Scattering of Surface Plasmon Polaritons by Metallic Nanostructures

Lina Cao

Submitted in partial fulfillment of the
requirements for the degree
of Doctor of Philosophy
in the Graduate School of Arts and Sciences

COLUMBIA UNIVERSITY

2009

ABSTRACT

Scattering of Surface Plasmon Polaritons by
Metallic Nanostructures

Lina Cao

Surface Plasmons (SPs) which are coherent oscillations of conduction electrons on a metal surface excited by electromagnetic radiation at a metal-dielectric interface have variety of applications in chemistry, optical devices, spectroscopy and bio/chemi sensors. Plasmon scattering is a growing area of importance for nonconventional meta-materials, condensed matter physics, and surface chemistry, thus it is very interested to study. A simulation tool for imaging scattering properties allows *ab-initial* design for plasmon devices as well as gives better physical insight for experiments. Furthermore, due to the high electric field density associated with SPs, Second-Harmonic Generation (SHG) is expected to be enhanced thus gives us extra physical insights.

In this thesis, a simulation tool is developed to calculate the scattering properties of Surface Plamon Polaritons (SHG) at both fundamental frequency (FF) and second-harmonic (SH). We present a comprehensive study of linear and nonlinear effects observed in the scattering process of surface plasmon polaritons (SPP) from localized surface deformations at a metal/dielectric interface. The electromagnetic field at the fundamental frequency (FF) is first determined by solving the corresponding set of reduced Rayleigh equations. The complete solution of these equations then allows us to investigate both the complex structure of the scattered electromagnetic field as well as the subtle mechanisms

by which incident SPPs are scattered into radiative modes (light) and outgoing SPP waves. Furthermore, the electromagnetic field at the FF is used to determine the nonlinear surface polarization at the second harmonic (SH) and subsequently both the electromagnetic field distribution as well as the amount of light generated at the SH. In this thesis, we will discuss our results including the size dependence of the scattering into both surface and radiated waves for several defect shapes as well as the computational issues and the physical phenomena of the scattering process.

This thesis is organized as follows. In chapter 1, I will give a brief introduction of SPs as well as their various applications. In chapter 2, the background theories as well as numerical techniques are discussed. Chapter 3 gives us a detailed description of surface SHG from scattering of SPPs by 1D Gaussian metallic nanostructures. Consequently, in chapter 4, the theory is extended to 2D circularly symmetric metallic nanostructures, which include Gaussian, Sphere-cap and Cylinder. Finally in Chapter 5, the some future direction of this thesis work is described.

TABLE OF CONTENTS

Acknowledgment

It gives me immense pleasure to be writing this thesis which shows the results of my research conducted over the past five years. I feel fortunate and privileged to have this wonderful experience to study at such a great institution. I would like to express my gratitude to all those who have helped me.

I am deeply indebted to my advisor Prof. Richard M. Osgood, Jr. for his guidance, suggestions and encouragement all the time of my research. I truly value his experience, and scientific knowledge. The serious attitude toward science, correct approaches to problem solving and good oral and written communication skills I have learned from him will be great assets for my whole life.

I would like to thank Dr. Nicolae Panoiu for his numerous suggestions and help. He helped me enormously in my scientific and academic growth. I truly value his broad knowledge in theoretical physics, scientific rigorousness, diligence and persistence. He always took the time out to discuss research ideas and provided invaluable suggestions. I have learned a lot from him both academically and personally.

I would like to thank all other faculty members in my thesis committee: Prof. Louis Brus, Prof. George Flynn, Prof. Chee-Wei Wong and Prof. Kenneth Eisenthal for their helpful discussion and suggestions. I particularly want to thank Prof. Flynn for his insightful suggestions on my research during each group meeting.

I also wish to thank my colleagues and friends, including Dr. Ravi Bhat, Dr. Jerry Dadap, Dr. Oliver Chen, Dr. Djordje Djukic, Dr. Iwei Hsieh, Dr. Ryan Roth, Ophir

Gaathon, Xiaoping Liu, Avishai Ophan, Jeffery Driscoll and all the members in Prof. Osgood group for their help and support.

My special and sincere gratitude goes to my parents, my sister and my brother. Their constant love, support and encouragement were of vital importance to my efforts. I would not go as far as PhD graduation without their love and understanding.

LIST OF FIGURES

Chapter 1

INTRODUCTION

This thesis is concerned with understanding the propagation of plasmon waves at the interface between a metal surface and a dielectric over-layer or vacuum. Such waves are of interest in many areas of physical chemistry and thus examining their interaction at surfaces is appropriate for advancing our understanding of elementary excitations for chemistry. In this chapter we will introduce the reader to the physical origins of the plasmonics followed by several sub-areas of interest for chemistry. We will also examine recent reports, which describe observations of plasmonic-wave scattering at surfaces; these reports have been enabled by impressive advances in nanoscale imaging tools. Finally we will briefly outline other related theoretical work in this area.

1.1. PHYSICAL ORIGIN OF PLASMONS

Surface Plasmons (SPs) are coherent oscillations of conduction electrons on a metal surface excited by electromagnetic radiation at a metal-dielectric interface. [1]. A plasmon is a coupling of an electro-magnetic wave with the oscillations of the valence electrons around the ion-cores in a conducting solid, typically metals or, in the infrared, doped semiconductors. The growing field of research of on such light-metal interactions is known as ‘plasmonics’. [2-3]. Two types of Surface Plasmon Resonances (SPRs) are widely used in surface-based chemical sensing, optical devices and photonic circuits. [4-18]. There are propagating surface plasmons which are known as surface plasmon polaritons (SPP) and non-propagating surface plasmons which are called localized surface plasmons (LSP). Detailed descriptions of these surface plasmons are listed here.

1.1.1 Surface plasmon polartions

Surface-plasmon polaritons (SPPs) are evanescent electromagnetic waves coupled to oscillations of the electron plasma in the metal that propagate along a metal-dielectric interface. A propagating surface plasmon wave is sketched schematically in Fig. 1.1. SPPs oscillate at optical frequencies. They are localized by a material interface with a positive dielectric constant (a dielectric) above, and a negative dielectric constant (metal) below.

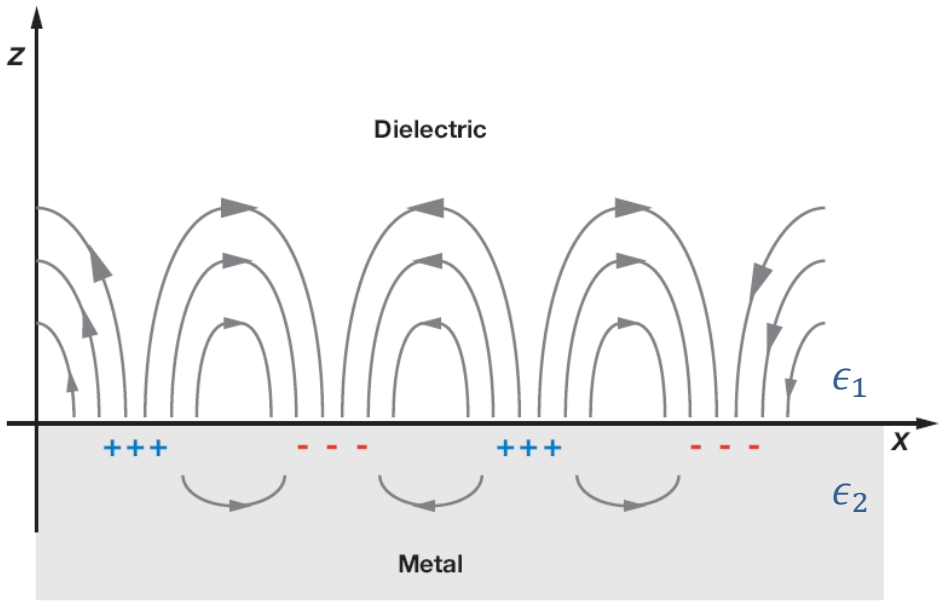

Figure 1.1 The charges and the electromagnetic field of SPs propagating on the surface in x direction are shown schematically. (ref. [4])

At wave-vectors much smaller than the metal Fermi wave-vector, these modes can be described by using Maxwell's equations. For these low wave-vectors, SPPs are essentially transverse in character with only a small longitudinal component; thus longitudinal component does increase in relative magnitude as the wave-increases. The transverse fields

polarize the dielectric along the driving field. In the metal, the polarization is opposite to the driving field due to the negative dielectric constant. This then creates equal and opposite electric displacements (*D*), in phase across the interface. These opposing electric displacements confine the current to this interface, generating the SPP collective electron oscillations.

Starting from Maxwell's Equations, we can derive the characteristics of this simple plasmonic system. The behavior in the z direction decays exponentially away from the interface. This derivation of the wave equation tells us that the exponential decay constant in a metallic medium is

$$k_i^2 = k_x^2 - \epsilon_i \left(\frac{\omega}{c}\right)^2 \tag{1.1}$$

The retarded dispersion relation for the plane surface of a semi-infinite metal with the dielectric function $\epsilon_1 = \epsilon_1^{'} + i\epsilon_1^{''}$, adjacent to a medium ϵ_2 as air or vacuum can be written as:

$$D_0 = \frac{k_{z1}}{\epsilon_1} - \frac{k_{z2}}{\epsilon_2} = 0 \tag{1.2}$$

Since the wave vector k_x is continuous across the interface [1], a simple algebra manipulation may then be used to solve for k_x, finally generating the dispersion relation for these simple surface plasmon modes. The dispersion relation from equation (1.2) can be written as:

$$k_x = \frac{\omega}{c}\sqrt{\frac{\epsilon_1 \epsilon_2}{\epsilon_1 + \epsilon_2}} \tag{1.3}$$

This wave-vector is no longer a simple linear function of permittivity as in standard dielectrics. Because we have the sum of dielectrics of opposite sign in the denominator, very large wave-vectors are possible. As we will show below the metallic dielectric constant, ϵ_1, has a substantial dependence on frequency. This dependence causes the SP wave-vectors to be very large at frequencies close to the resonant surface plasmon frequency. In particular, propagation of plasmon polaritons follows a dispersion relation, such as that seen for propagation of light in a periodic medium or as seen in the case of phonons in a crystal. The dispersion relation for surface plasmons, which is shown in Fig. 1.2, approaches the light line $\sqrt{\epsilon_2}\omega/C$ at small k_x, but remains larger than $\sqrt{\epsilon_2}\omega/C$.

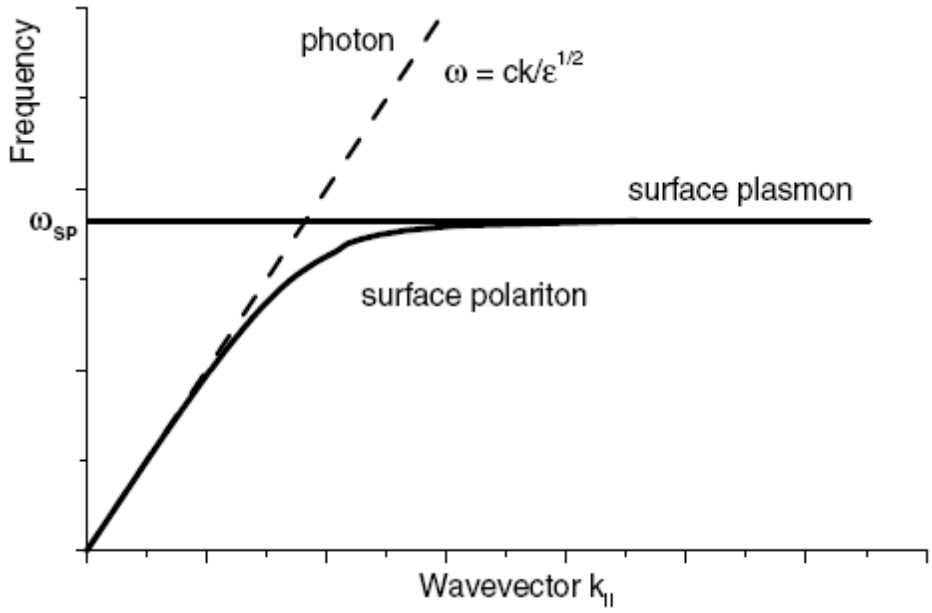

Figure 1.2 Dispersion of surface plasmon polaritons on a metal surface.

At larger k_x or when $\epsilon_1 \to \epsilon_2$, the value of ω_{sp} approaches

$$\omega_{sp} = \omega_p/\sqrt{1+\epsilon_2} \quad (1.4)$$

where ω_p is the plasma frequency. For a free electron gas, $\omega_p = \sqrt{\frac{4\pi n e^2}{m}}$, with n the bulk electron density. With the increasing ϵ_2, the value of ω_{sp} is reduced. At the interface of metal/air, $\epsilon_2 = 1$, thus, $\omega_{sp} = \omega_p/\sqrt{2}$.

Note that frequency is plotted in units of the plasma frequency (ω_p) and the wavevector in units of ω_p/c. In the figure we plot the 'so-called' light line as a dashed line; it gives the dispersion relation of an optical field propagating in the dielectric medium along the same direction as the surface plasmon.

The reason surface plasmon modes can achieve anomalously high wave-vectors at visible frequencies ("visible frequencies at X-ray wavelengths") is because they involve electrons rather than free-space optical fields. This simplified dispersion curve shows two important characteristics of surface plasmons. First the dispersion relation always lies at higher wave-vectors than the light line. Hence due to the difference in wave-vector, the plasmon field cannot efficiently couple to radiating modes. Conversely, free-space optical fields cannot directly stimulate surface plasmons unless momentum matching is somehow provided, using, say, a grating or prism. This behavior can be shown to be a consequence of the exponential decay normal to the surface, which requires an imaginary wave-vector in this direction. The absolute square of this positive quantity then adds to the light-line wave-vector to determine k^2, hence k must always be greater than that of the free space field.

A second feature of this dispersion relation is seen close to the frequency of 0.7 ω_p. At this point the wave-vector grows to be much larger than the light line. This large wave-

vector originates from the collective electron oscillations with sub-Angstrom wavelengths, which result in very large optical wave-vectors.

1.1.2 Localized Surface Plasmons

In addition to surface plasmons on a plane surface solid-state plasma oscillations can occur; in other geometries such as metallic particles or voids of different topologies, localized surface plasma excitations can be considered. Such surface plasma excitations in bounded geometries are called localized surface plasmons (LSPs). Fig. 1.3 illustrates the localized surface plasmon polaritons.

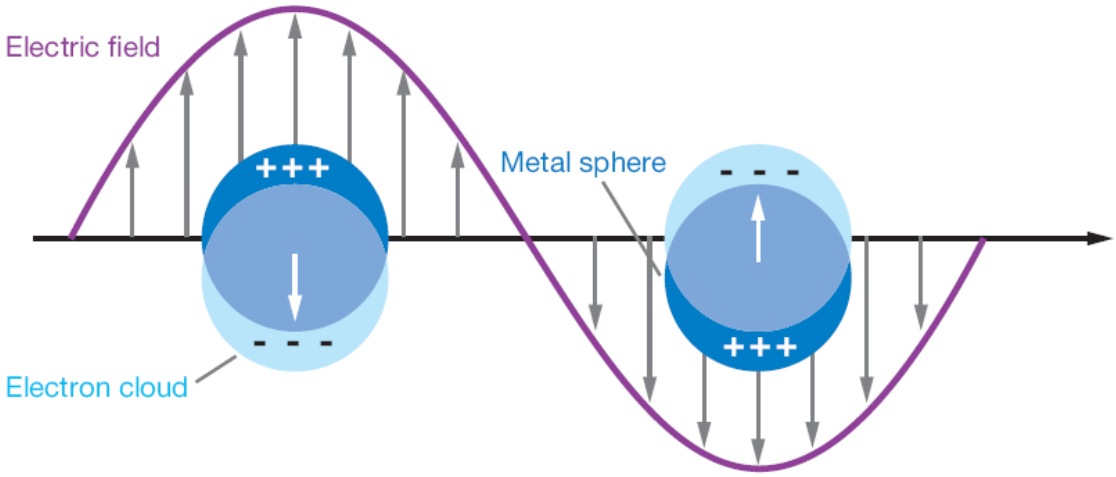

Figure 1.3 Schematic diagram illustration of localized surface plasmon polaritons. (ref. [4])

The LSP frequency can be determined in a non-retarded (electrostatic) approximation by solving the classical Dirichlet problem. This approximation is valid when the

characteristic length of the object is smaller than incident wavelength. The LSP has a different character from the SPP that is discussed above. As illustrated, the SPP has the dispersion relation $\boldsymbol{\omega_{sp} = \omega(k_{sp})}$ given by equation (1.3) and is a propagating surface mode. In contrast, LSPs are confined within discrete metal objects of limited spatial extend. They are characterized by discrete, complex frequencies which depend on the size and shape of the object, to which the surface plasmon is confined. LSPs can be resonantly excited with light of appropriate frequency (and polarization) irrespective of the excitation light wavevector. Therefore, LSPs also effectively decay with light emission. In contrast, the SPP mode can be excited only if both the frequency and wavevector of the excitation light match the SPP frequency and wavevector.

LSPs are confined to particles, and are due to the resonant build up of the electron oscillations within the metallic sphere, a significant electromagnetic field enhancement at small metallic particles is expected. This effect contributes to numerous phenomena such as light emission from STM tunnel junctions, enhanced scattering, surface enhanced Raman scattering (SERS) and second-harmonic generation (SHG).

1.1.3 Drude model

The plasmon properties are a result of the dispersion of the constituent materials. Thus it is essential to have a model for their relative permittivities. A common model which is used to treat the dispersion relations of a typical material system is the Drude model which is based on the assumption that metals have free valence electrons. In Drude model, it is assumed that the interactions between collisions are neglected as well as collisions are instantaneous. It can provide a simple approximation for a metal. If we

assume a lossless Drude metal, with plasma frequency, ω_p, by solving Newton's equations for the electron motion, we can obtain the example dispersion relation for plasmons shown in Fig 1.3. The dispersion relation follows this:

$$\epsilon = 1 - \frac{\omega_p^2}{\omega^2} \qquad 1.5$$

Where ϵ is the dielectric constant of the metal.

1.2 APPLICATIONS OF PLASMONS

One of the most important roles that plasmons have played is in the area of surface spectroscopy, surface reactions and surface structural probing. Several extremely important examples of these roles have been described in the literature and here we try only to give a brief summary of applications, which are applicable to chemical science.

1.2.1.Enhancing chemical reactions on surfaces

Chemical processes on bare, or uncapped, noble-metal nanoclusters have recently become a subject of renewed interest. This interest stems from several recent studies that have indicated the potential importance of nanoclusters as effective heterogeneous catalysts, e.g. for olefin oxidation, and the fact that size-dependent reactivity has been displayed in these experiments. This work has also given new impetus to the synthesis of high-quality low-dispersion nanosystems as well as the development of new nanoprobes to examine these systems. Other metallic nanocatalyst systems, include those prepared electrochemically, etc. The enhanced reactivity observed in some of these nanostructures,

particularly Au, has been the subject of significant discussion and interest and has been variously attributed to quantum-size dependence, surface structure, or defects and has led to related work on, for example roughened Au surface chemistry.

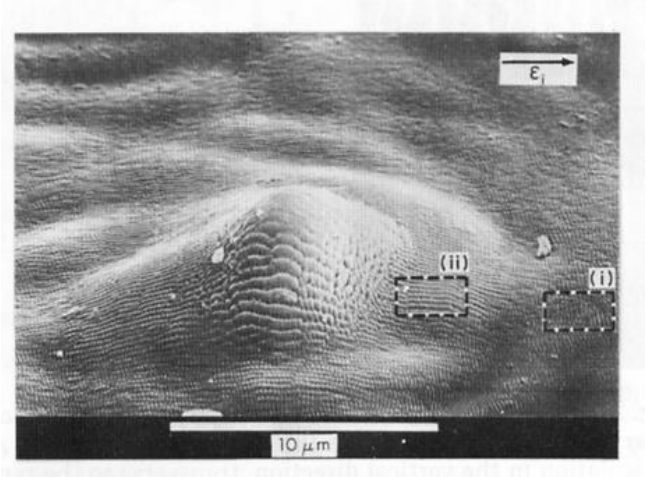

Fig. 1.4: Structure resonantly grown by plasmonically driven UV photochemistry of Cd from $(CH_3)Cd$ at 254nm. The spontaneous ordered growth is a result of a feedback mechanism with gain. ref. [5]

Similarly photochemistry on these same metallic nanoparticles is also an area of growing interest because enhanced-reaction chemistry can then also be derived from near-field enhancement of an incident optical beam due to local-plasmon excitation or if mounted on a dielectric substrate due to surface waves and their scattering. While work in this area has recently grown rapidly, the original work in this area was reported by Chen and Osgood using Cd nanoparticles of ~200A on carbon grids and relied on UV photoreactions in a low-pressure ambient of dimethyl cadmium. [5]. In this case, TEM

microscopy and polarization effects were used to show local field enhancement including growth controlled and "feedback" via local plasmon resonances determined by the particle geometry. This feedback effect was seen for both spontaneous particle growth on SiO_2 surfaces (see Fig. 1.4) and for intentional growth of diffraction gratings. More recently the Brus Group has reported plasmon-assisted growth by for local plasmon-enhanced CVD and electrochemistry on nano-particles. [6]. Finally, there has been a resurgence of interest in the chemical dynamics occurring at the surfaces of metal nanoparticles or clusters. One of these by the Wolf Group in Germany showed clearly that it was possible to couple into a plasmon resonance of a particle using pulsed excitation and excitation yielded desorbed molecules (water). [7].

In addition, photodynamics experiments on nanoscale silver spheres have also been recently reported for both desorbed molecular species and metal photoelectrons. With regard to the desorption of molecular fragments, Wolf and coworkers [7] have reported a femtosecond study of water desorption form nanoclusters of silver on an oxide support. In this case, excitation was close to the plasmon frequency of the silver particle, that is, at visible wavelengths. Desorption was attributed to coupling to phonons (or simple laser heating) due to plasmon relaxation.

1.2.2 Plasmons for control of surface energy flow

There have been many proposals for using plasmonic structures to enable a new generation of ultrasmall integrated optical devices as well structures to improve solar-energy collection or light-emitting diode performance. Most of these applications are far away from chemical physics and thus will not be described here. However, concepts embodied in plasmonic photonic devices structures carry the essence of ideas, which can

have a more chemical or photochemical nature to them. In particular, it is possible to use plasmonic structures to control the flow of surface energy in an interfacial region. As one example, of this we show the application of an array of metal spheres to form a type of plasmonic lens to reflect and redirect plasmonic energy in Fig. 1.5. [8]. The paper showed that incident SPP is focused by the SPP condensing lens. When the focused SPP was incident into the nanodot coupler, its transmission length through the nanodot coupler was confirmed to be three times longer than that of a metallic core waveguide owing to the efficient near-field coupling between the localized surface plasmon of neighboring nanoparticles. Furthermore, the transmission length through a waveguide zigzag-shaped nanodot coupler was as long as that through a linear one; again showing the low loss of plasmonic strengths over short distances.

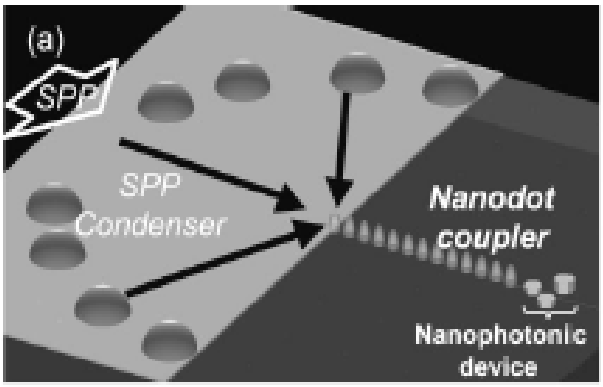

Fig. 1.5. Sketch of Nanodot coupler and SPP condenser. Ref. [8]

1.2.3 Surface Plasmons for surface probing

Probing the chemical and structiural state of surfaces is of continuing interest for catalysis; such probing can be done either using optical excitation of SPs or via direct

launching of SP's using an electron source. Prior to recent experiments, there had been no or very limited observations of the propagation of plasmons on surfaces. Most experimental observations of surface plasmons were based on the observations of energy loss spectroscopy, which showed an energy loss peak at integral values of ω_{sp}, or via optical resonances in the optical spectroscopy of light transmission through thin films.

Of course it is and was possible to carry out static imaging of surfaces using photographic film or via local photochemistry. These showed clearly the periodic nature expected for scattering of plasmonic waves. However, time-dependent phenomena were not observed. More recently advanced ultrafast laser excitation in conjunction with photoemission electron spectroscopy has been used to probe and image plasmons in real time. For example, Atsushi Kubo and his co-workers have demonstrated the imaging and quantum control of SP dynamics in a nanostructured silver film.

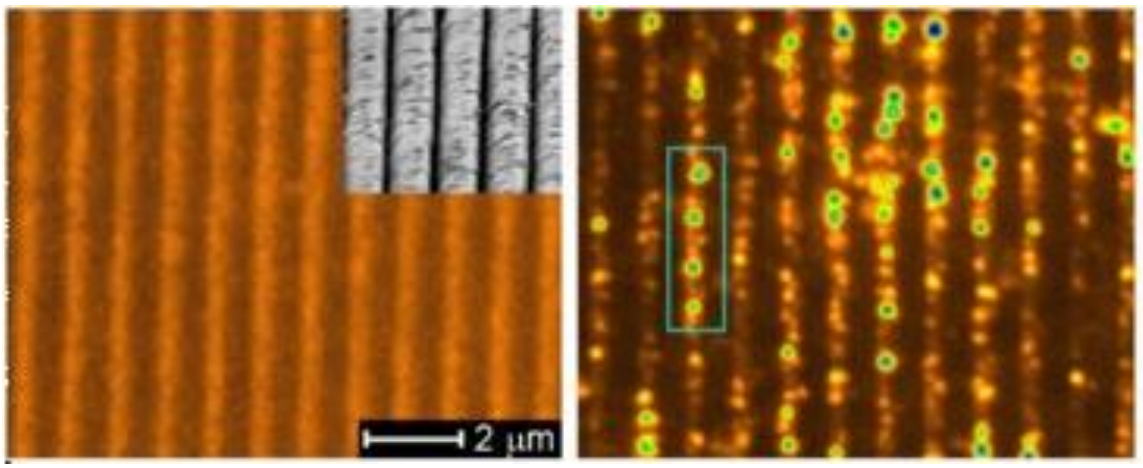

Fig 1.6. PEEM micrographs of the identical region on the silver grating obtained with (a) 254-nm line of a Hg lamp (1PP-PEEM), (b) p-polarized 400-nm femtosecond laser excitation (2PP-PEEM). Ref. [9].

By inducing and imaging the nonlinear two-photon photoemission from the sample with a pair of identical 10-fs laser pulses while scanning the pulse delay, they recorded a movie of SP fields at a rate of 330-attoseconds/frame. This development advances the time-resolution of electron microscopy for imaging the fundamental excitations in solids by more than twelve orders of magnitude. The dynamical imaging of surface plasmons in the suboptical cycle regime adds a new dimension to the study of plasmonic nanostructures. Surface probing can be enhanced by the nonlinear wavelength contrast of second harmonic generation. Thus in this case we hope to see scattering via conversion of the incident plasmon wave into second harmonic radiation. In particular, second-harmonic generation is a nonlinear optical process, in which photons interacting with a nonlinear material are effectively "combined" to form new photons with twice the energy, and therefore twice the frequency and half the wavelength of the initial photons. Within the electric dipole approximation, even-order harmonic generation is forbidden in the bulk of a centrosymmetric medium. The inversion symmetry, however, is broken at the surface of the medium, thus making even-order processes allowed in this region. Even-order nonlinear processes, such as second-harmonic generation (SHG), consequently exhibit a high degree of surface sensitivity for centrosymmetric media. [8,9]. As a result, second-harmonic (SH) fields, whether enhanced by plasmonic effects or not, have become an important surface diagnostic in surface science or colloidal chemistry. Surface SHG has been used to study a diverse set of surface phenomena and applications, e.g., the symmetry properties of surfaces, the nature of adsorbates at surfaces or interfaces, or noninvasive

probing of buried interfaces. [10]. Due to the highly enhanced field caused by surface plasmons, SHG is expected to be highly enhanced thus are very interested to study.

1.3 OVERVIEW

Using the above material as background, in this thesis we will be concerned with the scattering of plasmons from surface defects. Thus in this case, we assume that a plasmon wave is somehow excited and we examine how this wave scatters off of the defects. Further and most important we focus on the fact that such a plasmon wave may drive a nonlinear response in its medium. Our approach to solving this problem will be to use scattering theory to derive near analytic expressions; more details will provided in the next chapter on theoretical methods.

The general approach to solving the linear scattering problem has been previously examined by Maradudin and his collaborators in a series of seminal papers. In brief these results have shown provided the general outline of the theoretical method and provided initial theoretical insight. These authors have shown for example that scattering at the fundamental results in two general phenomena: scattering in plane of the SPP and scattering out of plane to yield radiated light. The former process is strongly resonant, the latter is less resonant but yield a highly directional surface to vacuum light beam – a nanoflashlight! These approaches used by these authors' have guided our work in this thesis.

Bibliography

[1] H. Raether, "Surface Plasmons on Smooth and Rough Surfaces and on Gratings" volume 111, Springer-Verlag, (1988)

[2] H.A. Atwater, "The promise of plasmonics", Sci. Am. 296, 56, (2007)

[3] E. Ozbay, "Plasmonics: Merging Photonics and Electronics at Nanoscale Dimensions", Science 311, 189 (2006)

[4] Willets, K.A.; Van Duyne, R. P. Ann. Rev.Phys. Chem. 58, 267, (2007)

[5] C.J. Chen and R.M. Osgood, Jr., "Direct Observation of the Local-Field-Enhanced Surface Photochemical Reactions." Phys. Rev. Lett. 50, 1705 (1983)

[6] L. Brus, "Noble Metal Nanocrystals: Plasmon Electron Transfer Photochemistry and Single-Molecule Raman Spectroscopy " Acc. Chem. Res. 41(12),1742 (2008)

[7] W. Nomura and M. Ohtsu, App. Phys. Lett. 86, 181108 (2005)

[8] J. Dadap, J. Shan, T. Heinz, "Theory of optical second-harmonic generation from a sphere of centrosymmetric material: small-particle limit", J. Opt. Soc. Ame. B. 21, 7, 1328-1347 (2004)

[9] A. Kubo, K. Onda, H. Petek, Z. Sun, Y. S. Jung, H. K. Kim, "Femtosecond Imaging of Surface Plasmon Dynamics in a Nanostructured Silver Film", Nano Lett. 5, 1123 (2005)

[10] D. Krause, "Optical surface second harmonic measurements of isotropic thin-film metals: Gold, silver, copper, aluminum, and tantalum", J. App. Phys. 96, 3626, 1786341 (2004)

[11] C.J. Chen and R.M. Osgood, Jr., "Surface-Catalyzed Photochemical Reactions of Physisorbed Molecules." Appl. Phys. 31, 171 (1983)

[12] C.J. Chen, H.H. Gilgen and R.M. Osgood, Jr., "Resonant, Optical Growth of Submicrometer Metal Gratings." Opt. Lett. 10, 173 (1985)

[13] R.M. Osgood, Jr. and D.J. Ehrlich, "Optical Induced Microstructure in Laser-Photodeposited Film." Opt. Lett. 7 , 385 (1982)

[14] N. -C. Panoiu, and R.M. Osgood, Jr., "Influence of the Dispersive Properties of Metals on the Transmission Characteristics of Left-handed Materials." Phys. Rev. E 68, 016611 (2003) (also featured in the Virtual Journal of Nanoscale Science and Technology 8 (5), August 4, 2003)

[15] N. -C. Panoiu, R.M. Osgood, Jr., "Subwavelength Nonlinear Plasmonic Nanowire." Nano Lett. 4, 2427 (2004) (also featured in the Virtual Journal of Nanoscale Science and Technology 10 (7), August 16, 2004 and Virtual Journal of Ultrafast Science 3 (9), September, 2004)

[16] S. Zhang, W. Fan, K.J. Malloy, S.R.J. Brueck, N. -C. Panoiu, and R.M. Osgood, Jr., "Experimental Demonstration of Near-Infrared Negative-Index Metamaterials," Phys. Rev. Lett. 95, 137404 (2005)

[17] R.M. Roth, N. -C. Panoiu, M.M. Adams, R.M. Osgood, Jr. C.C. Neacsu, and M.B. Raschke, "Resonant-Plasmon Field Enhancement from Asymmetrically Illuminated Conical Metallic-Probe Tips." Opt. Exp 14, 2921 (2006) (also featured in the Virtual Journal for Biomedical Optics 1 (5), May 5, 2006 and in the Virtual Journal for Biomedical Research 11 (10), May 15, 2006)

[18] W. Fan, S. Zhang, N.-C. Panoiu, A. Abdenour, S. Krishna, R.M. Osgood, Jr., K.J. Malloy, and S.R.J. Brueck, "Second Harmonic Generation from a Nanopatterned Isotropic Nonlinear Material." Nano Lett. 6, 1027 (2006)

[19] R.M. Roth, N.-C. Panoiu, J.I. Dadap, M. M. Adams, R.M. Osgood, Jr., J. Warren, and A. Stein, "Polarization-Tunable, Plasmon-Enhanced Extraordinary Transmission Through Metallic Films Using Asymmetric Cruciform Apertures" Opt. Lett. 32, 3414 (2007), Virtual J. Nanoscale Research & Technology (1/14/2008)

[20] L. Huang, S. Chey and J. Weaver, *Phys. Rev. Lett.* 78, 368 (2001); V. N. Antonov J. S. Palmer, P.S Waggoner, A.S. Bhatti, and J.H. Weaver, Phys. Rev. B, 70, 045406 (2004)

[21] X. M. Yan, J. N., M. Robbins, H. Park, W. Zhao and J. M. White, *J. Nanopret. Res.* 4, 525 (2002).

[22] M. Valden, X. Lai and D. Goodman, *Science* 281, 1617 (1998); M. Haruta and M. Date, *Appl. Catal.* 222, 427 (2001).

Chapter 2

BACKGROUND THEORY AND RELEVANT NUMERICAL TECHNIQUES

In this chapter we discuss the background theory for the research work in this thesis. Our discussion will include the main theoretical scattering equations following the theory description of Rayleigh scattering process by the used of impedance boundary conditions, as well as a short overview of the computational issues involved. Basic formulae of Second Harmonic Generation from the scattering of SPs are also included. In addition, to provide perspective, we will also describe a widely used numerical method, Finite Difference Time Domain (FDTD), which can be used to tackle the problems such as those discussed here.

This chapter is organized as follows. In Section 2.1, we will discuss the main theoretical equations we used as well as the background theories. In Section 2.2, the numerical approaches will be discussed as well as the challenges and our problem-solving methods. In Section 3, we will discuss Finite Difference Time Domain method, which is also widely used to simulate nano-plasmonics.

2.1 SCATTERING THEORY FOR SURFACE INTERACTIONS

Scattering of Surface Plasmon Polaritons is an interesting topic which has variety of applications as discussed in chapter 1. Thus, construction of a simulation tool to understand the scattering process is essential to give physical insight to experiments and to design *ab initio* experiments. In this thesis, we seek to establish a model which enables us to calculate the scattering process of SPP by metallic nanostructures at both fundamental frequency and Second Harmonic.

The sketch of our methodology is illustrated in Figure 2.1. To calculate the Second Harmonic Generation (SHG) from scattering of Surface Plasmon Polaritons (SPPs), two basic steps which correspond to scattering at fundamental frequency and second harmonic respectively are needed. For the linear scattering process, or the first step, we used the reduced Rayleigh-equation method, in which the electric field after the scattering is characterized by the sum over the incident electric field and the scattered electric field at different directions which are determined by wave-vectors. An impedance boundary condition is then incorporated to set up an equation, which is used for solving the scattering amplitude associated with different wave-vectors. All information about the scattered waves is well-defined by their corresponding wave-vectors, corresponding to different electronic modes (photons or SPP) at different out-going directions. The scattering amplitudes are then solved numerically in this thesis. By substituting scattering amplitudes back into the initial electric field distribution equation, we can get the electric-field distribution after scattering all over the space, which definitely include the electric field at the metal surface.

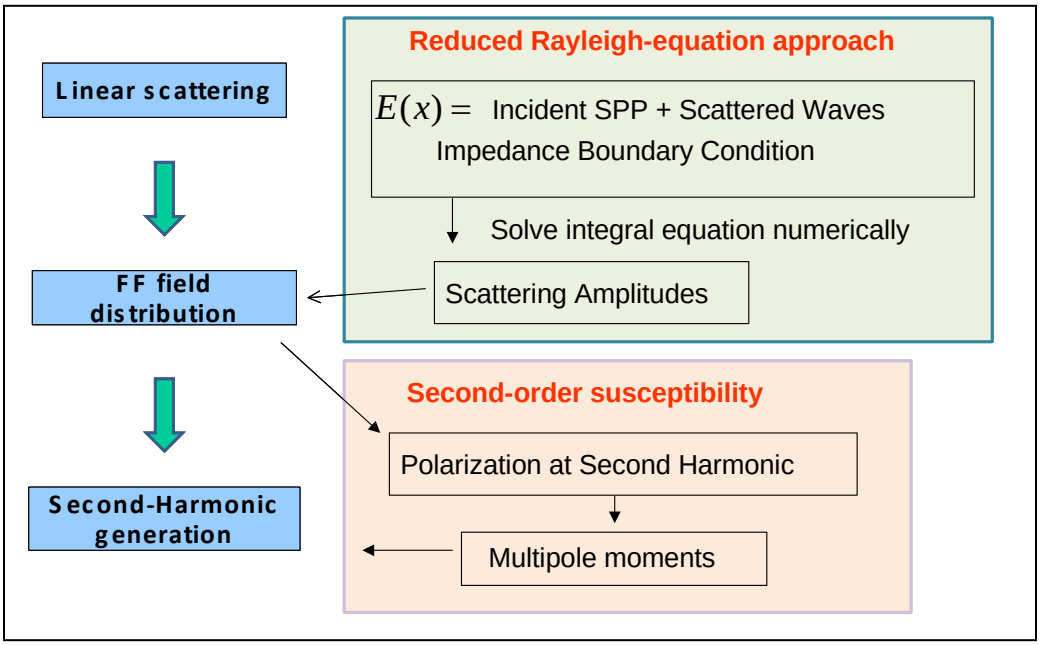

Fig. 2.1 Illustration of scattering theory for surface plasmon polaritons. The left side shows two basic steps while the right side gives the method at each step respectively.

For the second step, which is calculation for second-harmonic generation (SHG), as shown in figure 2.1, the electric field at FF at the surface is required. In this case, the second-order susceptibility is inserted into the electric-field distribution of FF to get polarization at the second-harmonic frequency for different spatial points, followed by an expansion method to obtain different orders of multipole moments. A multipole-moment expansion method can only be used when the object is very small ($ka \ll 1$). In this thesis, the object is chosen to be small compared to the incident wavelength so that by keeping the multi-moments up to second order, which include electric-dipole moment, magnetic-dipole moment and electric-quadrupole moment, we can get accurate results. These three

moments lead to the radiation at the second-harmonic frequency. Detailed explain of this methodology is described in the following section.

2.1.1 Linear SPP scattering

One can solve linear SPP scattering starting from Maxwell's equations, which is in fact the methodology used by the more completely FDTD algorithm (see below). In this thesis, an impedance boundary condition incorporated with Rayleigh scattering approach is next used. The use of impedance boundary condition [2] in theoretical studies of optical interactions at rough metal/vacuum interfaces simplifies such studies by eliminating the need for determining the electromagnetic field in the metal [1]. Consequently, only the electromagnetic field in the vacuum region is dealt with explicitly. For a metal/vacuum interface defined by the function $x_3 = \xi(x_1, x_2)$ in the case of two-dimensional or $x_3 = \xi(x_1)$ in the case of one-dimensional surface, while the region $x_3 > \xi(x_1, x_2)$ is vacuum and $x_3 < \xi(x_1, x_2)$ is metal, the usual Maxwell boundary conditions satisfied by the tangential components of the magnetic and electric fields at the surface can be replaced by local impedance boundary conditions on the planar surface $x_3 = \xi(x_1, x_2)$ of the form for one-dimensional case:

$$\left(-\xi'(x_1)\frac{\partial}{\partial x_1} + \frac{\partial}{\partial x_3}\right) H_2^{\uparrow}(x_1, x_3|\omega)|_{(x_3=\xi(\omega))} = \frac{1}{\epsilon(\omega)} K(x_1|\omega) H_2^{\uparrow}(x_1, x_3|\omega)|_{(x_3=\xi(\omega))} \quad 2.1$$

where the time dependence of the form $e^{-i\omega t}$ has been suppressed. Thus, this form of the impedance boundary condition is satisfied on the rough surface $x_3 = \xi(x_1, x_2)$, In the case of a deterministic surface profile function $\xi(x_1, x_2)$, the impedance function $K(x_1|w)$ can

be expanded in powers of the ratio of the optical skin depth of the metal at the frequency ω. $d(\omega) = \left(\frac{c}{\omega}\right)(-\varepsilon)^{-1/2}$, to the radius of curvature of the surface at each point. If $x_3 = \xi(x_1, x_2)$ is a periodic function of x_1, as in the case of a classical grating, a matrix equation for the Fourier coefficients of K, that is valid to all orders in $d(\omega)$, is obtained.

An alternative approach to the use of an impedance boundary condition is to satisfy it at the planar metal/vacuum interface $x_3 = 0$, and the effects of the corrugations of the real surface are taken into account through the coordinate dependence of the surface impedance. Following this approach, the impedance boundary condition is written as

$$H_2^{\uparrow}(x_1, x_3|\omega)|_{(x_3=\xi(\omega))} = \exp(ik(\omega)x_1)\, P(x_1|\omega) H_2^{\uparrow}(x_1, x_3|\omega)|_{(x_3=0)} \qquad 2.2$$

for the p and s-polarized fields, respectively for one dimensional case. Here, H and E are the single, nonzero components of the total magnetic and electric fields in the vacuum region above the metal surface, respectively. The attractiveness of this boundary condition is due to the fact that the Rayleigh expression for the nonzero component of the magnetic field in the vacuum region $x_3 > 0$, H_2, is exact.

The derivation of the boundary condition (2.2) for p-polarization starts by introducing a generalized, nonlocal, form of it [1]

$$\frac{\partial}{\partial x_3} H_2^{\uparrow}(x_1, x_3|\omega)|_{(x_3=0)} = \int_{-\infty}^{\infty} dx_1'\, P(x_1|x_1') H_2^{\uparrow}(x_1, x_3|\omega)|_{(x_3=0)} \qquad 2.3$$

The magnetic field component H_2 is the sum of an incident wave and scattered waves

$$H_2^{\uparrow}(x_1, x_3|\omega)|_{(x_3=0)}$$

$$= e^{ikx_1 - i\alpha_0(k,\omega)x_3} + \int_{-\infty}^{\infty} \frac{dq}{2\pi} R_p(q|k)\, e^{iqx_1 - i\alpha_0(q,\omega)x_3} \tag{2.4}$$

where $\alpha_0(q,\omega) = ((\omega^2/c^2) - q^2)^{1/2}$. By substituting equation 2.4 to equation 2.3, we obtain the integral equation satisfied by the scattering amplitude $R_q(q,k)$

$$i\alpha_0(q,\omega)R_p(q|k) - \int_{-\infty}^{\infty} \frac{dq}{2\pi} \hat{P}(q|p)R_p(q|k) = i\alpha_0(q,\omega)2\pi\delta(q-k) + \hat{P}(q|k) \tag{2.5}$$

while $\hat{P}$ is the Fourier transform of the function P through:

$$P(x_1|x_1') = \int_{-\infty}^{\infty} \frac{dq}{2\pi} \int_{-\infty}^{\infty} \frac{dk}{2\pi} e^{iqx_1} \hat{P}(q|k) e^{-ikx_1''} \tag{2.6}$$

By expressing $\hat{P}$ as the sum of a contribution P_0 associated with an ideal metal/vacuum interface at $x_3 = 0$, and a part which describes the effects of the surface roughness, we introduce the Green's function

$$G_p(k,\omega) = \frac{i\epsilon(\omega)}{\epsilon(\omega)\alpha_0(k,\omega) + \alpha(k,\omega)} \tag{2.7}$$

The final expression for $P(x_1|\omega)$ can be achieved and expressed as:

$$P(x_1|\omega) = -\frac{\omega}{c} \frac{1}{\left(-\epsilon(\omega)\right)^{1/2}} \left[1 + \frac{1-\epsilon(\omega)}{\epsilon(\omega)} \frac{1}{d(\omega)} \times (1 - d^2(\omega)D^2)^{\frac{1}{2}} \xi(x_1) + O(\xi^2)\right] \tag{2.8}$$

where $D \equiv d/dx_1$, and $d(\omega)$ is the optical skin depth of the metal at frequency ω.

Similarly, s-polarization component can be solved and is has the expression

$$S(x_1|\omega) = \frac{\omega}{c}\left(-\epsilon(\omega)\right)^{1/2}\left[1 - \frac{1-\epsilon(\omega)}{\epsilon(\omega)}\frac{\xi(x_1)}{d(\omega)} + O(\xi^2)\right] \quad 2.9$$

2.1.2 Second Harmonic Generation

Nonlinear optical studies can provide substantial information about ambient surfaces and interfaces. They can determine symmetry properties of the surface, characterize the nature of adsorbates or defects in the surface layers, and probe monolayers of molecules that have been applied to the surface. Surface second-harmonic generation (SHG) is particularly useful for systems with inversion symmetry, as much of the signal comes from dipolar response of atoms near surfaces and interfaces. The early theoretical model of surface SHG focused on solving Maxwell's equations for a reradiated second-harmonic field that arises from a nonlinear polarization induced by the incident field. In this way, the polarization is given by $P_i^{(2)} = \chi_{ijk}^{(2)} E_j^{(\omega)} E_k^{(\omega)}$, where $\chi^{(2)}$ is the material-dependent nonlinear susceptibility tensor and $E^{(\omega)}$ is the incident linear field with the frequency ω.

A simple classical model serves to illustrate the expected magnitude of the second-order response. In the presence of an applied harmonic field $E^{(\omega)}$, an atom in the material develops an induced dipole moment $p^{(\omega)} = \alpha(\omega)E^{(\omega)}$, while $\alpha(\omega)$ is the atomic polarizability. For atoms near surfaces or interfaces, $E^{(\omega)}$ is also expected to have

significant spatial variation. Therefore, the induced atomic dipoles feel a gradient force at twice the frequency.

$$F^{(2\omega)} = \left(p^{(\omega)}.\nabla\right)\mathrm{E}^{(\omega)} = \alpha(\omega)\left(E^{(\omega)}.\nabla\right)E^{(\omega)} \tag{2.10}$$

Assuming the force is primarily effective at accelerating a single electron charge per atom, we can find an induced dipole moment per unit volume,

$$\begin{aligned} P^{(2\omega)} &\approx \frac{ne}{4m\omega^2}\alpha(\omega)\left(E^{(\omega)}.\nabla\right)E^{(\omega)} \\ &= \frac{e}{16\pi m\omega^2}4\pi\alpha(\omega)n\left(E^{(\omega)}.\nabla\right)E^{(\omega)} \end{aligned} \tag{2.11}$$

where n is the atomic density. In terms of the dielectric function $\epsilon(m)$ this can be written as:

$$P^{(2\omega)} \approx \frac{e}{16\pi m\omega^2}(\epsilon_m - 1)\left(E^{(\omega)}.\nabla\right)E^{(\omega)} \tag{2.12}$$

By integrating across the surface layer, one can get

$$P_s^{(2\omega)} \approx \frac{e}{16\pi m\omega^2}(\epsilon_m - 1)E_z^{(\omega)}E^{(\omega)} \tag{2.13}$$

Thus the expected second order susceptibility tensor has the expression:

$$\chi^{(2)} \approx \frac{e}{16\pi m\omega^2}(\epsilon_m - 1) \tag{2.14}$$

When the surface is isotropic, symmetry arguments show that the surface second-order nonlinear susceptibility tensor $\chi^{(2)}$ has three families (z direction is normal to the surface):

$$\begin{gathered} \chi_{xxz}^{(2)} = \chi_{xzz}^{(2)} = \chi_{yyz}^{(2)} = \chi_{yzz}^{(2)} \\ \chi_{zzz}^{(2)} \\ \chi_{zxx}^{(2)} = \chi_{zyy}^{(2)} \end{gathered} \tag{2.15}$$

2.1.3 Multipole expansion method:

The multipole expansion method is widely used to calculate radiation. It starts with the electric vector potential and then a Taylor expansion to get different term. For electric vector potential $A(r)$, In MKS unit system, the relation between A and current density J is expressed as:

$$A(r) = \frac{1}{c}\int J(x')\frac{e^{ik|x-x'|}}{|x-x'|}d^3x' \tag{2.16}$$

Inserting the equation $|x-x'| = r - n\cdot x'$, we can rewrite equation (2.16) to be:

$$A(r) = \frac{1}{c}\sum_n \frac{(-ik)^n}{n!}\int J(x')\cdot(\mathbf{n}\cdot x')^n \cdot d^3x' \tag{2.17}$$

In order to use this method for 2D system, we need to use cylindrical coordinates. Thus, equation (2.16) is written as:

$$A(r) = \frac{\mu_0}{4\pi}\int d^2r_\perp' \cdot J(r_\perp')\int_{-\infty}^{\infty}\frac{e^{ik\sqrt{(r_\perp - r_\perp)^2+(z-z')^2}}}{\sqrt{(r_\perp - r_\perp)^2+(z-z')^2}}dz' \tag{2.18}$$

Notice that equation (2.18) is in SI units. Let's assume $z - z' = \zeta$; equation (2.18) can be rewritten as

$$A(r_\perp) = \frac{\mu_0}{4\pi}\int d^2r_\perp' \cdot J(r_\perp')\,2\int_0^{\infty}\frac{e^{ik\sqrt{(r_\perp - r_\perp)^2+\zeta^2}}}{\sqrt{(r_\perp - r_\perp)^2+\zeta^2}}dz' \tag{2.19}$$

As we know,

$$\int_0^\infty g(z)e^{ikf(z)}dz = \sqrt{-\frac{\pi}{2f''(z_0)}}\,g(z_0)e^{-\frac{i\pi}{4}}\frac{e^{ikf(z_0)}}{\sqrt{k}} \tag{2.20}$$

In order to use equation (2.20), we assume $f(\zeta) = \frac{1}{g(\zeta)} = \sqrt{\left(r_\perp - r_\perp^{'}\right)^2 + \zeta^2}$, thus,

We can get

$$A(r_\perp) = \frac{\mu_0}{4\pi}\sqrt{2\pi i}\int d^2 r_\perp^{'} \cdot J(r_\perp^{'}) \cdot \frac{e^{ik|r_\perp - r_\perp^{'}|}}{\sqrt{k\left|r_\perp - r_\perp^{'}\right|}} \tag{2.21}$$

Equation (2.21) has the similar form as equation (2.16), thus a similar approach which is assuming $\left|r_\perp - r_\perp^{'}\right| \cong \rho - n \cdot r_\perp^{'}$. Substituting this equation back to the expression of vector potential, we can get

$$A(r_\perp) = \frac{\mu_0}{4\pi}\sqrt{2\pi i}\frac{e^{ik\rho}}{\sqrt{k\rho}}\sum_n \frac{(-ik)^n}{n!}\int J\left(r_\perp^{'}\right)\cdot\left(n \cdot r_\perp^{'}\right)^n \cdot d^2 r_\perp^{'} \tag{2.22}$$

From electromagnetic theory, as we know, magnetic induction

$$B = \nabla \times A \tag{2.23}$$

For radiation system,

$$E = B \times n \tag{2.24}$$

After the electric field E and magnetic field B are known from the expression, the radiation power is given by this equation:

$$\frac{dP}{d\theta} = \frac{1}{2}Re[\rho \cdot n \cdot (E \times H^*)] \tag{2.25}$$

$$\frac{dP}{d\Omega} = \frac{1}{2} Re[\rho \cdot n \cdot (E \times H^*)]$$

for 2D and 3D system respectively. In equation (2.25), θ is the angle defined by cylindrical coordinates while $d\Omega = d\theta d\phi$ which is defined by spherical coordinates.

Equation (2.25) is used to calculate the angular distribution of the radiated power while the total radiated power can be gotten by a simple integration.

Equations (2.17) and (2.22) clearly show the vector electric potential's dependence on the order of $(k \cdot r)$. Where $k \cdot r \ll 1$, we have to keep only the first several orders to get accurate result. The first term ($n = 1$) is related to an electric dipole term while the second term ($n = 2$) ends up as two terms which are magnetic dipole and electric quadrupole term. In this thesis, we kept the expansion order to be 2, which means the electric dipole, magnetic dipole, electric quadrupole moments are kept.

2.2. NUMERICAL APPROACH

After having derived all equations to solve the problem, another major challenge is our choice of numerical approach. In this dissertation, the numerical approaches, which are used in both linear and nonlinear frequencies as well as for both 1D and 2D codes, are described as follows.

Recall the theoretical approaches which is illustrated in Fig. 2.1 we described above, there are two main steps. For numerical simulations, three main source codes were used; FF scattering-amplitude solving (step 1), electric field distribution at FF (step 2) and SHG

(step 3) respectively. Each of these three codes is about 1000 lines long and all of them are written in C++.

2.2.1 Step 1: solving integral equations for scattering amplitudes

After all the analytical derivations, solving the scattering amplitudes becomes solving an integral equation which has the form of for 1D:

$$R(q) = T(q) + \int_{-\infty}^{\infty} dpV(p,q)R(p) \tag{2.26}$$

while both function $T(q)$ and function $V(p,q)$ are well defined as an associated analytical formulation. The function R is what we need to solve. Furthermore, in equation (2.26), function $V(p,q)$ has singular points at $q = \pm k$. In order to solve this equation, we factored the term $\frac{1}{q-k} - \frac{1}{q+k}$ out, which means equation (2.26) becomes

$$R(q) = T(q) + \int_{-\infty}^{\infty} dpM(p,q)\left(\frac{1}{q-k} - \frac{1}{q+k}\right)R(p) \tag{2.27}$$

We add a delta function on the left hand side of equation (2.27), since $\int_{-\infty}^{\infty} dpR(p)\delta(p - q) = R(q)$, the equation we need to solve becomes

$$-T(q) = \int_{-\infty}^{\infty} dp\left(M(p,q)\left(\frac{1}{q-k} - \frac{1}{q+k}\right) - \delta(p-q)\right)R(p) \tag{2.28}$$

To solve this equation numerically, the grid points are evenly distributed along p and we used the numerical method from the book Numerical Recipes in C++ for solving integral equations with singular kernels. [3].

The difference between 2D and 1D include that for 2D the integral equation which we need to solve becomes two coupled integral equations, which has the form

$$-T_1(q) = \int_{-\infty}^{\infty} dp(M_{11}(p,q)R_1(p) + M_{12}(p,q)R_2(p))$$
$$-T_2(q) = \int_{-\infty}^{\infty} dp(M_{21}(p,q)R_1(p) + M_{22}(p,q)R_2(p)) \quad 2.29$$

In order to solve both R_1 and R_2, we generate new vectors $T(q) = \begin{bmatrix} T_1(q) \\ T_2(q) \end{bmatrix}, R(p) = \begin{bmatrix} R_1(p) \\ R_2(p) \end{bmatrix}$, as well as a new matrix $M(p,q) = \begin{bmatrix} M_{11}(p,q) & M_{12}(p,q) \\ M_{21}(p,q) & M_{22}(p,q) \end{bmatrix}$. Equation (2.29) becomes

$$-T(q) = \int_{-\infty}^{\infty} dpM(p,q)R(p) \quad 2.30$$

This equation is solved by the same approach as we used for solving equation (2.26). Notice that because of this reorganization of functions, the matrix equation for numerically solution doubles the dimension, thus leads to a numerical cost of up to $2^3 = 8$ times.

2.2.2 Step 2: getting FF field distribution

Electric (and/or magnetic) field distribution at FF has the expression of sum over incident SPP field and an integral of scattered field over all the wave-vectors. From numerical code of step 1, scattering amplitudes are saved in files. Thus the main code for this step is an integration function. An adaptive numerical integration method [3] is used to ensure the convergence of code. Since scattering amplitudes are solved numerically, we

only have a discretized series of values (for our case, around 1500 to 2000 grid points). The scattering amplitudes' values where we don't have are reached by interpolation of the two neighbor grid points.

As we have mentioned, the integral equation has a singular point at $q = k$, for the integration, this point is considered separately by analytical approach, which is the principal value as illustrated in equation (2.31).

$$\int_{-\infty}^{\infty} dpE(p)R(p) = \int_{-\infty}^{k-\frac{\delta}{2}} dpE(p)R(p) + \int_{k+\frac{\delta}{2}}^{\infty} dpE(p)R(p) + \int_{k-\frac{\delta}{2}}^{k+\frac{\delta}{2}} dpE(p)R(p) \tag{2.31}$$

δ is chosen to be really small ($10^{-6}k$) to ensure the correct result, furthermore, we did try smaller δ to check the convergence. Even the singular point is taken out, we still expect a denser grid points needed when $p \to k$, thus, a decomposition of the first two terms is incorporated, which is

$$\int_{-\infty}^{k-\frac{\delta}{2}} dpE(p)R(p) = \int_{-\infty}^{k-\Delta} dpE(p)R(p) + \int_{k-\Delta}^{k-\frac{\delta}{2}} dpE(p)R(p) \tag{2.32}$$

Similar approach is used for the second term. Here Δ is chose to be around $10 - 100\delta$ for numerical calculation. By doing this, the simulation time goes down from 5 hours to around 1 hour.

2.2.3 Step 3: Second Harmonic Generation

Electric-field distribution for the defect region is saved from step 2. The C++ code for step 3 starts from obtaining the second-order polarization and then the integration for three multipole moments. A similar integration approach as step 2 is used. Furthermore, the radiation angular distribution and radiated power are calculated and plotted by Matlab codes.

2.3 FINITE DIFFERENCE TIME DOMAIN METHOD

The Finite-diference time-domain (FDTD) method is an *ab initio* solution method to obtain the full exact solution to Maxwell's equations [6]. It is based upon a spatial sampling of the unknown electric field $\sim E$ and magnetic field $\sim H$ within the computational domain and application of initial conditions on this space grid. The Maxwell's equations at a particular time step are then solved on the entire space grid, and finally the electric and magnetic fields are forward-stepped in time. The sampling in space is at sub-wavelength resolution and is set depending on the smallest spatial feature that needs to be resolved. The time-step for advancing the solution in time is selected to ensure numerical stability of the algorithm using the Courant stability criterion. Since FDTD is a generic, non-system-dependent numerical technique, it can be applied to a wide variety of problems without changing the underlying simulation engine. Moreover, since vector field boundary conditions are rigorously enforced at all material interfaces, as nonlinearity, gain /

absorbtion, and dispersion can be naturally incorporated into the algorithm. Furthermore, due to FDTD's *ab initio* nature, accurate field solutions can be obtained with an accuracy determined primarily by the grid resolution.

2.3.1 Maxwell's equations in a material medium

In vacuum, $E(r,t)$and $H(r,t)$ can collectively predict complete electromagnetic wave behavior. However, in a material medium two more vector fields, the electric displacement $D(r,t)$ and the magnetic flux density $B(r,t)$, need to be defined. For a source-free region, i.e. with no free electric charges or currents, Maxwell's equations relate the four fields $E(r,t), H(r,t), D(r,t)$ and $B(r,t)$ through the following relations:

$$\begin{aligned} \nabla \times H(r,t) &= \frac{\partial D(r,t)}{\partial t} \\ \nabla \times E(r,t) &= -\frac{\partial B(r,t)}{\partial t} \\ \nabla \cdot D(r,t) &= 0 \\ \nabla \cdot B(r,t) &= 0 \end{aligned} \qquad 2.33$$

Here the electric displacement field, $D(r,t)$, describing the electric properties of the medium is related to the electric field, $E(r,t)$, by this following equation:

$$D(r,t) = \epsilon_0 E(r,t) + P(r,t) \qquad 2.34$$

where $P(r,t)$ is the induced polarization density.

Similarly the magnetic flux density, $B(r,t)$, describing the magnetic properties of the medium is related to the magnetic field, $H(r,t)$, by

$$B(r,t) = \mu_0 H(r,t) + M(r,t) \tag{2.35}$$

where $M(r,t)$ is the magnetization density; if nonmagnetic medium is considered, $M(r,t) = 0$.

Moreover, the induced polarization density, $P(r,t)$, is related to the electric field, $E(r,t)$, through relations determined by the electric properties of the medium. This $E(r,t)$~$P(r,t)$ relation for most medium is non-trivial and depends on different kinds of medium's inherent properties, namely homogeneity, linearity, dispersiveness, and absorbtion characteristics. However, for describing the basic premises of the finite-difference time-domain method, we consider a homogeneous, nondispersive, and linear medium where $P(r,t) = \epsilon_0 \chi E(r,t)$. For such a medium, the electric displacement field is given by

$$D(r,t) = \epsilon E(r,t) \tag{2.36}$$

where $\epsilon = \epsilon_0(1+\chi)$ is the electric permittivity of the medium and χ is the electric susceptibility. The Maxwell's equations in such a media can then be written as:

$$\begin{aligned} \frac{\partial E(r,t)}{\partial t} &= \frac{1}{\epsilon}(\nabla \times H(r,t)) \\ \frac{\partial H(r,t)}{\partial t} &= -\frac{1}{\mu_0}(\nabla \times E(r,t)) \\ \nabla \cdot E(r,t) &= 0 \\ \nabla \cdot H(r,t) &= 0 \end{aligned} \tag{2.37}$$

2.3.2 Basic FDTD algorithm

Based on equation 2.37 for a homogeneous, linear, lossless and nondispersive material with no free sources, the components of $E(r,t)$ and $H(r,t)$ satisfy the following coupled scalar equations:

$$\begin{aligned}
\frac{\partial E_x(r,t)}{\partial t} &= \frac{1}{\epsilon}\left(\frac{\partial H_z(r,t)}{\partial y} - \frac{\partial H_y(r,t)}{\partial z}\right) \\
\frac{\partial E_y(r,t)}{\partial t} &= \frac{1}{\epsilon}\left(\frac{\partial H_x(r,t)}{\partial z} - \frac{\partial H_z(r,t)}{\partial x}\right) \\
\frac{\partial E_z(r,t)}{\partial t} &= \frac{1}{\epsilon}\left(\frac{\partial H_y(r,t)}{\partial x} - \frac{\partial H_x(r,t)}{\partial y}\right) \\
\frac{\partial H_x(r,t)}{\partial t} &= \frac{1}{\mu_0}\left(\frac{\partial E_y(r,t)}{\partial x} - \frac{\partial E_z(r,t)}{\partial y}\right) \\
\frac{\partial H_y(r,t)}{\partial t} &= \frac{1}{\mu_0}\left(\frac{\partial E_z(r,t)}{\partial x} - \frac{\partial E_x(r,t)}{\partial z}\right) \\
\frac{\partial H_z(r,t)}{\partial t} &= \frac{1}{\mu_0}\left(\frac{\partial E_x(r,t)}{\partial y} - \frac{\partial E_y(r,t)}{\partial x}\right)
\end{aligned} \qquad 2.38$$

These above equations are solved using the FDTD algorithm [33, 34] that solves simultaneously for the $E(r,t)$and $H(r,t)$ fields rather than using the wave equation and solving for only the electric field (or magnetic field). As illustrated in Fig. 2.2, the FDTD algorithm centers the $E(r,t)$ and $H(r,t)$ components in a three-dimensional space grid in such a manner that every $H(r,t)$ component is surrounded by four circulating $E(r,t)$ components and vice versa.

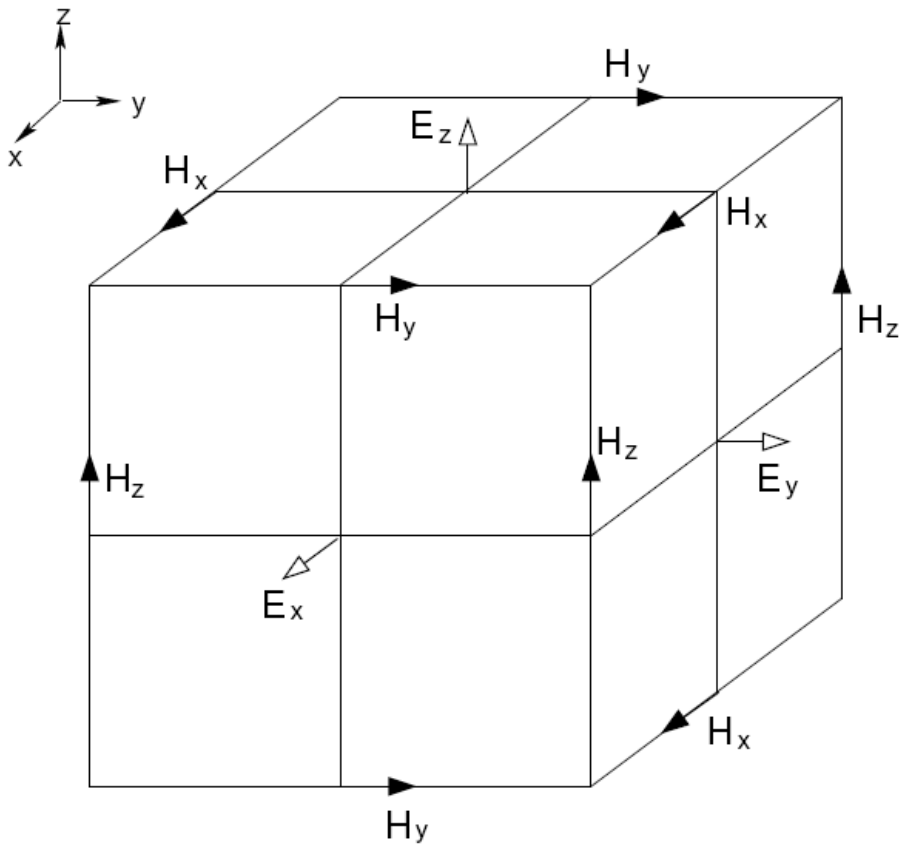

Figure 2.2: Positions of the components of $E(r,t)$ and $H(r,t)$ fields about a cubic cell of the Yee spatial lattice.

Moreover, the $E\,(r;\,t)$ and $H\,(r;\,t)$ components in time are computed in a "leapfrog" arrangement. Thus at a particular time step, using previously stored $H(r;\,t)$ data, all the $E(r;\,t)$ computations in the simulation domain are performed and the results stored. Subsequently, using the $E\,(r;\,t)$ data just computed, all of the $H(r;\,t)$ computations are performed and the results stored. This leapfrogging cycle continues with the new $E(r;\,t)$ components being recomputed based on the newly obtained $H(r;\,t)$, until finally the time-stepping is concluded.

We denote any function, $\xi(x,y,z,t)$, of space and time as

$$\xi^n(i,j,k) = \xi(i\Delta x, j\Delta y, k\Delta z, n\Delta t) \tag{2.39}$$

and use second-order accurate, center-difference finite-difference expressions for both space and time derivatives, i.e.

$$\frac{\partial \xi}{\partial x}(i\Delta x, j\Delta y, k\Delta z, n\Delta t) = \frac{\left(\xi^n\left(i+\frac{1}{2},j,k\right) - \xi^n\left(i-\frac{1}{2},j,k\right)\right)}{\Delta x} + O[\Delta x^2]$$

$$\frac{\partial \xi}{\partial t}(i\Delta x, j\Delta y, k\Delta z, n\Delta t) = \frac{\left(\xi^{n+\frac{1}{2}}(i,j,k) - \xi^{n-\frac{1}{2}}(i,j,k)\right)}{\Delta t} + O[\Delta t^2] \tag{2.40}$$

The applications of the above definitions for numerically approximating the Maxwell's equations in a material medium yields for Eq. 2.17 and 2.20:

$$\frac{E_x^n\left(i+\frac{1}{2},j,k\right) - E_x^{n-1}\left(i+\frac{1}{2},j,k\right)}{\Delta t} = \frac{1}{\epsilon}\left[\frac{\left(H_z^{n-\frac{1}{2}}\left(i+\frac{1}{2},j+\frac{1}{2},k\right) - H_z^{n-\frac{1}{2}}\left(i+\frac{1}{2},j-\frac{1}{2},k\right)\right)}{\Delta y} - \frac{\left(H_y^{n-\frac{1}{2}}\left(i+\frac{1}{2},j,k+\frac{1}{2}\right) - H_y^{n-\frac{1}{2}}\left(i+\frac{1}{2},j,k-\frac{1}{2}\right)\right)}{\Delta z}\right] \tag{2.41}$$

$$\frac{H_x^{n+\frac{1}{2}}\left(i,j+\frac{1}{2},k+\frac{1}{2}\right)-H_x^{n-\frac{1}{2}}\left(i,j+\frac{1}{2},k+\frac{1}{2}\right)}{\Delta t}$$

$$=\frac{1}{\mu_0}\left[\frac{\left(E_y^n\left(i,j+\frac{1}{2},k+1\right)-E_y^n\left(i,j+\frac{1}{2},k+1\right)\right)}{\Delta z}\right.$$

$$\left.-\frac{\left(E_z^n\left(i,j+1,k+\frac{1}{2}\right)-E_z^n\left(i,j,k+\frac{1}{2}\right)\right)}{\Delta y}\right]$$

Rearranging the above equations results in the following discrete equation, which can then be directly used for time-stepping:

$$E_x^n(i+\frac{1}{2},j,k$$

$$=E_x^{n-1}\left(i+\frac{1}{2},j,k\right)$$

$$+\frac{\Delta t}{\epsilon}\left[\frac{\left(H_z^{n-\frac{1}{2}}\left(i+\frac{1}{2},j+\frac{1}{2},k\right)-H_z^{n-\frac{1}{2}}\left(i+\frac{1}{2},j-\frac{1}{2},k\right)\right)}{\Delta y}\right. \quad 2.42$$

$$\left.-\frac{\left(H_y^{n-\frac{1}{2}}\left(i+\frac{1}{2},j,k+\frac{1}{2}\right)-H_z^{n-\frac{1}{2}}\left(i+\frac{1}{2},j,k-\frac{1}{2}\right)\right)}{\Delta z}\right]$$

$$H_x^{n+\frac{1}{2}}\left(i,j+\frac{1}{2},k+\frac{1}{2}\right)$$

$$= H_x^{n-\frac{1}{2}}\left(i,j+\frac{1}{2},k+\frac{1}{2}\right)$$

$$+\frac{\Delta t}{\mu_0}\left[\frac{\left(E_y^n\left(i,j+\frac{1}{2},k+1\right)-E_y^n\left(i,j+\frac{1}{2},k\right)\right)}{\Delta y}\right.$$

$$\left.-\frac{\left(E_z^n\left(i+,j+1,k+\frac{1}{2}\right)-E_z^n\left(i,j,k-\frac{1}{2}\right)\right)}{\Delta y}\right]$$

The finite difference equations corresponding to Eqs. (2.38) can be similarly constructed. Note that the location of the $E(r;\ t)$ and $H(r;\ t)$ components on the spatial grid shown in Fig. 2.2, and the central difference operations on these components automatically enforce the divergence Eqs. (2.37); thus the above solution solves the complete system of equations (2.36, 2.37) for a homogeneous, linear, and nondispersive medium.

2.4 DIFFERENCE BETWEEN GREEN'S FUNCTION METHOD AND FDTD

Every theoretical method has its advantages and disadvantages. As we have described, we used the Green's function method incorporated with a reduced Rayleigh equation approach in this dissertation. There are several advantages. First, our approach

gives better physical insight of the scattering process as the scattering amplitudes clearly show how the incident SPP is coupled to different modes while FDTD only gives the field distribution after a certain time. Second, our approach leads to more accurate result compared to FDTD. As long as the code converges, we get exact solution of the field distribution. While for FDTD, different grid size and step size always leads to error, no matter how small the grid size chosen. Third, our approach can separate SH from FF during the calculation while for FDTD, everything has to be calculated together. Fourth, our approach saves time compared to FDTD. However, FDTD is very robust and can be easily used in different systems. Our approach includes an analytical derivation for different defect shape, which is not as easily implemented in FDTD.

Bibliography

[1] H. Raether, "Surface Plasmons on Smooth and Rough Surfaces and on Gratings" volume 111, Springer-Verlag, (1988)

[2] J. D. Jackson, Classical Electrodynamics (Wiley, Hoboken, NJ, 1999).

[3] W. H. Press, S. A. Teukoisky, W. T. Vetterling, and B. P. Flannery, Numerical Recipes in C (Cambridge University Press, Cambridge, UK, 1992).

[4] A. A. Maradudin, "Topics in condensed matter physics", 33, (1994)

[5] D. Krause, "Optical surface second harmonic measurements of isotropic thin-film metals: Gold, silver, copper, aluminum, and tantalum", J. App. Phys. 96, 3626, 1786341 (2004)

[6] K. S. Yee, "Numerical solution of initial boundary value problems involving Maxwells equations in isotropic media," *IEEE Tran. Antennas and Propag.*, vol. 14, pp. 302-307, (1966).

[7] A. Taflove and S. C. Hagness, "*Computational Electrodynamics: The Finite Difference Time-Domain Method"*, Artech House, Inc., 2nd edition, (2000).

Chapter 3

Surface second-harmonic generation from surface plasmon waves scattered by metallic nanostructures

Abstract

In this chapter, my coworkers and I analyzed second-harmonic (SH) generation from scattering of surface plasmon polaritons (SPPs) by one-dimensional metallic nanostructures. The electromagnetic field at the fundamental frequency (FF) is calculated by using a formalism based on the reduced Rayleigh equations, in which the arbitrary shape of the nanostructure is accounted for by means of the impedance boundary condition. The near field at the FF, the induced nonlinear-source surface polarization at the SH, and the associated multipole moments up to second order are calculated from this fundamental field. The dependence of near field and radiated optical power at the SH on the SPP wavelength and nanostructure geometry is then investigated.

3.1 INTRODUCTION

Surface plasmon polaritons (SPPs) have attracted a great deal of attention in recent years in several areas of nanooptics and chemistry [1–20]. SPPs are p-polarized strongly localized surface waves that form at metal-dielectric interfaces [21–25]. Because they are bound at an interface and are sensitive to its dielectric properties, SPPs are ideal tools to sense surface-interfacial properties. Equally important, the unusual dielectric properties of metals provide unique functionalities for use in ultrasmall nanodevices. Thus, metallic nanostructures have found widespread use in optical sensor applications [27] [28], linear [2–6] and nonlinear [18–20] plasmonic nanodevices, and photochemical processes. [11],[12]. Besides its high degree of localization in metal structures, the electromagnetic field of either localized or propagating SPP modes is greatly enhanced compared to the incident excitation field. As a result, the excitation of SPPs at metal nanoparticles or surface defects on a metal-dielectric interface represents an efficient interface-selective probing method, especially when nonlinear optical or chemical processes are employed. For example, it has already been demonstrated that the excitation of SPPs greatly increases the efficiency of nonlinear optical effects such as surface-enhanced Raman scattering (SERS) [7–10] or second-harmonic generation (SHG).[13–19],[23–25]. Because of the lack of dipole-allowed optical transitions in the bulk of centrosymmetric materials, SHG optical fields are generated only at interfacial regions of such materials. These fields exhibit a strong and complex dependence on the physical and chemical properties of surfaces and interfaces. As a result, second-harmonic (SH) fields, whether enhanced by plasmonic effects or not, have become an important surface diagnostic in surface science or colloidal chemistry. Surface SHG has been used to study a diverse set of surface phenomena and

applications, e.g., the symmetry properties of surfaces, the nature of adsorbates at surfaces or interfaces, or noninvasive probing of buried interfaces; this rapidly expanding body of research has been recently reviewed in several articles. [22–25].

In most previous studies of surface SHG, the pump or excitation source is a light beam. However, due to their strong spatial localization and efficient coupling to metallic nanostructures, SPPs can be used directly for excitation. In this case, a plasmon wave could, for example, be an effective probe of surface nanodefects. Thus, it is of interest to understand how propagating plasmon waves interact with a surface feature to produce SHG radiation. Such interactions could form the basis for a new approach for high-resolution imaging of surface features on nominally bare or on nanostructured surfaces. Whereas a considerable body of research has been devoted to understanding SHG through light scattering off metallic nanostructures (see, e.g., Ref. [26] and the review article [22] with the references therein), the nonlinear process of SHG by means of scattering of surface plasmon polaritons of metallic nanodefects has yet to be investigated. In the paper published, we analyzed this latter process, namely, generation of SH during scattering of an SPP, which is propagating on a flat metal-dielectric interface, by one-dimensional (1D) metallic nanostructures, such as linear ridges (protuberances) or grooves (indentations). Our analysis used a formulation based on the reduced Rayleigh equations [29] to first determine the total electromagnetic field at the fundamental frequency (FF). Subsequently, we computed the induced nonlinear surface polarization density at the SH and used it to compute the dominant multipoles in a series expansion. We then use these multipoles to calculate the electromagnetic field and its spectral distribution at the SH.

This chapter is organized as follows. In Sec. 3.2, I will introduce the analytical formulation of our problem and the numerical method we used to determine the electromagnetic field at both the fundamental frequency and the second harmonic. Furthermore, in Sec. 3.3, I will present our results obtained by solving the analytical model in the paper. Thus, we determine the spectral properties and the spatial distribution of the field at the fundamental frequency and second harmonic as well as the influence of the structure of the nanodefect on the scattering process. In the last section, I will summarize our results.

3.2 THEORETICAL APPROACH

In order to investigate SHG via scattering of SPP by metallic nanostructures, we consider a system consisting of a 1D metallic defect on a planar metal surface; the corresponding geometry is illustrated in Fig. 2.1. The surface profile is thus described by an x_1-dependent function, i.e., $x_3 = f(x_1)$, only. The incoming SPP propagates along the x_1 direction and, upon its interaction with the defect, it generates transmitted and reflected SPP waves as well as outgoing photon states (radiative modes). For the work in this paper, we chose the metal to be silver, which is characterized by the Drude model with dielectric constant $\epsilon(\omega) = 1 - \omega_p^2/\omega^2$, where ω_p is the plasma frequency of the metal and ω is the frequency of incident SPP. For silver, λ_p=157 nm. Note that in the description of the scattering process, the optical losses (via the damping frequency γ) can be neglected, as the size of the nanodefect is much smaller than the characteristic propagation length of the SPP. As a result, the scattering process conserves the total energy, a property that is very useful in analyzing the convergence rate of the numerical method used here. To

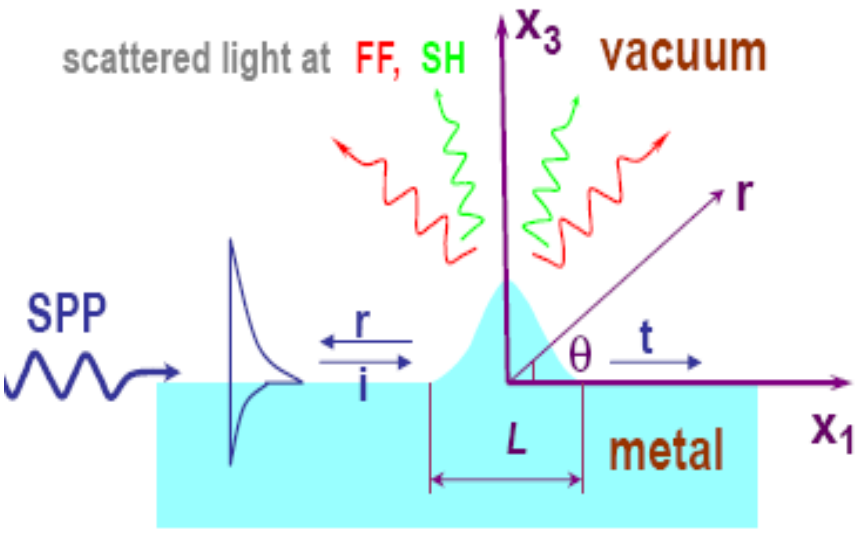

Fig. 3.1 Schematic of the scattering geometry and the radiated waves involved in the nonlinear scattering process. Fields in the region denoted by L=4a are integrated to calculate SHG.

calculate the electromagnetic field at the FF, we use the Rayleigh-equation approach [29] and express the only nonvanishing component of the magnetic field as

$$H_2^{\uparrow}(x_1, x_3) = \exp[ik(\omega)x_1 - \beta_0 x_3] + \int_{-\infty}^{\infty} \frac{dq}{2\pi} R(q,\omega) \exp[iqx_1 + i\alpha_0(q,\omega)x_3] \quad 3.1$$

where $H_2^{\uparrow}$ is the magnetic-field component in the x_2 direction, the arrow $\uparrow$ denotes the vacuum region, $k(\omega) = \sqrt{1 - 1/\epsilon(\omega)}\omega/c$ and $\beta_0(\omega) = \omega/[c\sqrt{-\epsilon(\omega)}]$ are the SPP wave vector and the decay constant in the vacuum, respectively, $\alpha_0(\omega) = \sqrt{\omega^2/c^2 - q^2}$, and $R(q,\omega)$ is the scattering amplitude. To calculate this scattering amplitude, we use a local impedance boundary condition, [30], which accounts for the planar surface perturbation centered at $x_3 = 0$,

$$\frac{\partial}{\partial x_3} H_2^{\uparrow}(x_1, x_3|\omega)|_{x_3=0}$$

$$= -\frac{\omega[1 + s(x_1)]}{c\sqrt{-\epsilon(\omega)}}\, H_2^{\uparrow}(x_1, x_3|\omega)|_{x_3=0} \tag{3.2}$$

The prefactor in the right-hand side of Eq. 3.2 is defined by the surface structure; namely, for small surface perturbations, the Fourier transform of the surface impedance function, $\hat{s}(q)$, is determined by the Fourier transform of the real-space surface profile, $\hat{f}(q)$, by the relation, [29], [30]:

$$\hat{s}(q) = -\frac{1 - \epsilon(\omega)}{d(\omega)\epsilon(\omega)}\, \hat{f}(q) \tag{3.3}$$

Where $d(\omega) = c/\left[\omega\sqrt{-\epsilon(\omega)}\right]$ is the optical skin depth.

By substituting Eq. (3.1) into Eq. (3.2), we obtain a Fredholm equation of the second kind whose solution determines the scattering amplitude,

$$T(q, \omega) = V\big(q, k(\omega)\big)$$

$$+ \int_{-\infty}^{\infty} \frac{dp}{2\pi} V(q|p) G_0(p, \omega) T(p, \omega) \tag{3.4}$$

where$V(q, p) = \beta_0(\omega)\hat{s}(q - p)$plays the role of a scattering potential, $T(q, \omega) = G_0^{-1}(q, \omega)R(q, \omega)$ is the rescaled scattering amplitude, and

$$G_0(p, \omega) = \frac{i\epsilon(\omega)}{\epsilon(\omega)\alpha_0(p, \omega) + \alpha(k, \omega)} \tag{3.5}$$

is Green's function of an SPP propagating on a planar surface.

Equation (3.4) is of central importance to our analysis of the field distribution at the FF: upon solving for the scattering amplitude $T(q,\omega)$, and then $R(q,\omega)$, we insert $R\,(q,\omega)$ into Equation (3.1) and calculate the magnetic field $H_2^{\uparrow}(x_1\,,x_3)$ in the vacuum region. Then, using Maxwell equations, we determine the nonvanishing components of the electric field at any point in the vacuum region,

$$\begin{aligned}\frac{\omega}{c}E_1^{\uparrow}(x_1,x_3) &= i\beta_0(\omega)\exp[ik(\omega)x_1-\beta_0(\omega)x_3]\\ &\quad+\int_{-\infty}^{\infty}\frac{dq}{2\pi}\alpha_0(q,\omega)R(q,\omega)\exp[iqx_1\\ &\quad+i\alpha_0(\omega)x_3]\end{aligned} \tag{3.6a}$$

$$\begin{aligned}\frac{\omega}{c}E_3^{\uparrow}(x_1,x_3) &= -k(\omega)\exp[ik(\omega)x_1-\beta_0(\omega)x_3]\\ &\quad-\int_{-\infty}^{\infty}\frac{dq}{2\pi}qR(q,\omega)\exp[iqx_1+i\alpha_0(\omega)x_3]\end{aligned} \tag{3.6b}$$

Here, E_1 and E_3 are the electric-field components in the x_1 and x_3 directions, repectively, thus yielding the complete set of fields for the linear scattering process.

In a phenomenological model that is widely used in studies of SHG at surfaces and interfaces, the electromagnetic field at the SH is viewed as being generated by two nonlinear polarization sources. The first consists of a sheet of surface nonlinear polarization, $P^{(2\omega)}$, occupying an interfacial domain of a few angstroms. Within this region, the material properties and the electromagnetic field undergo a steep transition between their bulk values in the two media. In addition, within this region the inversion symmetry is broken and therefore the surface nonlinear polarization induced at the SH is related to the electric field at the FF by a second-order nonlinear optical response.

$$P^{(2\omega)} = \chi_s^2 E^{(\omega)}(r) E^{(\omega)}(r) \delta\big(x_3 - f(x_1)\big) \quad 3.7$$

Here, χ_s^2 is the surface second-order susceptibility, whereas the Dirac function expresses the surface characteristic of the source polarization. In most cases of practical interest, the metal-vacuum interfaces possess an isotropic mirror-symmetry plane perpendicular to the interface. Under these circumstances, the surface nonlinear susceptibility χ_s^2 has only three independent components, namely, $\chi^2_{s\perp\perp\perp}$, $\chi^2_{s\perp\parallel\parallel}$, $\chi^2_{s\parallel\parallel\perp} = \chi^2_{s\parallel\perp\parallel}$, where $\perp$ and $\parallel$ refer to normal and perpendicular directions to the surface, respectively. Note that $\chi^2_{s\parallel\parallel\perp} \neq \chi^2_{s\parallel\perp\parallel}$ if the surface does not have an isotropic mirror plane, as is the case with metallic monocrystals cleaved along certain crystal symmetry planes or surfaces containing adsorbed chiral molecules. In our calculations, we assume the following values for the χ_s^2 components: , $\chi^2_{s\perp\perp\perp} = 5.02 \times 10^{-20} m^2/V$, $\chi^2_{s\perp\parallel\parallel} = 0$, $\chi^2_{s\parallel\parallel\perp} = \chi^2_{s\parallel\perp\parallel} = 1.13 \times 10^{-18} m^2/V$.

The second source for the electromagnetic field at the SH is the bulk nonlinear polarization, which in the case of isotropic centrosymmetric metals can be expressed as

$$P^{(2\omega)}_{bulk}(r) = \gamma\big[E^{(\omega)}(r) \cdot E^{(\omega)}(r)\big] \quad 3.8$$

Where $\gamma = e[1 - \epsilon(\omega)]/32\pi m\omega^2$ and e and m are the charge and mass of the electron, respectively. Note that although the two sources of SH have very different physical origins, namely, the surface nonlinear polarization stems from dipole allowed transitions, whereas the bulk (longitudinal) component originates from quadrupolar ones, their contributions to the SH are experimentally indistinguishable. [32]. Nevertheless, these two nonlinear polarization sources have largely different relative contributions to the SHG process, especially if is close to the frequency of resonantly excited SPPs. Thus, at this frequency, the contribution of the surface nonlinear polarization to the SHG is enhanced significantly

more than that of the bulk source. [33]. In addition, the spatial distribution of the SH is much more sensitive to variation in surface nonlinear polarization; indeed, recent experiments [34] have demonstrated that in the case of metals with good, i.e., low loss, optical properties (Ag, Au), the surface nonlinear susceptibility is about 2 orders of magnitude larger than the bulk one. As a final argument for the validity of neglecting the bulk contribution to the SH, note not only that the bulk component of the SH is smaller than the surface one but also that it is primarily generated within a thin layer with thickness comparable to the skin depth, which at optical frequencies is only 20 nm; therefore, if the defect size is considerably larger than the skin depth, the bulk contribution to the total SH can be safely neglected.

The electromagnetic field at the SH, generated by the surface nonlinear polarization, can be represented in terms of the multipole moments associated with $P_s^{2\omega}(r)$. As the nanodefect size is considerably smaller than the plasmon wavelength, $k(\omega)a \ll 1$, we have restricted our calculations to multipoles up to the second order, that is, the electric dipole moment, the magnetic dipole moment, and the electric quadrupole moment; they are defined by the following relations, [35]:

$$p = \int P^{(2\omega)}(r')dr' \tag{3.9a}$$

$$m = -\frac{i\omega}{2}\int r' \times P^{(2\omega)}(r')dr' \tag{3.9b}$$

$$Q(n) = \int \left\{3\left[\left(\widehat{r}\cdot r'\right)P^{(2\omega)}(r') + \left(\widehat{r}\cdot P^{(2\omega)}(r')\right)r'\right] - 2[(r'\cdot P^{(2\omega)}(r))\hat{r}]\right\}dr' \tag{3.9c}$$

Note that the polarization vector in Eq. (3.9) does not depend on the x_2 coordinate, so the integrals are calculated in the two-dimensional plane defined by the x1 and x3 coordinates. Therefore, the multipoles defined in Eq. (3.9) represent linear densities of the corresponding physical quantities. Moreover, since we are only interested in the SH radiation generated by the defect, the integral region is chosen to be $L = 4a$, as illustrated in Fig. 3.1. This characteristic size of the defect is defined by the spatial extent over which the electromagnetic field at the FF is strongly inhomogeneous, i.e., the size of the domain in which this field is markedly different from that of SPPs that propagate along a flat air-metal interface. As a result, we used the spatial distribution of the computed field at the FF to estimate the value of the characteristic length *L* over which we performed the integrals in Eq. (3.9). Finally, the SHG from SPPs propagating on flat surfaces [23] is a well understood process, so it is not considered here.

The angular distribution of the radiated power at the SH, originating from the multipoles in Eq. (3.9), is given by the following relations:

$$\frac{dP_{ed}}{d\theta} = \frac{Z_0 c^2 K^3}{16\pi} |(n \times p) \times n|^2 \quad \text{3.10a}$$

$$\frac{dP_{md}}{d\theta} = \frac{Z_0 K^3}{16\pi} |(n \times m) \times n|^2 \quad \text{3.10b}$$

$$\frac{dP_{eq}}{d\theta} = \frac{Z_0 c^2 K^5}{288\pi} \left|\left(n \times Q(n)\right) \times n\right|^2 \quad \text{3.10c}$$

where P_{ed}, P_{md} , and P_{eq} correspond to the electric dipole, magnetic dipole, and electric quadrupole, respectively, $k = 2\omega/c$ is the wave vector at the SH, and $Z_0 = \sqrt{\mu_0/\epsilon_0}$ is the vacuum impedance. As is well known from classical electrodynamics, at the smaller wavelengths considered here, the radiated energy comes primarily from the magnetic and

quadrupole moments ($P_{md}, P_{eq} \sim \lambda^{-5}$), while at longer wavelengths, the main contribution to the emitted energy comes from the electric-dipole moment ($P_{ed} \sim \lambda^{-3}$). Finally, the multipoles allow us to calculate not only the radiative field at 2ω but also the near field; the corresponding near-field formulas are not presented here due to their large size. [36].

3.3. RESULTS AND DISCUSSION

In what follows, we will illustrate how our formalism describes linear and nonlinear scatterings of SPPs by metallic nanostructures. For our calculations, we use as a model a small surface defect whose mathematical representation allows a convenient calculation of its Fourier transform. [29]. In particular, the surface structure is characterized by the function $f(x_1) = hexp(-\frac{x_1^2}{a^2})$, where $h > 0 (h < 0)$ is the height (depth) of the defect and $a/\sqrt{2}$ is its half-width (see Fig. 2.1). With these assumptions, we performed our calculations for two types of nanostructures, namely, ridges $h > 0$ and grooves $h < 0$. Specifically, we solved Eq. (2.1.4) numerically by using a method of quadrature on a uniform mesh with arbitrary weight. [37]. Convergence was reached when using around1000 discretization points, the relative error of the results being less than 5%. We then calculated the magnetic field, via Eq. (3.1), the electric field from Eq. (3.6), and the radiated power in Eq. (3.10), which correspond to the multipoles in Eq. (3.9).

3.3.1 SPP scattering at the fundamental frequency

Consider first the linear scattering process. The physics of this process is illustrated most clearly by a plot of the near-field distribution resulting from the scattering of an

incident SPP wave at a defect, say, a groove (see Fig. 2). As shown in the figure, a portion of the incident SPP is reflected back; this back reflected wave interferes with the incident wave to form a standing-wave pattern to the left of the defect in Fig. 3.2.

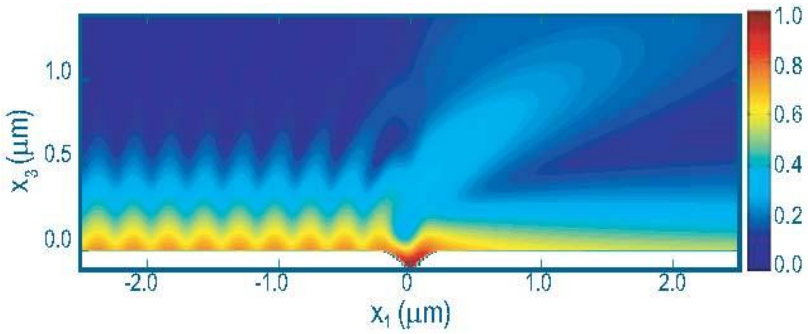

Fig. 3.2 Near-field distribution in vacuum, at FF,computed for Gaussian-shaped nano groove with width a=100 nm, h=−100 nm, and incident SPP wavelength λ=560 nm.

In addition, a portion of the incident SPP is transmitted through the defect. Finally, in this case of a groove, the scattering of the SPP is coupled into radiative modes and, thus, leads to emission of a narrow beam in a narrow angular range, leading to photonic nanojets [22] radiated in a narrow cone above the defect. In the case illustrated in Fig. 3.2, the nanojet has a spectral width of 450 nm and is emitted in the forward direction at an angle of ~45°.

The linear scattering process illustrated in Fig. 3.2 varies strongly with the plasmon wavelength and defect geometries. This variation is shown clearly by a plot of the normalized scattered intensity versus the plasmon wavelength given in Fig. 3.3. By scattered intensity, we mean the integrated optical radiation in the far field normalized by the intensity of the incident plasmon wave. Note that at long SPP wavelength, both groove

and ridge defects exhibit a monotonic decrease in scattered intensity with λ; this decrease simply reflects the expected long-wavelength behavior of scattering processes.

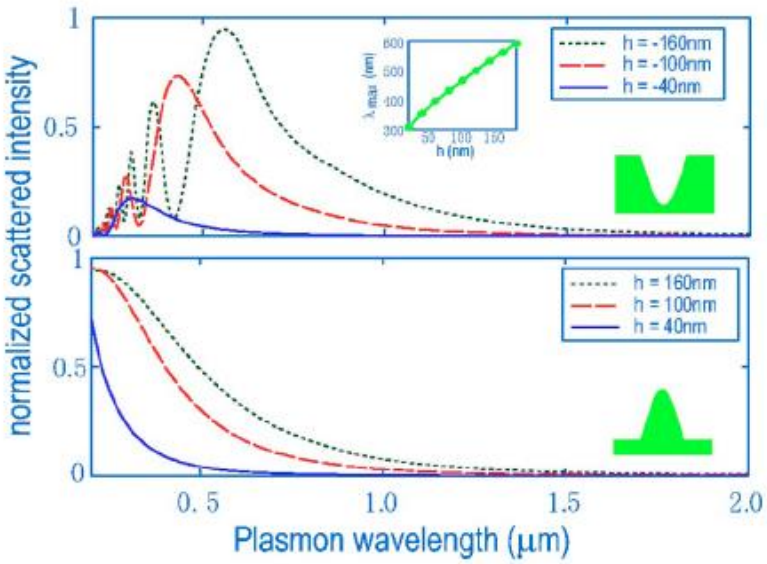

Fig. 3.3 Normalized SPP-FF conversion ratio vs the plasmon wavelength λ, computed for (a) grooves with a=100 nm and (b) ridges with a=120 nm, calculated for $\lambda_p = 157nm$. The inset in the top panel shows the plasmon wavelength for the first peak vs depth of grooves with groove with remaining constant a=100 nm.

Specifically, as shown in Ref. 28, for large SPP wavelength λ, the amount of energy of the SPP scattered into radiative modes (light) varies as $\sim\lambda^{-2}$. In addition, in the case of groove, the intensity of the emitted radiation exhibits a series of oscillations as the incident plasmon wavelength is varied. The fact that the oscillation period seen in the spectrum of the radiated light increases with the depth of the groove suggests that these oscillations

originate from cavity effects. For the ridge defect, in contrast, the intensity of the scattered light does not oscillate with increasing plasmon wavelength and in fact exhibits only a monotonic decrease with λ. Figure 3.3 shows that the scattered intensity increases rapidly with the defect height. Note also that the plasmon wavelength for the largest radiation peak, denoted by λ_{max}, redshifts as the defect height increases. The λ_{max}'s dependence on the defect depth is shown in the inset in Fig. 3.3.

Consider now the spatial distribution of the near field of the scattered light for different defect sizes, shapes, and different incident SPP wavelengths. In particular, consider the near field at both groove resonant and nonresonant wavelengths (see Fig. 3.4) and both for grooves and ridges. The first three panels in this figure show the spatial distribution of the electric field in the near proximity of a groove with a=100 nm and h=−160 nm, i.e., the green curve in Fig. 3.3, calculated at the wavelengths of the first two resonant peaks, λ=561 nm [Fig. 3.4(a)] and λ=370 nm (Fig. 3.4(c)), and the "intervalley" minimum, λ=424 nm [Fig. 4(b)]. While each of these figures shows field enhancement inside the groove, particularly near the metal-vacuum interface, the maximum enhancement is seen at the wavelength corresponding to the strongest resonance, i.e., oscillation peak in Fig. 3.3. For ridges, calculations of the near field show that the interaction with the nanodefect leads to strong spatial distortions in the field of the incoming SPP; these distortions increase with the defect size. As a result, larger defects are more efficient in coupling the plasmon wave into the radiative modes.

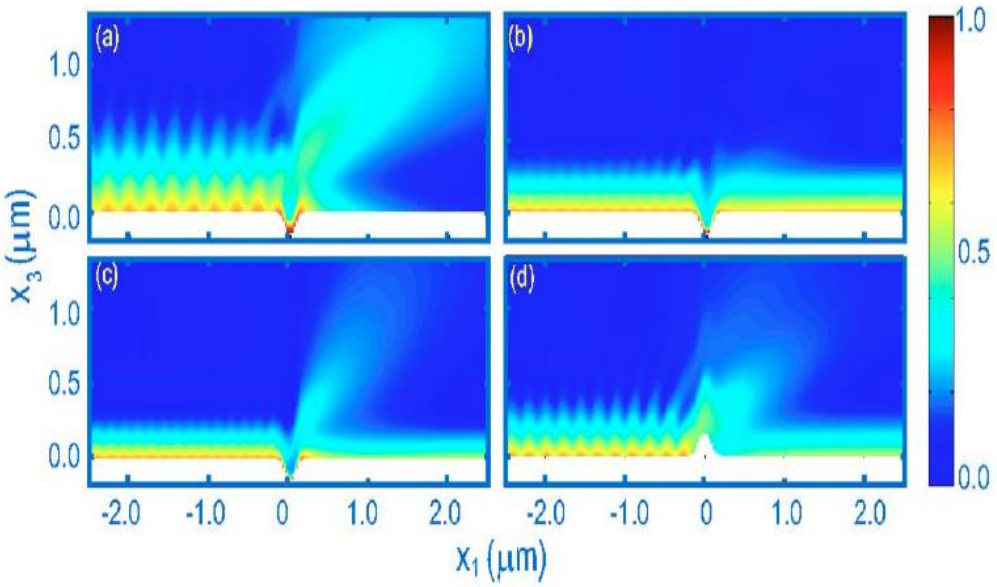

Fig. 3.4 Near-field distribution in vacuum, at FF, computed for Gaussian-shaped nanodefects with width a=100 nm. Plots (a), (b), and (c) correspond to grooves with h=−160 nm and incident SPP wavelengths λ=561 nm, λ=424 nm, and λ=370 nm, respectively. Panel (d) corresponds to a ridge with h=160 nm and λ=460 nm.

3.3.2 SPP scattering at second harmonic

Next, we consider SHG due to scattering of the SPPs by the metallic nanodefect. In particular, we determine both the 2ω far-field radiation spectrum and the spatial distribution of its near field. Both of these quantities may be obtained from the multipoles of the nonlinear surface polarization. To compute these multipoles, we calculate the integrals in Eq. (3.9) by discretizing the surface profile at the nanodefect in ~ 400 segments of equal length. Figure 3.5(a) presents the results of such calculations, performed in the

case of a groove with a=100 nm and h=−100 nm. As is typical in scattering, the SHG due to the electric dipole dominates at long wavelength ($\lambda > \sim -2\mu m$), whereas for smaller wavelengths all three multipoles make contributions of comparable magnitude. Note, however, that as the wavelength approaches the characteristic size of the defect, additional multipoles must be included in the calculations. We have restricted our calculations to $\lambda >$ 300nm, a cutoff value that ensures that the errors introduced by ignoring higher-order multipoles remain smaller than 1%. Furthermore, we have observed that the SHG process depends in a rather subtle way on the shape of the defect. At small wavelengths, the maxima of the quadrupole SHG coincide with the maxima of the total SHG, which suggests that the quadrupole SHG represents the dominant contribution. However, our calculations show that the resonant peaks in Fig. 3.3 correspond to the maxima in the spectrum of the *electric dipole* SHG. This result suggests that the spectral characteristics of the SHG depend not only on the strength of the field at the FF but also on its spatial distribution and the geometrical and physical characteristics of the surface, *i.e.*, the surface susceptibility tensor χ_s^2. More exactly, the strength of the electric dipole, magnetic dipole, and electric quadrupole, which are sources for the SH, are determined by the electric field through a surface integral of a sum of terms, each term being the product between a component of the susceptibility tensor and two field components [see Eq. 3.7]. These differences in the properties of SPP scattering at the FF and SH should not be surprising as it is well known that, for instance, due to their strong frequency dispersion, the localization properties of SPP at the FF are quite different from their localization effects at the SH. [22].

To gain a more in-depth understanding of the physical properties of the radiated SHG, we present in Fig. 3.5(b) the total SHG emitted by grooves, ridges, and a flat surface

(h=0), with the feature width a being the same. First, this figure shows that, at smaller λ, grooves radiate 10–100 times larger amount of power at the SH, as compared to ridges; this observation again suggests that grooves are more efficient nanostructures for light extraction from SPP excitations. In addition, note that the SHG spectra in Fig. 3.5(b) show several resonant features. In the case of ridges, this behavior is in contrast with that seen for the radiated power at the FF, which exhibited a monotonic decrease with wavelength (see Fig. 3.3). This finding again shows that the magnitude of scattered

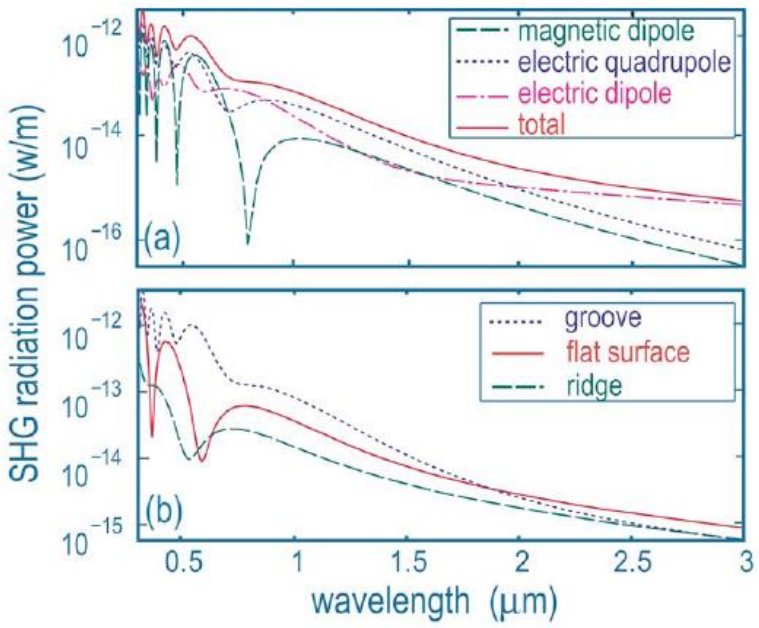

Fig 3.5 (a) SHG radiation power *vs*. plasmon wavelength, calculated for a groove with a=100 nm and h=−100 nm. Both the total SHG and its multipole components are presented. (b) The total SHG radiation power generated by grooves and ridges with a=100 nm and by a flat surface. The height (depth) of ridges (grooves) is h=100 nm (h=−100 nm).

SH light depends both on the geometry of the defect, since optical resonances are typically dependent on the geometry of the nanodefect, and on the electric field at the FF. Importantly, such frequency-selective optical response may allow optical detection of defects with specific geometries using surface spectroscopy optical probes. Finally, we observe that the amount of radiation corresponding to a flat surface is larger (smaller) than that corresponding to ridges (grooves); as expected, when $h \rightarrow 0$, i.e., the defect height or

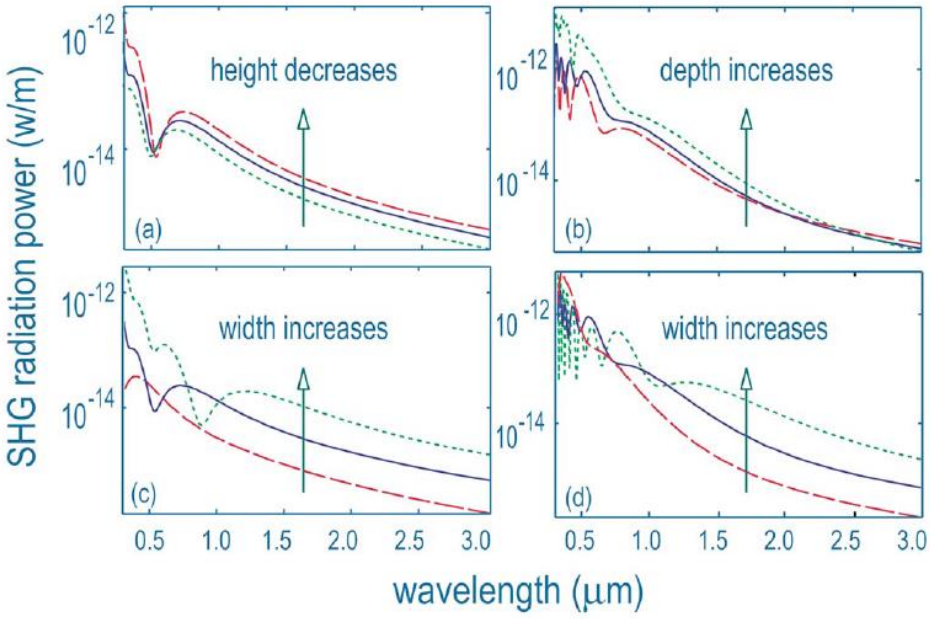

Fig. 3.6 A comparison of the spectral density of the SH radiated power computed for grooves and ridges. Left (right) panels correspond to ridges (grooves). In the top panels, a=100 nm and h=60 nm (dot green), h=100 nm (solid blue), and h=160 nm (dashed red); In the bottom panels, h=100 nm and a=60 nm (dot green), a=100 nm (solid blue), and a=160 nm (dashed red).

depth decreases to zero, the power of radiated SH light converges to the case of flat surface. In all cases, the amount of scattered SHG power corresponding to an incident SPP with a power per unit length of 1 W/m is 10^{-6}–10^{-8} W/m.

In as much as the particular geometry of the nanostructure appears to be the main factor that determines the power in the SHG radiation for a fixed incident SPP wavelength λ, we have investigated the dependence of the SHG power on the geometrical parameters of the metallic nanostructure, namely, the width a and height h. The results of these calculations are presented in Fig. 3.6 for two different choices of λ and defect shapes. This figure shows that in the case of ridges, the scattered SH power decreases as h increases, a counterintuitive result that is explained by the reduced field excitation at the surface of ridges with increasing h. Thus, our calculations show that as the defect height increases, the magnitude of the electric field and, consequently, the nonlinear surface polarization at the back side of the defect decreases (see Fig. 3.4(d)). Since the multipole moments are calculated by integrating the nonlinear surface polarization over the surface of the whole defect, smaller field excitation over the defect area leads to smaller multipole moments; as a result, the SHG radiation power decreases. In contrast, for the case of groove, deeper defects generate more SH radiation in the wavelength region where the electric quadrupole moment dominates. In addition, the SH spectra show a series of resonances, which, as in the linear case, are redshifted with the increase in the depth of a groove. Finally, Figs. 3.6(a) and 3.6(d) illustrate that for a fixed h, the amount of SH radiated by both ridges and grooves increases with the width a.

In many cases of practical importance, valuable information about the properties of surfaces and interfaces can be extracted not only from the excitation-wavelength

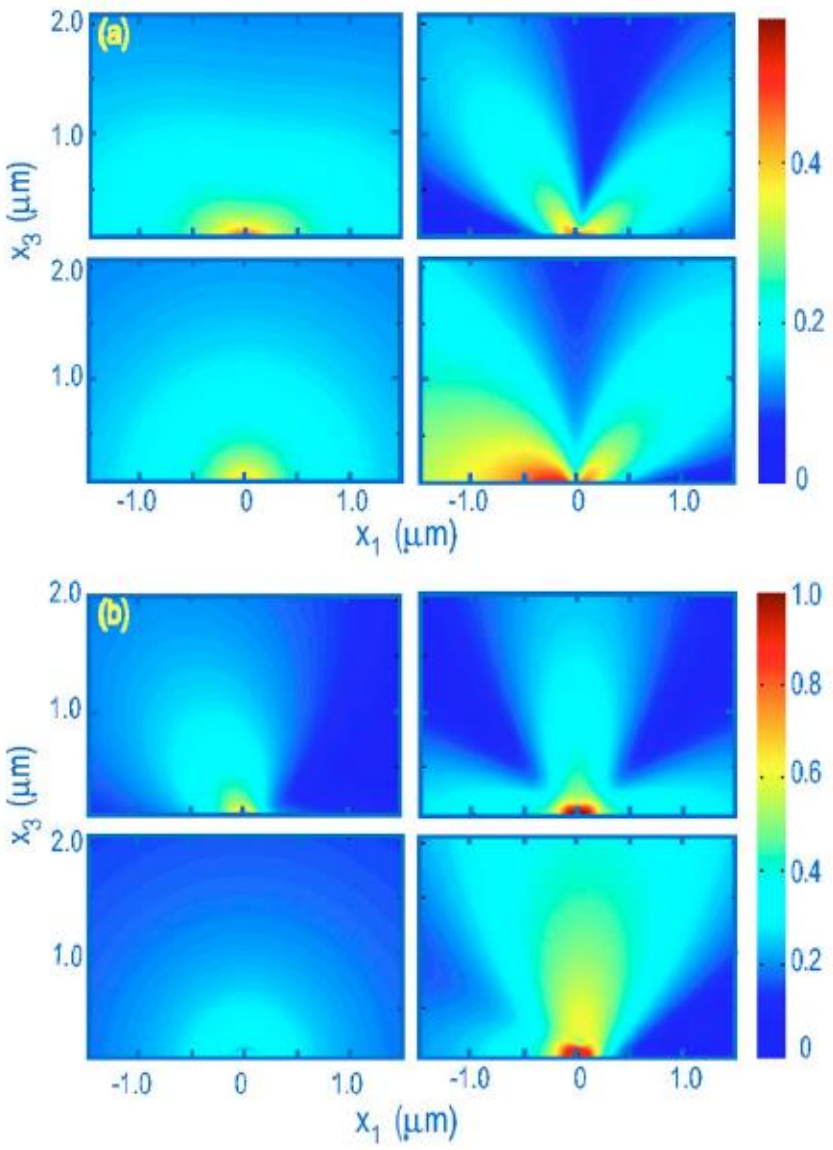

Fig. 3.7 Second-harmonic near-field distribution, computed for Gaussian-shaped nanodefects for the region above the surface, with (a) width a=100 nm, height h=100 nm, and incident SPP wavelength λ=512 nm and (b) a=100 nm, h=−100 nm, and λ=1.33μm. Clockwise, panels correspond to the electric dipole, electric quadrupole, total field, and magnetic dipole.

dependence of the SH signal but also from its near-field distribution. To illustrate this point, we have calculated the spatial distribution of the SH field in the near proximity of the nanodefect; the results for two generic cases are presented in Fig. 3.7. Since the near-field distribution is strongly dependent on the relative strength of the multipole moments, this field profile and angular distribution will in turn be strongly dependent on the wavelength of the SPP. For example, in Fig. 3.7 the SPP wavelength was chosen so that the three dominant multipole moments each make contributions of comparable magnitude to the total field. The total electric field in Fig. 3.7 is the sum of the fields generated by the electric dipole, magnetic dipole, and electric quadrupole. Since there are phase differences among the three terms, the total field is not simply the sum of the field amplitudes. Note also that the near-field distribution at the SH is markedly different from that at the FF, which can make the SH imaging a useful tool for nonlinear optical probing of surfaces.

3.4 CONCLUSIONS

In conclusion, we have presented a comprehensive description of the surface SH generated by surface plasmon scattering from metallic nanodefects at metal-dielectric interface. Our formalism has a wide applicability, as it can be used to study metallic nanostructures of arbitrary shape and can describe metals whose dielectric constant is described by a Drude or Lorentz model, that is, most metals with good optical properties. Our results clearly show that the properties of the emitted SH are highly sensitive to the material and geometrical characteristics of the metallic surface or metal dielectric interface, through the surface susceptibility $\chi_s^{(2)}$ and surface profile function $f(x_1)$. As a result, scattering of SPPs by metallic nanostructures can be a powerful alternative in noninvasive

spectroscopy studies of chemical and physical properties of surfaces and interfaces. Specifically, our study demonstrates that this SHG can provide unique information not only about the material parameters of the surface, e.g., the components of surface nonlinear susceptibility tensor, but also give valuable insight into the geometry and symmetry properties of the metallic nanostructures. Finally, since the surface nonlinear susceptibility $\chi_s^{(2)}$ is strongly dependent on the nature of the surface or interface, the formalism introduced has applicability to measurements of molecular adsorbates at interfaces or on metallic surfaces.

Bibliography

[1] T. W. Ebbesen, H. J. Lezec, H. F. Ghaemi, T. Thio, and P. A. Wolff, Nature (London) 391, 667 (1998).

[2] S. I. Bozhevolnyi, J. Erland, K. Leosson, P. M.W. Skovgaard, and J. M. Hvam, Phys. Rev. Lett. 86, 3008 (2001).

[3] S. I. Bozhevolnyi, V. S. Volkov, E. Devaux, J. Y. Laluet, and T. W. Ebbesen, Nature (London) 440, 508 (2006).

[4] S. K. Gray and T. Kupka, Phys. Rev. B 68, 045415 (2003).

[5] X. P. Zhang, B. Q. Sun, R. H. Friend, H. C. Guo, D. Nau, and H. Giessen, Nano Lett. 6, 651 (2006).

[6] W. Nomura, M. Ohtsu, and T. Yatsui, Appl. Phys. Lett. 86, 181108 (2005).

[7] S. M. Nie and S. R. Emery, Science 275, 1102 (1997).

[8] K. Kneipp, Y. Wang, H. Kneipp, L. T. Perelman, I. Itzkan, R. R. Dasari, and M. S. Feld, Phys. Rev. Lett. 78, 1667 (1997).

[9] C. L. Haynes and R. P. Van Duyne, J. Phys. Chem. B 107, 7426 (2003).

[10] R. M. Roth, N. C. Panoiu, M. M. Adams, R. M. Osgood, C. C.Neacsu, and M. B. Raschke, Opt. Express 14, 2921 (2006).

[11] R. M. Osgood and D. J. Ehrlich, Opt. Lett. 7, 385 (1982).

[12] C. J. Chen and R. M. Osgood, Phys. Rev. Lett. 50, 1705 (1983).

[13] H. J. Simon, D. E. Mitchell, and J. G. Watson, Phys. Rev. Lett. 33, 1531 (1974).

[14] A. V. Baranov, Y. S. Bobovich, and V. I. Petrov, Opt. Spektrosk. 58, 578 (1985).

[15] C. K. Johnson and S. A. Soper, J. Phys. Chem. 93, 7281 (1989).

[16] R. Antoine, P. F. Brevet, H. H. Girault, D. Bethell, and D. J. Schiffrin, Chem. Commun. (Cambridge) 1997, 1901.

[17] E. C. Hao, G. C. Schatz, R. C. Johnson, and J. T. Hupp, J. Chem. Phys. 117, 5963 (2002).

[18] A. Bouhelier, M. Beversluis, A. Hartschuh, and L. Novotny, Phys. Rev. Lett. 90, 013903 (2003).

[19] W. Fan, S. Zhang, N. C. Panoiu, A. Abdenour, S. Krishna, R. M. Osgood, K. J. Malloy, and S. R. J. Brueck, Nano Lett. 6, 1027 (2006).

[20] N. C. Panoiu and R. M. Osgood, Nano Lett. 4, 2427 (2004).

[21] H. Reather, Surface Polaritons on Smooth and Rough Surfaces and on Gratings (Springer-Verlag, Berlin, 1995).

[22] A. V. Zayats, I. I. Smolyaninov, and A. A. Maradudin, Phys. Rep. 408, 131 (2005).

[23] T. F. Heinz, in Nonlinear Surface Electromagnetic Phenomena, edited by H. E. Panath and G. I. Stegeman (Elsevier, Amsterdam, 1991), p. 353.

[24] J. I. Dadap, J. Shan, and T. F. Heinz, J. Opt. Soc. Am. B 21, 1328 (2004).

[25] K. B. Eisenthal, Chem. Rev. (Washington, D.C.) 106, 1462 (2006).

[26] S. I. Bozhevolnyi and K. Pedersen, Surf. Sci. 377-379, 384 (1997).

[27] J. L. West and N. J. Halas, Annu. Rev. Biomed. Eng. 5, 285 (2003).

[28] G. Boisde and A. Harmer, Chemical and Biochemical Sensingwith Optical Fibers and Waveguides (Arthech House, Boston,1996).

[29] J. A. Sanchez-Gil and A. A. Maradudin, Phys. Rev. B 60, 8359 (1999).

[30] A. A. Maradudin, in Topics in Condensed Matter Physics, edited by M. P. Das (Nova Science, New York, 1994), p. 33.

[31] J. E. Sipe, V. C. Y. So, M. Fukui, and G. I. Stegeman, Phys. Rev. B 21, 4389 (1980).

[32] J. E. Sipe, V. Mizrahi, and G. I. Stegeman, Phys. Rev. B 35, 9091 (1987).

[33] G. S. Agarwal and S. S. Jha, Solid State Commun. 41, 499 (1982).

[34] D. Krause, C. W. Teplin, and C. T. Rogers, J. Appl. Phys. 96, 3626 (2004).

[35] J. I. Dadap, J. Shan, K. B. Eisenthal, and T. F. Heinz, Phys. Rev. Lett. 83, 4045 (1999).

[36] J. D. Jackson, Classical Electrodynamics (Wiley, Hoboken, NJ, 1999).

[37] W. H. Press, S. A. Teukoisky, W. T. Vetterling, and B. P. Flannery, Numerical Recipes in C (Cambridge University Press, Cambridge, UK, 1992).

Chapter 4

Surface Second Harmonic Generation from Scattering of Surface Plasmon Polaritons from Radially Symmetric Nanostructures

Abstract

We present a comprehensive study of linear and nonlinear effects observed in the scattering process of surface plasmon polaritons (SPP) from localized two-dimensional surface deformations at a metal/dielectric interface. Thus, the electromagnetic field at the fundamental frequency (FF), for both p- and s-polarizations, is first determined by solving the corresponding set of reduced Rayleigh equations. The complete solution of these equations allows us to investigate both the complex structure of the scattered electromagnetic field as well as subtle mechanisms by which incident SPPs are scattered into radiative modes (light) and outgoing SPP waves. Furthermore, the electromagnetic field at the FF is used to determine the nonlinear surface polarization at the second harmonic (SH) and subsequently both the electromagnetic field distribution as well as the amount of light generated at the SH. Calculations are performed for three geometries that are relevant in many experiments, namely, Gaussian, hemispherical, and cylindrical nanodefects. Finally, throughout our analysis, we discuss potential applications of our findings to surface spectroscopy, surface chemistry, or new imaging techniques of surface nanodefects.

4.1 INTRODUCTION

Over the last few years, we have witnessed a renewed interest in both the physical properties of surface plasmon polaritons (SPPs) as well as their use in nanodevices with new or improved functionality. In particular, recent advances in materials, surface science, and nanofabrication techniques have made possible the design and experimental implementation of new plasmonic nanostructures and nanodevices, which exhibit remarkable physical properties and a great potential for advanced technological applications. To this end, of particular interest has been the optical properties of SPPs, [1-29], which are strongly localized *p*-polarized surfaced waves formed at the interface between a metal and a dielectric, [30 -33], as well as their interaction with metallic nanostructures. [34 – 36]. One of the consequences of the extreme light localization at metal/dielectric interfaces or close to the surface of metallic nanoparticles, is that extended (propagating waves) or localized surface plasmon polaritons can be used to achieve strong enhancement of the electromagnetic field, a property with important technological applications. To be more specific, this property can be employed to design new linear plasmonic devices, [1-9], detectors and other photovoltaic devices (solar cells), [14-17] optical sensors, [38,39], or study a series of photochemical processes. [18, 19]. In addition, and also of particular importance for practical applications, the strong enhancement of the electromagnetic field leads to the possibility to achieve strong nonlinear optical effects, such as second harmonic generation (SHG) [20-28], [30 36] and surface enhanced Raman scattering (SERS), [10-13] at remarkably low optical power.

Surface SHG has become an essential diagnostic tool for physical chemistry, non-invasive surface analysis, and catalytic chemistry, chiefly because this nonlinear optical

wave interaction is strongly dependent on the physical properties and local structure of surfaces and interfaces. This sensitivity of SHG is particularly important if one considers SHG at the surface of a centrosymmetric material, as in this case the lack of dipole-allowed optical transitions in the bulk of such materials leads to the vanishing of the otherwise dominant bulk SHG. In this case, the total SH signal is generated within a layer of only a few Ångstroms thickness, and therefore it is strongly dependent on the physical structure of this surface layer or its chemical properties, e.g. the nature of adsorbates at the surface or interface. In addition, surface SHG is a useful probing technique because it is non-invasive and has micrometer-scale spatial resolution. Moreover, the properties of surface SHG process, e.g. the polarization of the generated signal and the spatial distribution of the near- and far-field, are markedly different from those of the corresponding linear scattering process, and further enabling this nonlinear optical process to be a unique tool for the analysis of surfaces and interfaces.

In the standard approach to nonlinear surface probing, a laser source illuminates a surface and the scattered radiation is detected. In some cases metal particles are present on the surface and in that case it is well known that the scattering process is enhanced via the excitation of local surface plasmon-polariton modes in the metal object. More recently the interest in propagating plasmon polaritons has led several groups to consider the use of these waves as the primary probing source of surface features. Indeed recent beautiful work involving photoemission electron microscopy studies of illuminated surfaces [37] has shown that this approach is not only useful but can also provide a route to examine coherent plasmon effects. The question then arises as to whether this “plasmon-source" approach could also provide a useful source to examine surface features via nonlinear

surface wave excitation. Such an approach would have the advantage of a closer coupling of the excitation source with the surface feature to be examined. Further it would also be possible to envision using non optical excitation means such as injected electrons. Thus, in this paper we examine the physics of two-dimensional (2D) wave scattering from surface nanodefects. In fact we extend our earlier analysis [27] of the SHG from scattering of SPP waves from one-dimensional (1D) surface nanodefects to the more realistic case of two-dimensional, radially symmetric surface nanodefects. Importantly, our analysis does not simply extends the results obtained in the 1D case to the 2D geometry, as the latter case presents an additional complexity that stems from the more intricate polarization properties of the electromagnetic field that is generated near a 2D metallic nanodefect. Thus, unlike the 1D case, when both the SPP waves and the radiated light are *p*-polarized, in the 2D case the radiative modes have both *s*- and *p*-polarized components. This increased degree of complexity has important implications for the structure of the near- and far-field angular distribution and the magnitude of emitted radiation, both at the fundamental frequency (FF) and at the second harmonic (SH).

The chapter is organized as follows. In Sec. 4.2, we introduce the analytical formulation of our problem and the numerical method we used in our approach. Thus, we introduce a set of coupled reduced Rayleigh equations, whose solution fully determines the electromagnetic field at the FF. Also, we introduce the numerical method used to solve this system of equations. Moreover, we describe our approach to determine the electromagnetic field and the amount of emitted radiation at the SH, from the electromagnetic field at the FF. In Sec. 4.3, we present our results obtained by solving this analytical model. Thus, we consider three different radially symmetric surface nanodefects, namely Gaussian,

hemispherical, and cylindrical nanodefects, and for each of them we determine the spectral properties and the spatial distribution of the field at the FF and SH, Also, we investigate the influence of the geometrical structure of the nanodefect on the scattering process. In the last section, we summarize our results.

4.2 THEORETICAL APPROACH AND NUMERICAL ALGORITHM

In this section we present the theoretical formalism used to analyze the scattering of SPPs from surface metallic nanodefects as well as the numerical method used in our analysis. Our calculations provide the spatial distribution of the electromagnetic field and the spatial pattern of the radiated light, both at the FF and the SH.

4.2.1 Linear scattering of surface plasmon polaritons

In order to study the scattering process of SPP waves from surface nanodefects, we consider a system consisting of a SPP wave propagating on a planar metallic surface located in the (x_1 ,x_2)-plane, a wave that is incident onto a surface nanodefect; the corresponding geometry is illustrated in Fig. 4.1. The surface profile, which for the sake of simplicity is chosen to be radially symmetric, is described by a surface profile function $x_3 = \zeta(x_\parallel)$, where $x_\parallel = (x_1, x_2)$, For the function $\zeta(x_\parallel)$, which describes the shape of the surface nanodefect, we considered three choices, namely a Gaussian, $\zeta(x_\parallel) = h\exp(-x_\parallel^2/R^2)$, with height h and width R; a cylinder, $\zeta(x_\parallel) = h, x_\parallel \leq R$, with height h and radius R; and a spherical cap, $\zeta(x_\parallel) = \sqrt{R^2 - x_\parallel^2} - \sqrt{R^2 - \rho^2}, x_\parallel \leq \rho$, with R and ρ

the radius of the sphere and the cap, respectively. Note that with these choices for the surface profile function $\zeta(x_{\parallel})$, we can study surfaces with both protuberances (h > 0) and indentations (h < 0). The incoming SPP propagates along the x_1 direction and, upon its interaction with the surface nanodefect, generates scattered SPP waves as well as radiative modes (photon states), which propagate outwardly, away from the nanodefect.

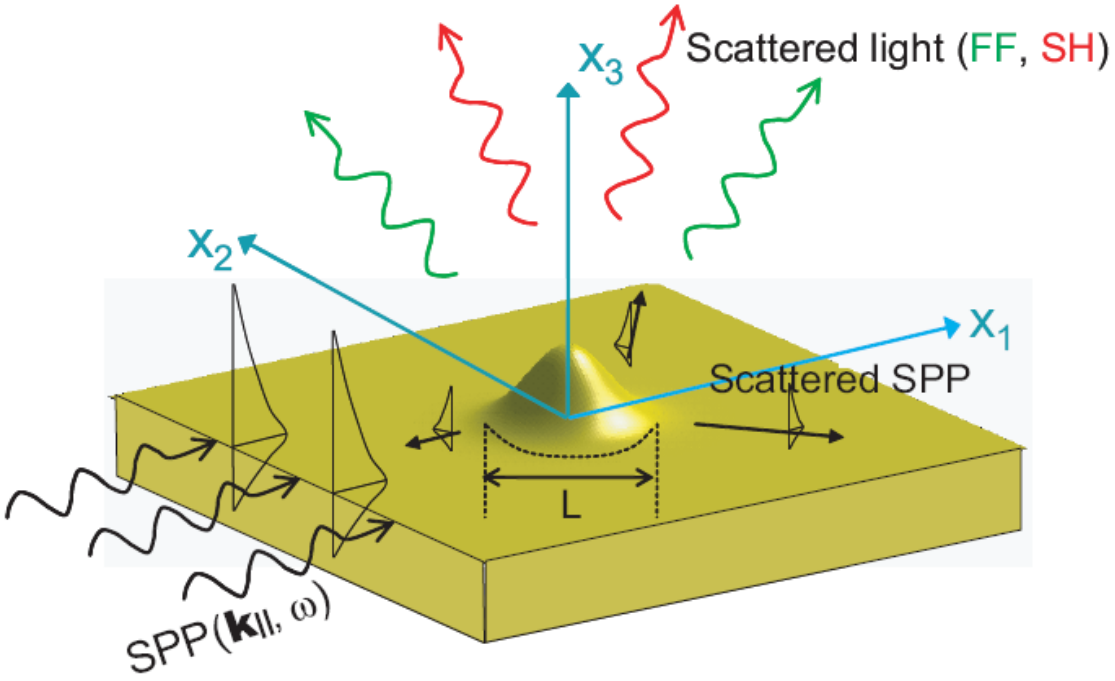

Fig 4.1 Schematic of the scattering geometry and the radiated waves involved in the nonlinear scattering process. Fields in the region denoted by L = 3.5R are integrated to calculate SHG.

We consider that the SPP propagates at the interface between vacuum and a metal, which is chosen to be silver in our calculations; the extension to the more general case of a

dielectric/metal interface is trivial. The electromagnetic properties of the metal are modeled via a dielectric function that obeys the Drude model, $\epsilon(\omega) = 1 - \omega_p^2/\omega^2$, while ω_p is the plasma frequency of the metal and ω is the frequency. For silver, the corresponding plasma wavelength is ω_p = 145.9 nm. [40]. Note that this choice for the metal dielectric function does not take into account the optical losses, that is, the imaginary part of $\epsilon(\omega)$ is set to zero; however, this is a good approximation since the characteristic size of the nanodefect is much smaller than the plasmon absorption length and therefore only a negligible amount of energy is dissipated during the scattering process. As a result, the electromagnetic energy is conserved during the scattering process. Accounting for loss is relatively straightforward since its effect on the wave is over a scale size which is much longer than that of the scatterer.

In order to analyze the scattering process of the SPP wave at the FF, we employ a method based upon a set of coupled reduced Rayleigh equations. [31,41,43,44]. To begin with, it is assumed that in the vacuum region, $x_3 > \zeta(x_\parallel)$, the amplitude $E(x, \omega)$ of the electric field, which is defined by the harmonic dependence $E(x, t) = E(x, \omega)e^{i\omega t}$, consists of the incident SPP wave and a scattered field that contains both radiative modes (scattered light) and scattered SPP waves:

$$E^{\uparrow}(\vec{x},\omega) = \frac{c}{\omega}[i\hat{x}_1\beta_0(\omega) - \hat{x}_3 k_{\parallel}(\omega)]\exp[ik_{\parallel}(\omega)x_1 - \beta_0(\omega)x_3]$$

$$+ \int \frac{d^2q_{\parallel}}{2\pi}\Big\{\frac{c}{\omega}[i\hat{q}_{\parallel}\beta_0(q_{\parallel}) - \widehat{x_3}q_{\parallel}]A_p(q_{\parallel}) \qquad 4.1$$

$$+ (\widehat{x_3}\times\hat{q}_{\parallel})A_s(q_{\parallel})\Big\}\exp[i\vec{q}_{\parallel}\cdot\vec{x}_{\parallel} - \beta_0(q_{\parallel})x_3]$$

Here, $E^{\uparrow}(\overline{x},\omega)$ is the electric field at the frequency ω, the arrow designates the vacuum region, $k_{\parallel}(\omega)$ and $\beta_0(\omega)$ are the plasmon wave vector and the inverse decay length of the field in the direction normal to the surface, respectively, and are given by the relations:

$$k_{\parallel}(\omega) = \frac{\omega}{c}\sqrt{\frac{\epsilon(\omega)}{\epsilon(\omega)+1}} \qquad 4.2a$$

$$\beta_0(\omega) = \frac{\omega}{c}\sqrt{\frac{-1}{\epsilon(\omega)+1}} \qquad 4.2b$$

These components of the plasmon wave vector satisfy the dispersion relation $k_{\parallel}^2(\omega) - \beta_0^2(\omega) = \omega^2/c^2$, Moreover, the function $\alpha_0(q_{\parallel})$ is defined by

$$\alpha_0(q_{\parallel}) = \begin{cases} \sqrt{q_{\parallel}^2 - \left(\frac{\omega}{c}\right)^2} & q_{\parallel} > \frac{\omega}{c} \\ -i\sqrt{\left(\frac{\omega}{c}\right)^2 - q_{\parallel}^2} & q_{\parallel} < \frac{\omega}{c} \end{cases} \qquad 4.3$$

where the vector $\vec{q}_{\parallel} = (q_1, q_2, 0)$ is parallel to the metal surface. Note that for a surface plasmon $k_{\parallel}(\omega) > \omega/c$, and therefore $\alpha_0\left(k_{\parallel}(\omega)\right) = \beta_0(\omega)$. Finally, $A_s(\vec{q}_{\parallel})$ and $A_p(\vec{q}_{\parallel})$ are scattering amplitudes of the s- and p-polarized waves, respectively. Based on the definition of $\alpha_0(q_{\parallel})$, Eq. (4.3), it can be seen that for $q_{\parallel} > \omega/c$ the scattered waves in Eq.

(4.1) are surface scattered into the vacuum. Note the expansion given in Eq. (4.1) is valid within the Rayleigh hypothesis, namely, close to the surface the series expansion of the electromagnetic field contains only outward propagating waves. In particular, for small surface nanodefects this assumption is rigorously satisfield. [45].

In order to calculate the scattering amplitudes $A_s(\vec{q}_\parallel)$ and $A_p(\vec{q}_\parallel)$, one requires that Eq. (4.1) together with the corresponding equation for the metal region satisfy the boundary conditions at the vacuum/metal interface, a condition that can be cast into a set of coupled reduced Rayleigh equations: [41, 42].

$$f_i(p_\parallel)A_i(p_\parallel) + \sum_{j=p,s} \frac{d^2 q_\parallel}{(2\pi)^2} g_{ij}(p_\parallel, q_\parallel)A_j(q_\parallel) = -g_{ip}(p_\parallel, k_\parallel) \qquad i = p, s \tag{4.4}$$

and the functions $f_{s,p}$ are given by

$$f_p(p_\parallel) = \frac{\epsilon(\omega)\beta_0(p_\parallel) + \beta(p_\parallel)}{1 - \epsilon(\omega)} \tag{4.5a}$$

$$f_s(p_\parallel) = \frac{\beta_0(p_\parallel) + \beta(p_\parallel)}{1 - \epsilon(\omega)} \tag{4.5b}$$

With

$$\alpha(q_\parallel = \sqrt{q_\parallel^2 - \epsilon(\omega)\left(\frac{\omega}{c}\right)^2} \tag{4.6}$$

is the inverse decay length of the electromagnetic field inside the metal and the kernel functions g_{ij} are given by the following expressions:

$$g_{ss}(p_\parallel, q_\parallel) = J(p_\parallel, q_\parallel)\left(\frac{\omega}{c}\right)^2 \vec{p}_\parallel \cdot \vec{q}_\parallel \tag{4.7a}$$

$$g_{pp}(p_\parallel, q_\parallel) = J(p_\parallel, q_\parallel)[p_\parallel q_\parallel - \beta(p_\parallel)\vec{p}_\parallel \cdot \vec{q}_\parallel \beta_0(q_\parallel)] \quad 4.7b$$

$$g_{sp}(p_\parallel, q_\parallel) = iJ(p_\parallel, q_\parallel)\left(\frac{\omega}{c}\right)\beta_0(p_\parallel)(\vec{p}_\parallel \times \vec{q}_\parallel)_3 \quad 4.7c$$

$$g_{ps}(p_\parallel, q_\parallel) = -iJ(p_\parallel, q_\parallel)\left(\frac{\omega}{c}\right)\beta(p_\parallel)(\vec{p}_\parallel \times \vec{q}_\parallel)_3 \quad 4.7d$$

Here, $\vec{p}_\parallel$ and $\vec{q}_\parallel$ are unit vectors and the function $J(p_\parallel, q_\parallel)$ is defined as:

$$J(p_\parallel, q_\parallel) = \int d^2x_\parallel \exp[-i(p_\parallel - q_\parallel) \cdot x_\parallel] \frac{\exp\left[\left(\alpha(p_\parallel) - \alpha_0(q \quad \parallel)\right)\zeta(x_\parallel)\right] - 1}{\alpha(p_\parallel) - \alpha_0(q_\parallel)} \quad 4.8$$

We now introduce the azimuthal angles ϕ_x, ϕ_q, and ϕ_p, which characterize the direction of the vectors $x_\parallel$, $q_\parallel$, and $p_\parallel$, respectively. The scattering amplitudes $A_s(q_\parallel)$ and $A_p(q_\parallel)$ are then expanded in Fourier series,

$$A_j(\vec{q}_\parallel) = \sum_{n=-\infty}^{\infty} A_j^{(n)}(q_\parallel)\exp(in\phi_q), j = s, p \quad 4.9$$

and the Fourier coefficients corresponding to the *p*-polarized waves, $A_p^{(n)}(q_\parallel)$, are rescaled so as to separate their singular behavior at the plasmon wave vector $q_\parallel = k_\parallel$ [the function $f_p(k_\parallel) = 0$ has a simple zero at $q_\parallel = k_\parallel$, $f_p(k_\parallel) = 0$,

$$A_p^n(q_\parallel) = a_p^{(n)}(q_\parallel)/f_p(q_\parallel) \quad 4.10$$

.

Note that since the scattering amplitudes $A_p^{(n)}(q_\parallel)$ have a simple pole at $q_\parallel = k_\parallel$, the reduced scattering amplitudes $a_p^{(n)}(q_\parallel)$ are bounded functions. Finally, by substituting Eqs.

(4.9) - (4.10) into the relations (4.4) one obtains the following set of coupled integral equations:

$$a_p^n(p_\parallel) + \frac{1}{2\pi}\int_0^\infty dq_\parallel q_\parallel \left[\frac{h_{pp}^n(p_\parallel, q_\parallel)}{f_p(q_\parallel)} a_p^n(q_\parallel) + h_{ps}^n(p_\parallel, q_\parallel) A_s^n(q_\parallel)\right] = -h_{pp}^n(p_\parallel, k_\parallel) \quad \text{4.11a}$$

$$f_s(p_\parallel) A_s^n(p_\parallel) + \frac{1}{2\pi}\int_0^\infty dq_\parallel q_\parallel \left[\frac{h_{sp}^n(p_\parallel, q_\parallel)}{f_p(q_\parallel)} a_p^n(q_\parallel) + h_{ss}^n(p_\parallel, q_\parallel) A_s^n(q_\parallel)\right] = -h_{sp}^n(p_\parallel, k_\parallel) \quad \text{4.11b}$$

Where

$$h_{ss}^{n}(p_{\parallel},q_{\parallel})=\frac{1}{2}\left(\frac{\omega}{c}\right)^{2}[N_{n-1}+N_{n+1}] \quad 4.12a$$

$$h_{pp}^{n}(p_{\parallel},q_{\parallel})=N_{n}p_{\parallel}q_{\parallel}-\frac{1}{2}\alpha(p_{\parallel})\alpha_{0}(q_{\parallel})[N_{n-1}+N_{n+1}] \quad 4.12b$$

$$h_{sp}^{n}(p_{\parallel},q_{\parallel})=-\frac{1}{2}\frac{\omega}{c}\alpha_{0}(q_{\parallel})[N_{n-1}-N_{n+1}] \quad 4.12c$$

$$h_{ps}^{n}(p_{\parallel},q_{\parallel})=\frac{1}{2}\frac{\omega}{c}\alpha(q_{\parallel})[N_{n-1}-N_{n+1}] \quad 4.12d$$

And

$$N_{m}=\frac{2\pi}{\beta(p_{\parallel})-\beta_{0}(q_{\parallel})}\int_{0}^{\infty}x_{\parallel}dx_{\parallel}\left\{\exp\left[\left(\beta(p_{\parallel})-\beta_{0}(q_{\parallel})\right)\zeta(x_{\parallel})\right]-1\right\}J_{m}(p_{\parallel}x_{\parallel})J_{m}(q_{\parallel}x_{\parallel}) \quad 4.13$$

Equations [4.11] are solved numerically for the scattering amplitude coefficients $a_{p}^{(n)}(q_{\parallel})$ and $A_{s}^{(n)}(q_{\parallel})$, and subsequently, by using the Fourier expansions in Eq. [4.9] the scattering amplitudes $A_{s,p}(p_{\parallel})$are determined. These scattering amplitudes fully determine the distribution of the electric field in the spatial region $x_{3}\geq\zeta(x_{\parallel})$, at the FF, as shown by the Eq. (4.1).

4.2.2 Light scattering at second harmonic

The complete description of the spatial distribution of the electromagnetic field at the FF allows one to determine the field distribution at the SH. Thus, according to the phenomenological model that is used to describe the physical properties of the SHG at the interface between two centrosymmetric media, the generated SH has two sources, namely a

surface nonlinear polarization localized within a thin surface layer at the interface between the two media and a non-local polarization originating from bulk magnetic dipoles and electric quadrupoles. Although the two media are centrosymmetric, and thus electric-dipole transitions are not allowed, the inversion symmetry is broken in the thin layer at the interface between the two media and therefore the sheet of nonlinear surface polarization at the SH, $P_s^{(2\omega)}(r)$, is induced at this interface. This nonlinear polarization is related to the electric field at the FF by a second-order nonlinear susceptibility tensor,

$$P_s^{(2\omega)}(r) = \chi_s^{(2)} : E^{(\omega)} E^{(\omega)} \delta\big(x_3 - \zeta(x_1, x_2)\big) \tag{4.14}$$

where $\chi_s^{(2)}$ is the surface second-order susceptibility and the Dirac function describes the surface characteristic of the source polarization.

In the case of homogeneous isotropic media excited by plane waves the bulk nonlocal nonlinear polarization can be expressed as [45,46] $P_{bulk}^{(2\omega)}(r) = \gamma \nabla [E^{(\omega)}(r) \cdot E^{(\omega)}(r)]$, where $\gamma = e[1 - \epsilon(\omega)]/32\pi m\omega^2$ and e and m are the charge and mass of the electron, respectively. As has been demonstrated, [47] the longitudinal nature of this nonlinear polarization makes it that its contribution to the SHG is indistinguishable from that of the surface nonlinear polarization given in Eq. (1.14). In practice, this contribution is accounted for by rescaling the components of the surface susceptibility $\chi_s^{(2)}$ so as to include the contributions of both the surface and bulk polarizations. Nevertheless, in the case of metals these two nonlinear polarization sources have largely different relative contributions to the SHG process, especially if ω is close to the frequency of resonantly excited SPPs. Thus at this frequency, the contribution of the surface nonlinear polarization to the SHG is enhanced significantly more than that of the bulk source, [48] and therefore the bulk contribution can be neglected. Indeed, recent experiments have demonstrated that

in the case of metals with good, i.e. low-loss, optical properties (Ag, Au) the surface nonlinear susceptibility is about two orders of magnitude larger than the bulk one. [49].

In most cases of practical interest, the metal/vacuum interfaces possess an isotropic mirror-symmetry plane perpendicular to the interface. Under these circumstances, the surface nonlinear susceptibility $\chi_s^{(2)}$ has only three independent components, which are $\chi_{s,\perp\perp\perp}^{(2)}$, and $\chi_{s,\perp\parallel\parallel}^{(2)}$ and $\chi_{s,\parallel\perp\parallel}^{(2)} = \chi_{s,\parallel\parallel\perp}^{(2)}$, where $\perp \; and \; \parallel$ refer to normal and perpendicular directions to the surface, respectively. In our calculations, we assume the following values for the independent components of the susceptibility tensor $\chi_s^{(2)}$, $\chi_{s,\perp\perp\perp}^{(2)} = 5.02 \times 10^{-18} m^2/V$, $\chi_{s,\perp\parallel\parallel}^{(2)} = -2.54 \times 10^{-21} m^2/V$, $\chi_{s,\parallel\perp\parallel}^{(2)} = \chi_{s,\parallel\parallel\perp}^{(2)} = 1.13 \times 10^{-20} m^2/V$. [50]. However, it should be noted that in certain cases the metal/vacuum interface lacks a mirror symmetry plane, namely when chiral molecules are adsorbed at the interface or in the case of nanopatterned metallic surfaces.

Since the source of the electromagnetic field at the SH is the surface nonlinear polarization $P_s^{(2\omega)}(r)$, we can fully characterize the SHG process once we know multipole moments associated with this nonlinear polarization. As the nanodefect characteristic size a of the nanodefect is considerably smaller than the plasmon wavelengths, $k(\omega)a \ll 1$, we have restricted our calculations to multipoles up to the second order, that is, the electric dipole moment, the magnetic dipole moment, and the electric quadrupole moment; they are defined by the following relations: [50],

$$p = \int P^{(2\omega)}(r')dr' \tag{4.15a}$$

$$m = -\frac{i\omega}{2}\int r' \times P^{(2\omega)}(r')dr' \tag{4.15b}$$

$$Q(n) = \int \left\{ 3\left[\left(\widehat{r}\cdot r'\right)P^{(2\omega)}(r') + \left(\widehat{r}\cdot P^{(2\omega)}(r')\right)r'\right] - 2[(r'\cdot P^{(2\omega)}(r))\hat{r}]\right\} dr' \quad \text{4.15c}$$

Since we are only interested in the SH generated by the nanodefect, the integration region in Eqs. [4.15] for a Gaussian defect is chosen to be L = 3.5R, as illustrated in Fig 4.1. For the case of spherical cap and cylinder, the domains of integration are chosen to be $\zeta(x_{\parallel}) \neq 0$, that is, $L = 2\rho$ for the spherical cap and $L = 2R$ for the cylinder. It should be noted that in our study we do not consider the SHG from the entire flat surface, which has been extensively studied, because it provides only a uniform background illumination. [32].

The angular distribution for the radiated power at the SH, originating from the multipoles described by Eqs. [4.15], is given by the following equations, [52]:

$$\frac{dP_{ed}}{d\theta} = \frac{Z_0 c^2 K^4}{32\pi}\left|(n\times p)\times n\right|^2 \quad \text{4.16a}$$

$$\frac{dP_{md}}{d\theta} = \frac{Z_0 K^4}{32\pi}\left|(n\times m)\times n\right|^2 \quad \text{4.16b}$$

$$\frac{dP_{eq}}{d\theta} = \frac{Z_0 c^2 K^5}{1152\pi}\left|\left(n\times Q(n)\right)\times n\right|^2 \quad \text{4.16c}$$

Where P_{ed}, P_{md}, P_{eq} correspond to the power radiated by the electric dipole, magnetic dipole, and electric quadrupole, respectively. $K = 2\omega/C$ is the wave vector at the second harmonic and $Z_0 = \sqrt{\mu_0/\epsilon_0}$ is the vacuum impedance. As is well known from classical electrodynamics, at longer wavelengths the main contribution to the emitted energy comes from the electric-dipole moment ($P_{ed}\sim\lambda^{-4}$) whereas at smaller wavelengths the radiated energy comes primarily from the magnetic and quadrupole moments ($P_{md}, P_{eq}\sim\lambda^{-6}$).

Finally, calculating these multipoles allow us to determine not only the radiative field at the SH but also the near-field; the corresponding near-field formulae are not presented here as their expressions are rather long and cumbersome.

4.2.3 Numerical approach

To solve Eqs. [4.11] numerically, we follow a procedure described in Ref. [31]. Thus, this system of coupled equations is discretized on a uniform computational grid that spans the domain $q_{\parallel}, p_{\parallel} \in (0, \Lambda_{max})$, the step size of the computational grid being $\Delta q_{\parallel}$. To reach convergence of the numerical results, ~1500 grid points are necessary, whereas the upper limit of the wave vectors $p_{\parallel}$ and $q_{\parallel}$, Λ_{max}, is chosen to be in the range of 20/R~70/R. In addition, the computational grid is constructed in such a way that the point $k_{\parallel}$ is one of the grid points.

In the discretization process, the integrals in Eqs. [4.11] are calculated as a sum of integrals defined over the intervals between adjacent grid points, each of these integrals being then approximated as the product between the integrand evaluated at the midpoint of the interval and the size of the interval, $\Delta q_{\parallel}$. As previously explained, the integral equations [4.11] have a singularity (a simple pole) at $q_{\parallel} = k_{\parallel}$. This singular point is treated separately, and the corresponding integral is being calculated analytically. As a result of this discretization procedure, Eqs. [4.11] are cast into two linear coupled matrix equations, which are solved by using standard numerical techniques. The corresponding discretized equations can be written in the following form:

$$a_p^n(p_j) + \frac{1}{2\pi}\sum_i \Delta q q_i \left[\frac{h_{pp}^n(p_j, q_i)}{f_p(q_i)} a_p^n(q_i) + h_{ps}^n(p_j, q_i) A_s^n(q_i)\right] = -h_{pp}^n(p_j, k_\parallel) \quad 4.17a$$

$$f_s(p_j) A_s^n(p_j) + \frac{1}{2\pi}\sum_i \Delta q q_i \left[\frac{h_{sp}^n(p_j, q_i)}{f_p(q_i)} a_p^n(q_i) + h_{ss}^n(p_j, q_i) A_s^n(q_i)\right] = -h_{sp}^n(p_j, k_\parallel) \quad 4.18b$$

where *i* and *j* indexes the grid points. Furthermore, in the case of a Gaussian-shaped defect, the integrals $N_m$defined by Eq. [4.13] can be expressed as a series of Bessel functions of the second kind, I_m,

$$N_m = \pi A R^2 \sum_{n=1}^{\infty} \frac{\{[\beta(p_\parallel) - \beta_0(q_\parallel)]A\}^{n-1}}{n.n!} \exp\left[-\frac{(p_\parallel^2 + q_\parallel^2)R^2}{4n}\right] I_m\left(\frac{p_\parallel q_\parallel R^2}{2n}\right) \quad 4.19$$

For the hemisphere- and cylinder-shaped defects the integral that defines the functions $N_m(q_\parallel, p_\parallel)$ are calculated numerically, by using an adaptive integration algorithm. [53]. Moreover, in the case of cylindrical nanodefects, in order to resolve the strongly inhomogeneous electromagnetic field near the sharp corners, a considerably large number of grid point must be used, with the result of a slow convergence rate of the numerical algorithm. In order to overcome this problem, a numerical procedure was employed that in effect smoothes out the top edge of the cylinder, namely, the shape function $\zeta(x_\parallel)$ was

multiplied by the function shape factor $1 - 1/\cosh[p_1(p_2 R - x_{\parallel})]$, with $p_1 = 0.6 \times 10^8$ and $p_2 = 1.12$.

Finally, once the complete distribution of the electromagnetic field at the FF is determined through the method just described, the scattering process at the SH is numerically characterized as follows. First the surface nonlinear polarization $P_s^{(2\omega)}(r)$ is calculated using Eq. [4.14] and subsequently the multipoles are determined from Eqs. [4.15]. The spatial distribution of the electromagnetic field at the SH and the corresponding emitted power are then calculated by using Eqs. [4.16].

4.3 RESULTS AND DISCUSSIONS

In this section we present and discuss the main results pertaining to the spatial distribution of near- and far-field, as well as the spatial pattern of the scattered light, both at the FF and the SH.

4.3.1 Field distribution and scattered light: fundamental frequency

The theoretical formalism presented in subsection 4.2.1 provides a full description of the distribution of the electromagnetic field, both in the close proximity of the defect (the near-field), as well as far from the scatterer (the far-field). A generic example of the spatial distribution of the field amplitude at the FF, $|E^{\uparrow}(r;\, \omega)|$, corresponding to a Gaussian indentation, is presented in Fig. 2. Among other things, this figure clearly shows the transition between the near-field, seen as a series of ripples that are formed through the interference between the incident plasmon field and the scattered field, and the far-field, which is seen as an emerging beam of scattered light (a nanoflashlight) emitted by the

defect. The angle of this flashlight "beam" with respect to the surface normal is a result of momentum matching between the SPP and scattered light momenta and a characteristic reciprocal vector of the scatterer, i.e. π/R, much as is the case of plasmon scattering from a surface diffraction grating. [30]. Note that the width of the emitted beam, measured in a transverse plane located at $1.5\,\mu m$ above the metallic surface, is only a few hundreds nanometers. Hence the plasmon scattering by metallic nanodefects could provide an interesting and flexible approach to generate and manipulate sub-wavelength optical beams, an idea discussed in Ref. [31].

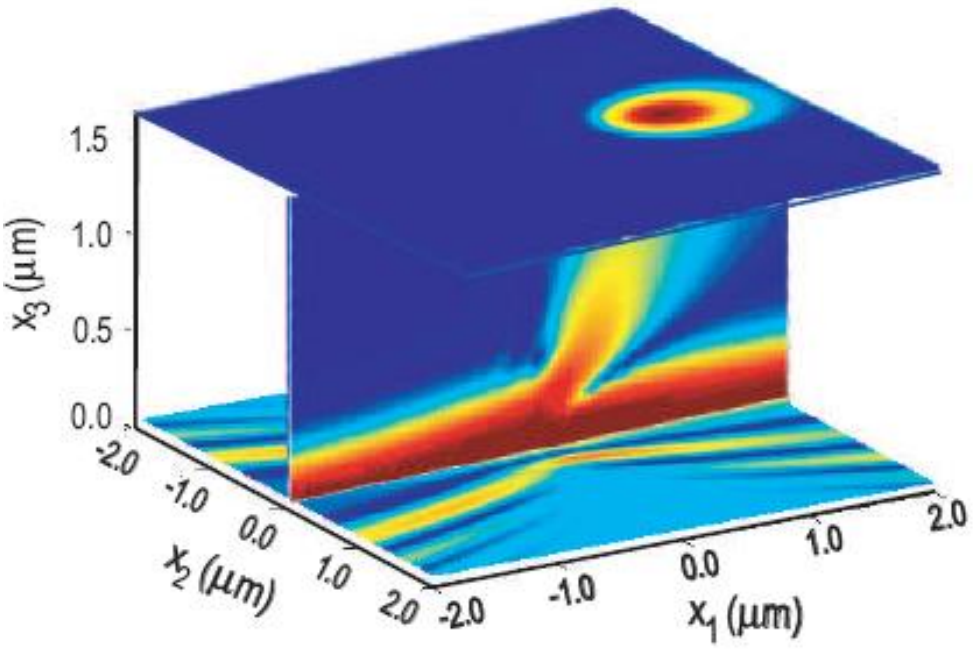

FIG. 4.2: Electric field distribution corresponding to the scattering of a SPP off a Gaussian nanodefect with $R = 200\,nm$ and $h = -50\,nm$ where only the scattered light is shown. The wavelength of the incident SPP is $\lambda = 328\,nm$.

As an interesting aside, the property that the shape of the defects considered here is invariant to rotation transformations implies that the scattering coefficients $A_{p,s}^{(n)}(q_{\parallel})$ defined by Eq. [4.9] obey the symmetry relation $|A_{p,s}^{(n)}(q_{\parallel})| = |A_{p,s}^{(-n)}(q_{\parallel})|$ and therefore the total angular momentum of the scattered electromagnetic field is zero. However, it can be easily seen that in the case of chiral scatterers the just mention symmetry relation no longer holds, and thus the scattered field, in particular the nanoflashlight seen in Fig. 4.2, will have a finite angular momentum. One immediate consequence of this effect is that the scattering of SPPs from chiral defects can be readily used to generate sub-wavelength optical beams carrying angular momentum, namely, optical nanotweezers.

Deeper insight into the characteristics of the plasmon scattering at the FF is provided by the frequency dependence of the total scattering cross sections of SPPs and light. Thus, using the relations (A.4) and (A.5) in the Appendix, we have calculated the spectra of these scattering cross sections, both for indentations and protuberances. Note that the scattering cross section corresponding to the emitted radiation contains the contribution of both the *s*- and *p*-polarized waves. The results of these calculations, summarized in Fig. 4.3, lead us to several important conclusions. But before discussing the results note that the general shape and appearance of these two scattering cross sections is similar to that presented earlier by the Maradudin Group [31], [43], although the greater computation resources available at present allows a fuller spectral range to be examined. First, both spectra show a resonant behavior, in both cases the scattering process being most efficient at a certain resonant frequency. The two resonant frequencies are very different from each other, and thus one can infer that the two scattering processes are only weakly coupled. More specifically, whereas the generation of radiative modes can be viewed as the result of

the creation of spatial inhomogeneities in the incoming field, at the location of the defect, the scattered surface plasmons are generated via the excitation of localized plasmon modes supported by the surface defect. This dichotomy in the scattering process also explains the markedly different width of the SPP and light spectra of the corresponding cross-sections. In addition, a comparison of the peak scattering cross sections suggests that the scattering of the incident SPP into SPP waves is a much more efficient process as compared to the scattering of the incident SPP into radiation, the corresponding ratio of the cross sections being ~5. This result is explained by the fact that, due to their similar characteristics, the overlap between the electromagnetic field of the incident and scattered SPP waves is larger than the overlap between the fields of the incident SPP wave and the emitted radiation.

Figure 4.3 also shows that surface indentations are more effective in scattering the incident SPP, as compared with protuberances, a result that can be attributed to the cavity effect associated with such surface defects. Moreover, the spectra of the scattering cross sections of both SPPs and light show a steep decrease near $\omega/\omega_p \sim 0.7$, which is due to the fact that surface SPP waves at the metal/vacuum interface can not exist if $\omega > \omega_p/\sqrt{2}$.

We have also investigated the dependence of the scattering cross sections on the size of the surface defect. The results corresponding to the scattering cross section of light are summarized in Fig. 4.4(a). Thus one can observe that in the case of shallow surface defects the amount of radiated light decreases as the radius of the defect increases, which suggests that in the case of larger defects the field can easier readjust to the shape of the defect and thus it is perturbed to a smaller extent. However, if one compares the amount of light scattered by defects with the same radius R but different depth h one observe that more light is emitted by defects with larger depth. Again, this result is explained by the fact

that the larger the depth of a surface defect, the stronger the perturbation of the incident plasmon field; although not shown, this same behavior follows when varying the height of protuberance.

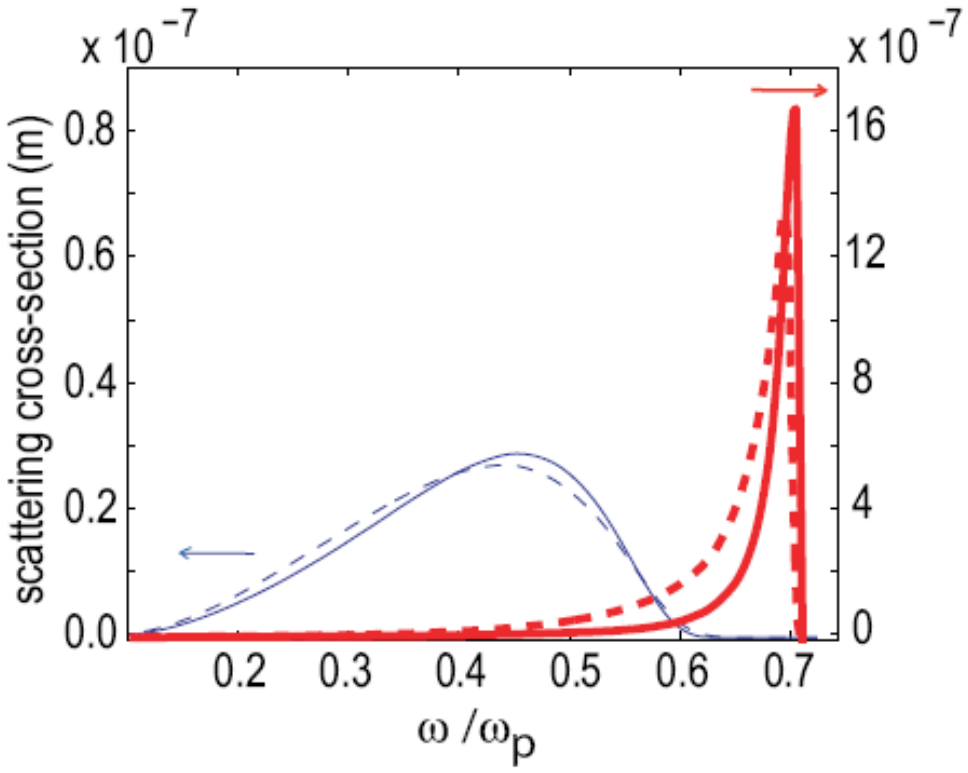

FIG. 4.3: Total scattering cross section of light and SPP, for both indentation ($h < 0$, solid line) and protuberance ($h > 0$, dash line). The defect parameters are $|h| = 50\,nm$ and $R = 200\,nm$. Red and blue curves correspond to the scattering cross section of SPPs and light, respectively.

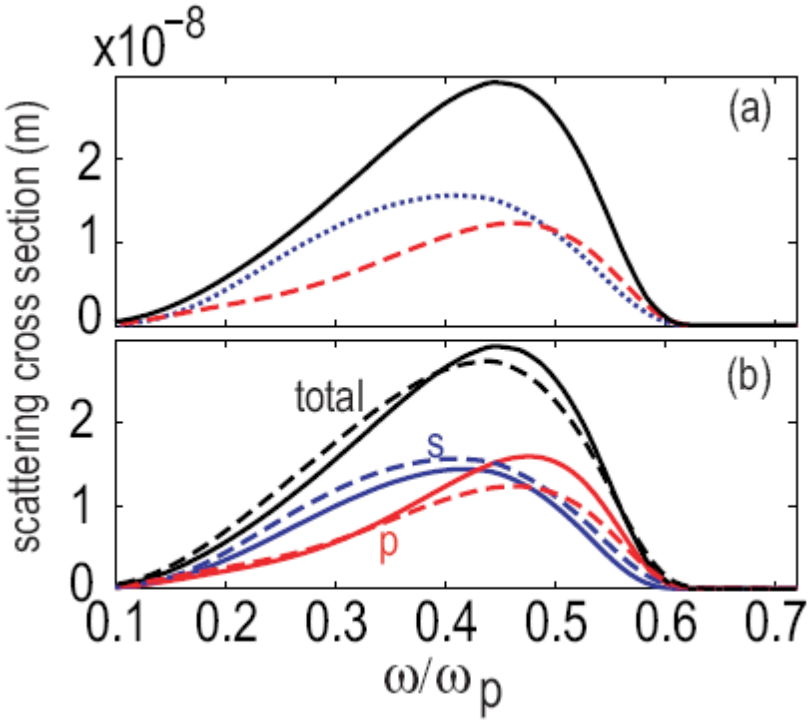

FIG. 4.4: Dependence of the scattering cross section of light on the size of the Gaussian defect and polarization of the scattered light. The curves in the panel (a) correspond to R = 200 nm and h = −50 nm (solid curve), R = 200 nm and h = −20 nm (dash curve), R = 150 nm and h = −20 nm (dotted curve). Panel (b) shows the spectra of the scattering cross sections corresponding to R = 200 nm and |h| = 50 nm: the solid (dash) curves correspond to h < 0 (h > 0). As indicated, the black curves correspond to the total scattering cross section whereas the blue and red curves correspond to the s- and p-polarized light, respectively.

As we have discussed, unlike the 1D case, in the case of 2D surface defects the emitted light can not only be p-polarized but also s-polarized. The spectra of the total scattering cross section as well as the corresponding spectra of the s- and p-polarized light

are shown in Fig. 4.4(b). Thus, it can be seen from this figure that the spectra corresponding to the two polarizations show a similar resonant behavior; however, the two resonant frequencies have slightly different values. In addition, our calculations show that at low frequency (long wavelength side of the spectra) the radiated light is predominantly s-polarized whereas the light emitted at high frequencies (at the blue side of the spectrum) is predominantly p-polarized.

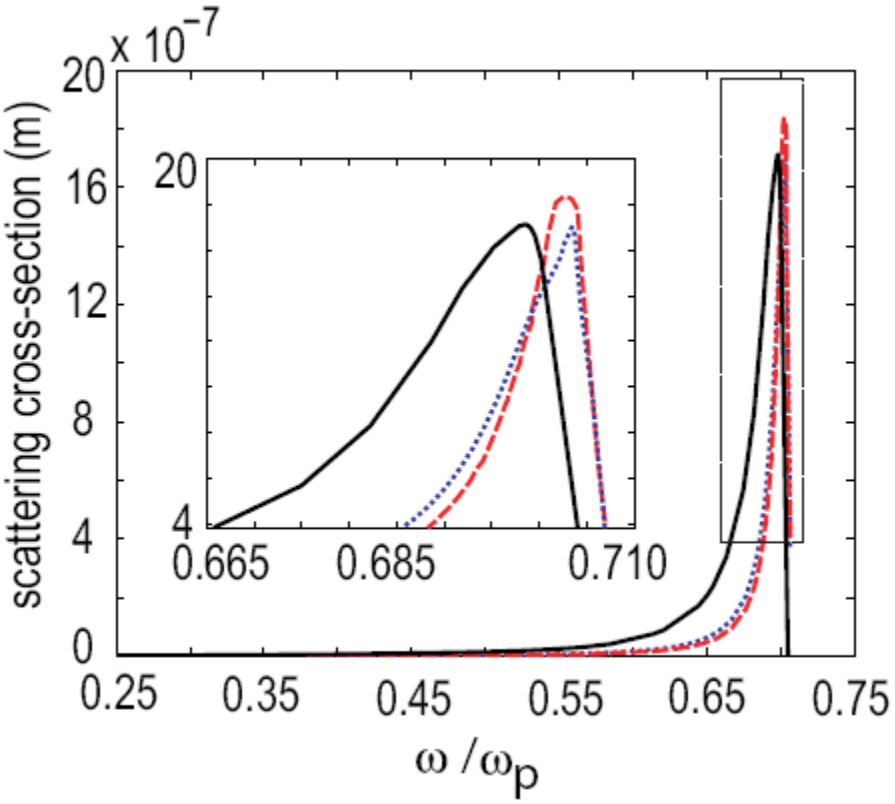

FIG. 4.5: Dependence of the scattering cross section of SPPs on the size of the Gaussian defect. The curves correspond to R = 200 nm and h = −50 nm (solid curve), R = 200 nm and h = −20 nm (dash curve), R = 150 nm and h = −20 nm (dotted curve).

Similar studies have been done of the dependence of the peak SPP scattering cross sectionnand the width of its spectrum on the width and depth/height of the defect. The main results, plotted in Fig. 4.5, support the general conclusion according to which the incident SPP wave generates SPP modes localized at the site of the defect, which subsequently decay into outgoing SPP waves. Thus, Fig. 4.5 shows that the width of the spectrum of the scattering cross section decreases with the depth of the defect. As expected, deeper defects are more effective in capturing and thus re-emitting the incident SPP wave, an effect that leads to the broadening of the SPP scattering cross section spectra with the width of the defect. On the other hand, the scattering cross section depends only slightly on the radius of the defect.

A better understanding of scattering of the incident SPP, at the FF, can be achieved by analyzing the distribution of the electromagnetic field in the proximity of the surface defect. In this connection, Fig. 4.6 shows the field distribution in two horizontal sections, one at a distance that is only a fraction of the wavelength of the plasmon and the other one located a few wavelengths away from the metallic surface. Note that the plots in Fig. 4.6 do not contain the field of the incident SPP wave. This figure clearly illustrates the transition from the near-field to far-field as well as the strong dependence of the electromagnetic field on the polarization of the emitted field. Thus, as expected, in the case of the *s*-polarized light, the field is predominantly located at the position of the surface defect. This behavior is a direct consequence of the fact that the SPP waves are p-polarized, and thus the s-polarized field cannot propagate along the vacuum/metal interface. Moreover, Fig. 4.6 shows that in the case of the s-polarized scattered light the electric field vanishes in the plane $x_2 = 0$. To understand this property, note that the electric field of the s-polarized

scattered light, at the plane $x_2 = 0$, is perpendicular on this plane and thus symmetry considerations require that it vanishes within this plane. In addition the electric field for p-polarized light has a large value even a few wavelengths away from the surface defect. This electric field is radiated by the outgoing surface SPP waves that are generated in the scattering process. Also, note that the spatial distribution of the total field is similar to that of the p-polarized light, which suggests that, at this wavelength, the radiated light in the nanobeam directed in the $x_2 = 0$ plane is predominantly p-polarized. S-polarized light is emitted at two angles with respect to this plane and is thus more diffuse in the $x_3 = 1.2\ \mu m$ plane shown here.

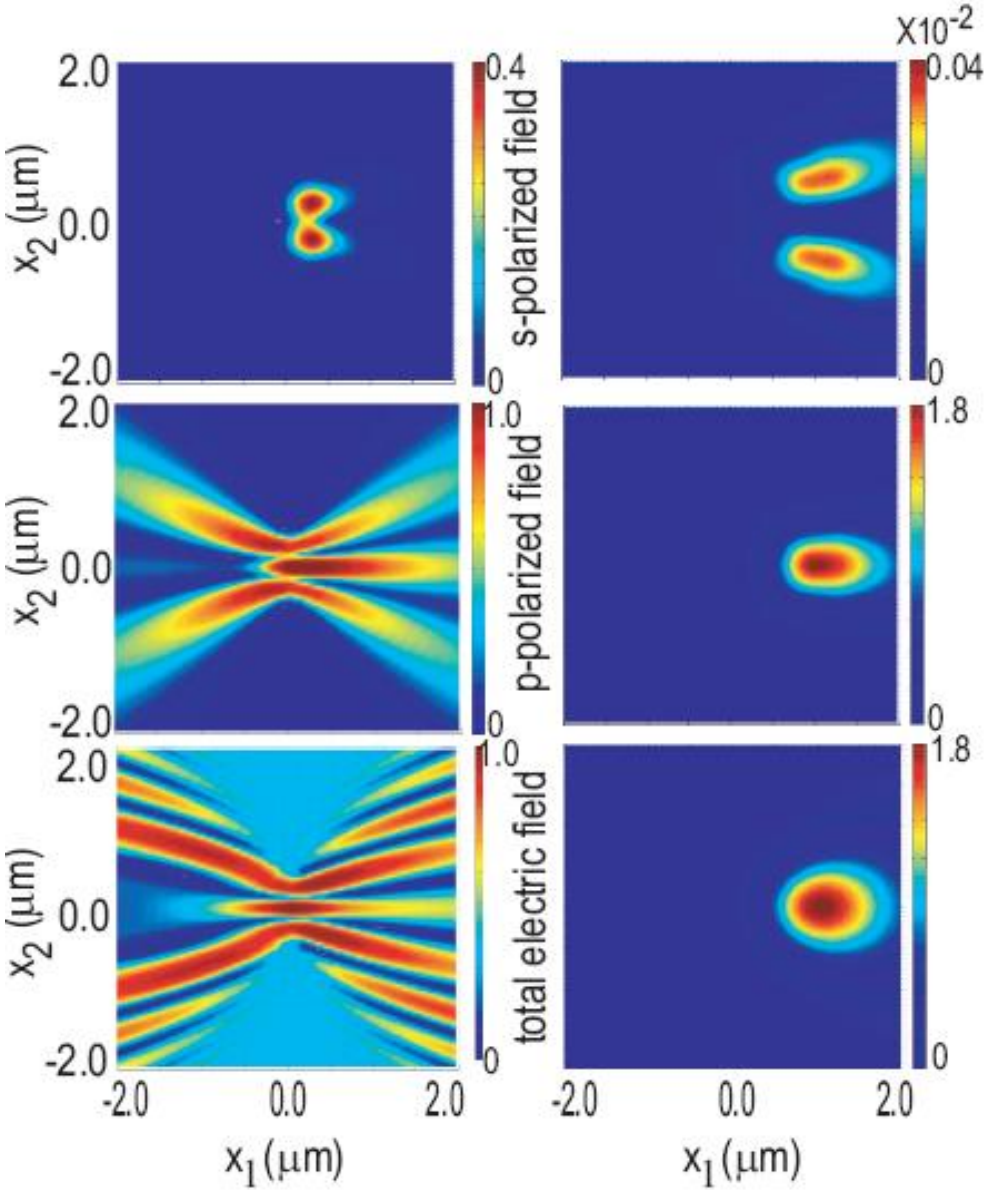

FIG. 4.6: Near- to far-field transition corresponding to a Gaussian surface defect with R = 200 nm and h = −50 nm. The incident SPP wavelength is $\lambda = 328\,nm$. The panels on the left and on the right correspond to horizontal plane sections at $x_3 = 0.2\,\mu m$ and $x_3 = 1.2\,\mu m$, respectively.

We have also investigated the dependence of the SPP-surface defect scattering process on the specific shape of the defect. In particular, we have considered Gaussian, cylindrical and hemispherical defects. The main results of this analysis are presented in Fig. 4.7, which shows the frequency dependence of the scattered light corresponding to these three shapes of the surface defect. As expected, the scattering cross sections of light emitted by Gaussian and hemispherical defects have similar spectral characteristics, namely, a broad spectrum with a maximum at a certain resonant frequency.

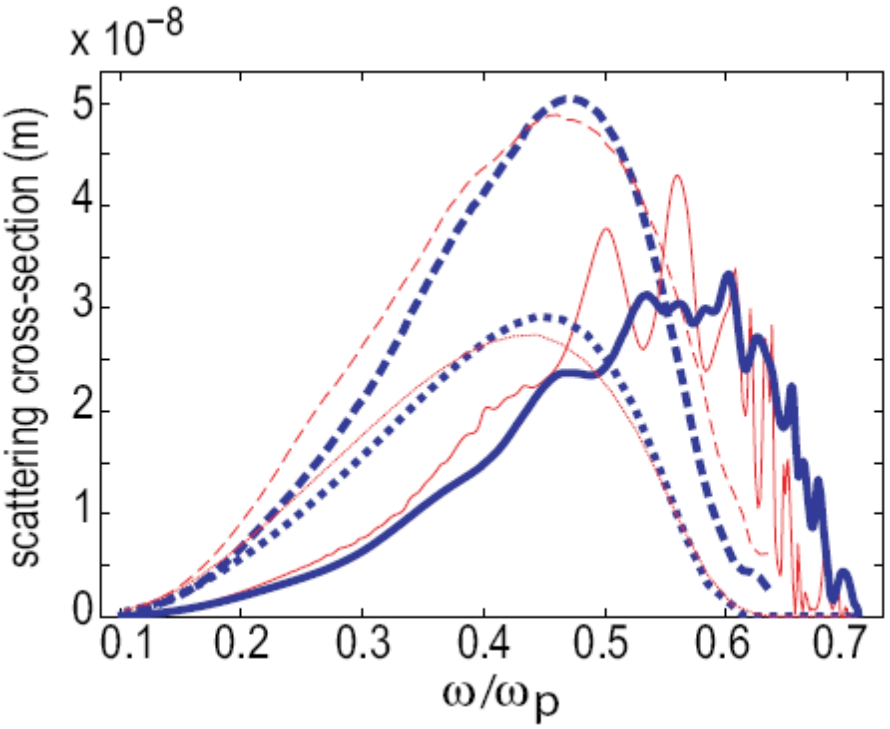

FIG. 4.7: Scattering cross sections corresponding to cylindrical ($R = 200\,nm$ and $|h| = 20\,nm$, solid curves), hemispherical ($R = 600\,nm$ and $|h| = 50\,nm$, dash curves), and Gaussian ($R = 200\,nm$ and $|h| = 20\,nm$, dotted curves) surface defects. The thick and thin curves correspond to $h < 0$ and $h > 0$, respectively.

Unlike the case of these two types of surface defects, the spectra corresponding to cylindrical defects, i.e. cylindrical holes or pillars, present a series of sharp, well defined maxima which become more closely spaced as the frequency approaches the asymptotic limit $\omega = \omega_p/\sqrt{2}$. These spectral peaks can be associated with the excitation of plasmon modes with a vanishing longitudinal (along the x_3 axis of the cylinder) propagation constant, at the surface of the cylindrical defects. Indeed, the propagation constant of the incident surface plasmon lies in the surface plane, and therefore any modes excited in the x_3 plane for a cylindrical defect must have a vanishing longitudinal propagation constant. As it is well known, [54,55], these modes form a sharp, discrete spectrum with the mode frequency asymptotically approaching the limit frequency of $\frac{\omega_p}{\sqrt{2}}$, irrespective of the radius of the cylinder.

Our calculations show not only that the spectra of the scattering cross sections depend on the particular shape of the defect but also that the field distribution is strongly dependent on the geometry of the defect. This property, which can have a series of applications to near field optical microscopy, is illustrated by the results summarized in Fig. 4.8. This figure clearly shows that both the near field and the far-field generated in the scattering process, at the FF, are strongly dependent on the shape of the defect. For example, it can be seen that, unlike the case of a Gaussian or hemispherical defect, two nano-beams are emitted in the case of a cylindrical defect.

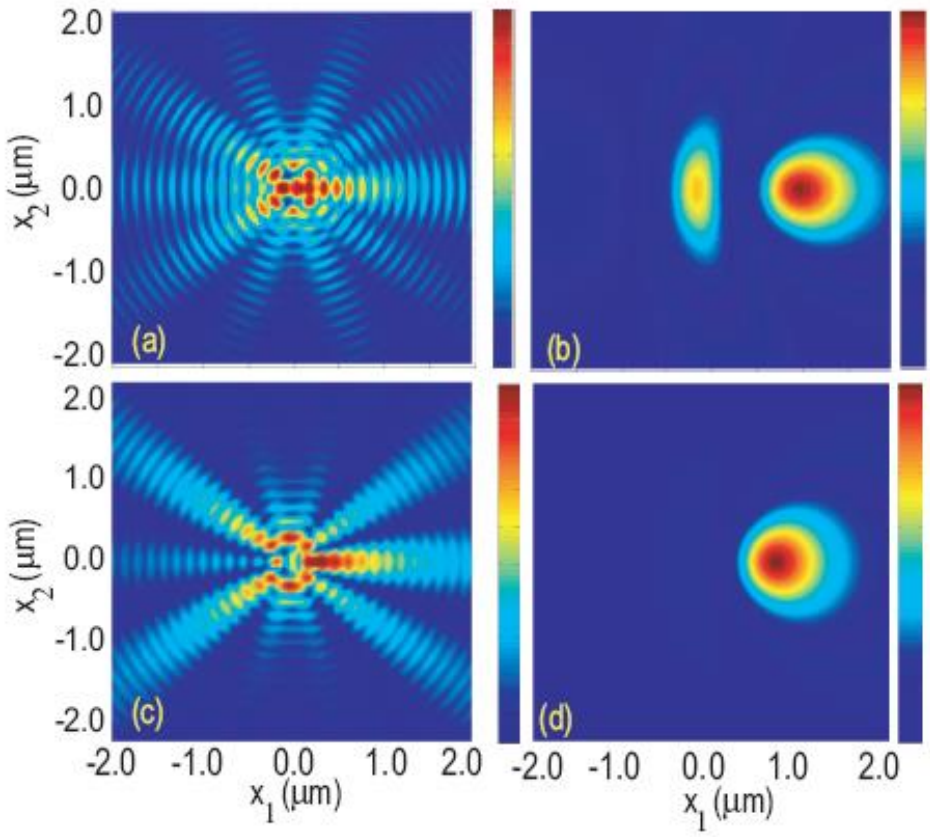

FIG. 4.8: Near-field and far-field distribution corresponding to cylindrical ($R = 200\,nm$ and $h = -20\,nm$, top panels) and hemispherical ($R = 600\,nm$ and $h = -50\,nm$, bottom panels) surface defects. The panels on the left and on the right correspond to horizontal plane sections at $x_3 = 0.2\,\mu m$ and $x_3 = 1.2\,\mu m$, respectively. The incident SPP wavelength is $\lambda = 328\,nm$.

4.3.2 Field distribution and scattered light: second harmonic

The theoretical formalism presented in Sec. 4.2.2 allows one to determine the spatial distribution of the electric field at the SH and the corresponding scattering cross

section, once the electric field at the FF has been calculated. In addition, our theoretical model allows us to study the relative contribution of the multipole moments to the total amount of light generated at the SH.

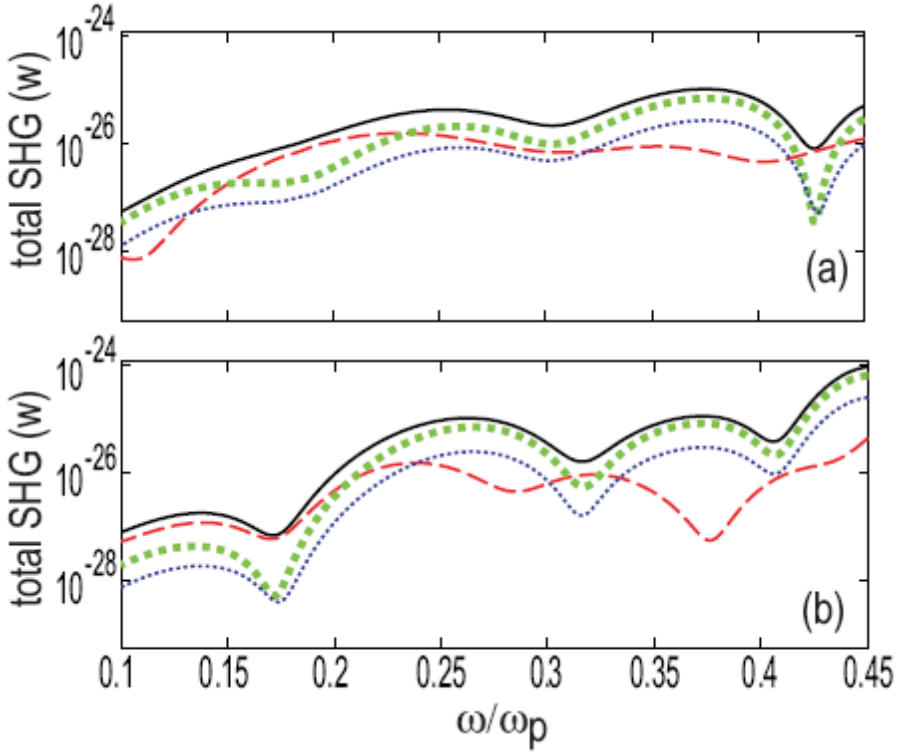

FIG. 4.9: Spectra of the SH radiated upon the scattering of SPP waves off Gaussian surface defects. Panels (a) and (b) correspond to indentations (h = −50 nm) and protuberances (h = 50 nm), respectively. In both panels, R = 200 nm and the spectra in both panels correspond to the electric dipole moment (thin dash curves), the magnetic dipole moment (thick dotted curves), the electric quadrupole moment (thin dotted curves), and the total SHG (thin solid curves).

A generic example that illustrates how our theoretical model can be applied to study the generation of SH via the scattering of SPP waves by surface defects is presented in Fig. 4.9. Thus, this figure shows the spectra of the radiated SH, the surface defects considered being Gaussian-shaped indentations and protuberances. Our theoretical formalism allows us to separate the contribution of each multipole moment to the total generated SHG, so that we show in Fig. 4.9 the spectrum of each of all these moments (up to the second-order). As expected, our calculations show that the SH generated at short wavelengths is predominantly due to the higher-order multipole moments (magnetic dipole and electric quadrupole), whereas at long wavelengths (low frequency) the SH is primarily generated by the induced electric dipoles. In addition, it can be seen that the frequencies of the maxima and minima in the spectra corresponding to the magnetic dipole and electric quadrupole are the same; in fact overall, these spectra exhibit nearly identical spectral variation. However, the spectrum corresponding to the electric dipole shows a quite different frequency dependence, a fact that is explained by the particular dependence on wavelength of the power radiated by the induced multipole moments [see Eq. (4.16)]. Note also that the total amount of generated SH increases with the frequency of the incident SPP wave. Indeed, as the frequency increases the incident SPP wave has a shorter wavelength and thus interacts more strongly with the surface defect. Consequently, the induced multipole moments have a larger magnitude. Importantly, the spectral characteristics of the radiated power at the FF are significantly different from those corresponding to the SH, which further illustrates the differences in the physical phenomena involved in the radiation process at the two frequencies.

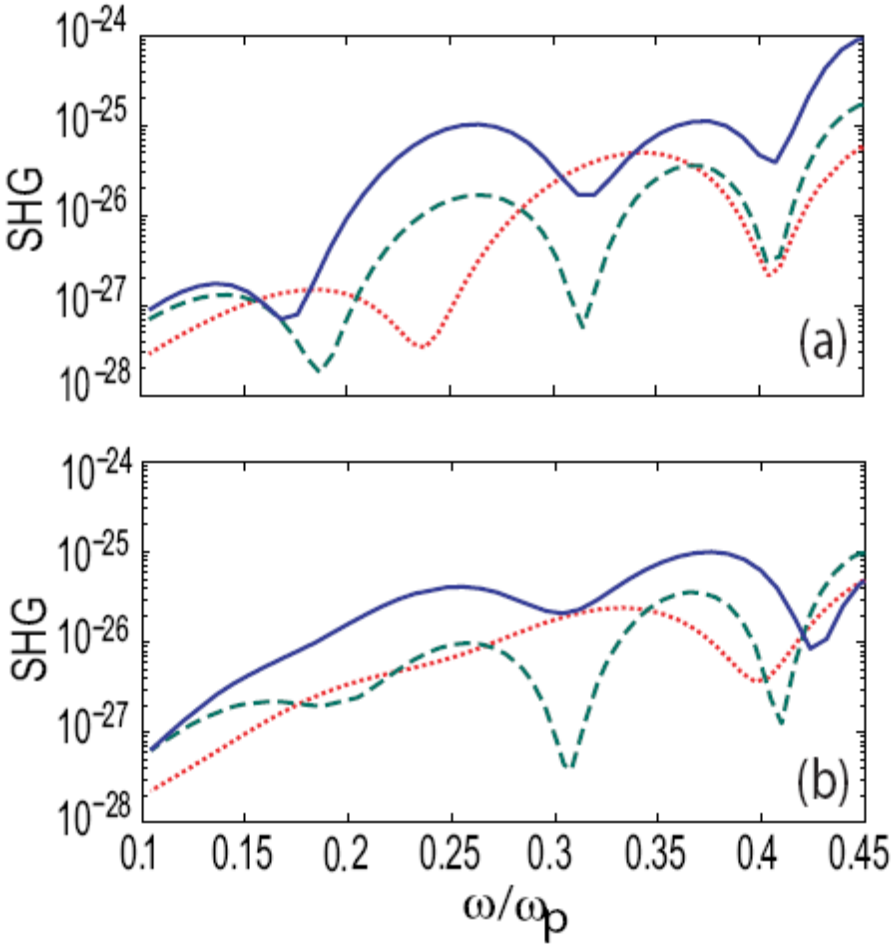

FIG. 4.10: Dependence of the total SHG on the size of Gaussian surface defects. Panels (a) and (b) correspond to protuberances (h > 0) and indentations (h < 0), respectively. In both panels, the parameters of the defect are: R = 200 nm and |h| = 50 nm (solid curves), R = 200 nm and |h| = 20 nm (dash curves), and R = 150 nm and |h| = 20 nm (dotted curves).

We have also investigated the dependence of the spectra of the generated SH on the geometrical parameters of the surface defect. The results corresponding to a Gaussian surface defect are summarized in Fig. 10. This figure shows that larger defects lead to the generation of a larger SH signal. This result is an expected dependence of the SHG on the

size of the defect since in the case of larger defects the nonlinear surface polarization is induced over a larger area and therefore the multipole moments that generate light at the SH are larger. Also, Fig. 4.10 suggests that the frequencies at which the SH spectra have minima are primarily determined by the radius of the defect, the height (depth) h having only a marginal influence on the location of these frequencies.

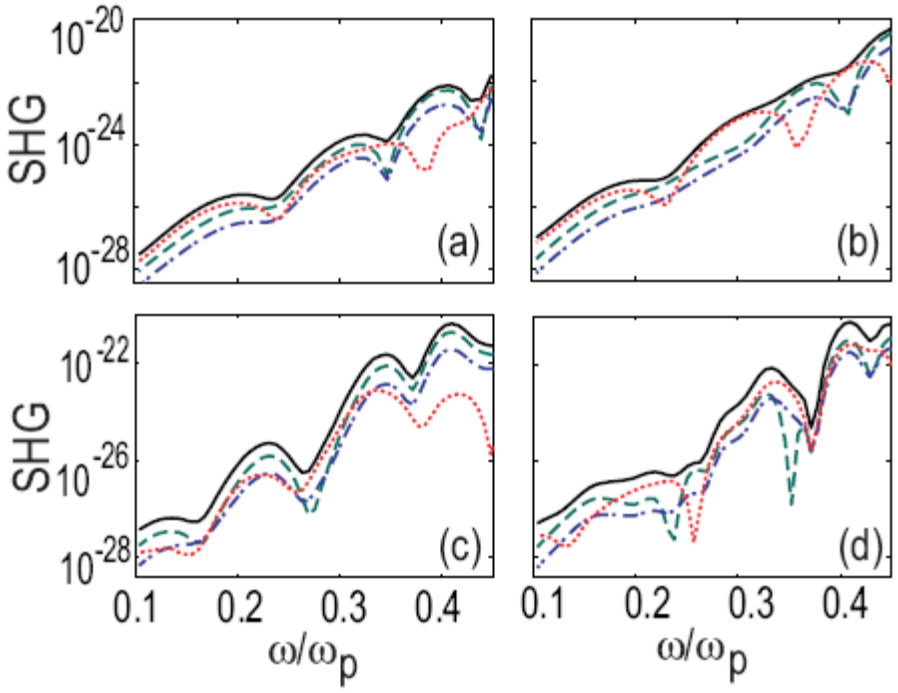

FIG. 4.11: Top and bottom panels show the SHG corresponding to cylindrical and hemispherical surface defects, respectively. In all panels, the spectra correspond to the electric dipole moment (dotted curves), the magnetic dipole moment (dash curves), the electric quadrupole moment (dotted-dash curves), and the total amount of generated SH (solid curves).

Our calculations show that, unlike the case of the FF, the spectra of the radiated light at the SH depend to a lesser extent on the shape of the surface defect. This conclusion is illustrated by Fig. 4.11, which shows the spectra corresponding to cylindrical and hemispherical defects, for both $h > 0$ and $h < 0$. The general characteristics of these spectra are very similar to those corresponding to the Gaussian surface defects, part of the observed differences being attributable to the fact that the defects have different size. Indeed, the amount of radiation emitted at the SH depends primarily on the magnitude of the induced multipole moments and thus one expects that the general characteristics of the corresponding spectra would depend only slightly on the shape of the surface defect.

One of the important applications of the theoretical formalism presented here is that the spectral characteristics of the radiation emitted at the SH can be used to extract information about the geometry of the surface defects and their surface properties. For example, since the angular distribution of the radiation emitted by electric dipoles, electric quadrupoles, and magnetic dipoles are quite different from each other, the angular distribution of the total radiated light at the SH will depend strongly on the relative strength of the magnitude of these induced multipoles. Therefore, the angular distribution of the total light emitted at the SH can provide valuable information about the shape and surface properties of the defect. This idea is illustrated in Fig. 4.12, where we show the angular distribution of the light emitted at the SH, as well as the angular distribution corresponding to the electric dipole, electric quadrupole, and magnetic dipole. Note that in this figure the parameters of the surface defect and the wavelength of the incident SPP wave have been chosen such that the amount of light radiated by each of the three multipoles has a comparable magnitude, and therefore the angular distribution of the total radiated light is

different from each of the angular distributions corresponding to the three multipoles. However, in the case in which one of the multipoles dominates, the total angular distribution of the SH will be similar to the angular distribution of that multipole and thus this information can be used to determine the properties of the surface defect.

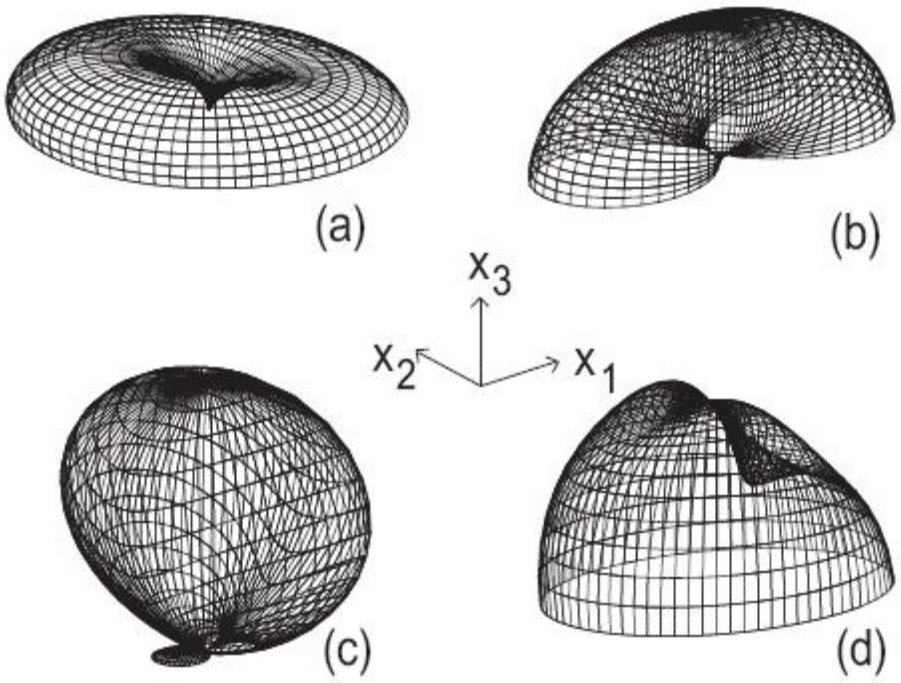

FIG. 4.12: Angular distribution of the power emitted at the SH. The panels correspond to a Gaussian surface defect with R = 200 nm and h = −50 nm, and an incident SPP wave with wavelength λ = 1012 nm. The panels correspond to, (a), the electric dipole momentum; (b), the magnetic dipole momentum; (c), the electric quadrupole moment; and (d), the total SH.

The angular distribution of the power emitted at the SH can be used not only to infer which is the dominant multipole that generates light at the SH, but also to obtain information about the shape of the surface defect. As illustrated in Fig. 4.13, this is possible because the angular distribution of the power radiated at the SH is strongly dependent on the shape of the surface defect. Thus, as Fig. 4.13 shows, the angular distribution of the power emitted by a cylindrical defect is very different from the angular dependence of the power emitted by a hemispherical defect. Consequently, measuring the angular distribution of the power generated at the SH could represent a powerful surface probing tool.

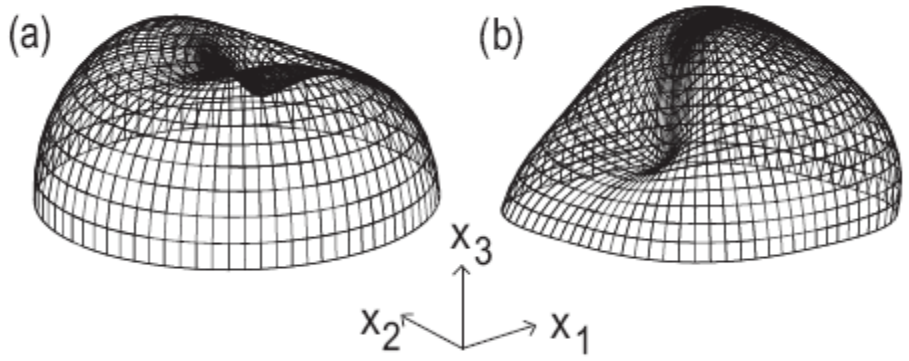

FIG. 4.13: Angular distribution of the power emitted at the SH. The panels correspond to a cylindrical (left) and hemispherical (right) surface defect, the wavelength of the incident SPP being λ = 1012 nm. The defect parameters are: (a), R = 200 nm and h = −20 nm; (b), R = 600 nm and h = −50 nm.

In addition to the angular dependence of the power emitted at the SH, the spatial distribution of the near-field at the SH can provide valuable information about the properties of the surface defect. In particular, the spatial distribution of the near-field at the SH depends on the shape of the surface defect and the nature of the surface (through the surface susceptibility) and thus near-field surface optical microscopy measurements at the SH can be used as an effective tool to study the properties of surface defects. [13]. As an example, we show in Fig. 4.14 the spatial distribution of the near-field at the SH, corresponding to a Gaussian defect. Our calculations show clearly that such field distributions are strongly dependent on the shape of the surface defect and the wavelength of the incident SPP wave, a property explained by the fact that the relative strength of the induced multipoles that determine this field distribution is strongly dependent on these parameters. Arguments similar to those just presented in connection to the angular distribution of the power radiated at the SH allow us to conclude that the near-field at the SH can be used to retrieve additional information, which is not contained in the field distribution at the FF.

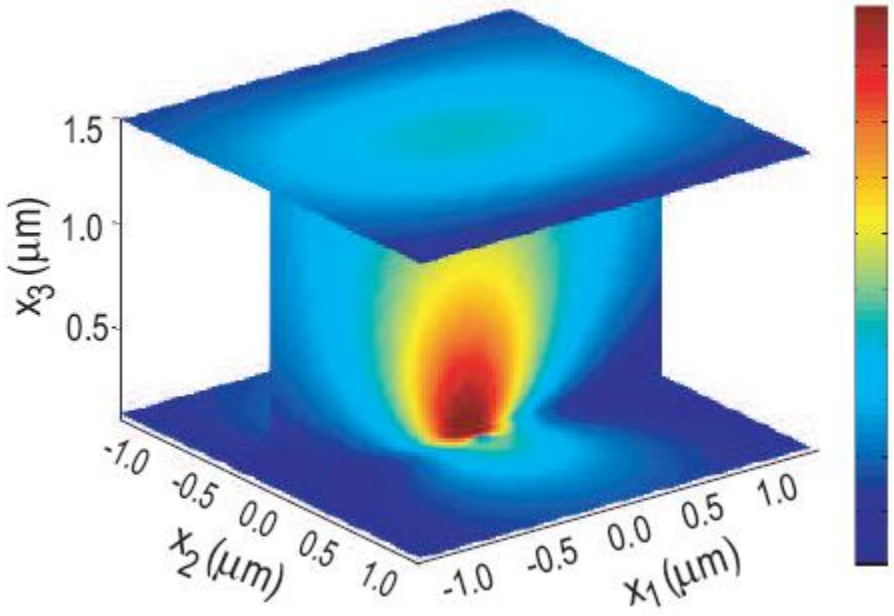

FIG. 4.14: Electric field distribution corresponding to the scattering of a SPP off a Gaussian surface defect with R = 200 nm and h = −50 nm. The wavelength of the incident SPP is λ = 328 nm.

4.4. CONCLUSIONS

In conclusion, we have presented a comprehensive analysis of the physical characteristics of the SH generated as a result of the scattering of SPP waves off surface metallic nanodefects with radial symmetry. Our analysis, based on a set of coupled reduced Rayleigh equations, can be applied to surface nanodefects of arbitrary shape; in particular, we have investigated surface nanodefects with three different geometries that are important in practical applications, namely, Gaussian, hemispherical, and cylindrical nanodefects. Moreover, our study shows that the physical characteristics of the scattering process at the

FF, namely the distribution of the electromagnetic field and the spatial pattern of the emitted radiation, is markedly different from those of the scattering process at the SH, and therefore the surface generated SH could prove to be an invaluable non-invasive diagnosis tool in surface spectroscopy. In particular, we have demonstrated that the structure of the generated electromagnetic field at the SH is strongly dependent on the shape of the surface nanodefects and on the physical properties of the surface, through the surface profile function $\zeta(x_{\parallel})$ and the surface susceptibility $\chi_s^{(2)}$, respectively. As a result, our study proves that the formalism introduced here has applicability to surface imaging or to surface physical chemistry, e.g, to measurements of physical quantities related to molecular adsorbates at interfaces or on metallic surfaces.

It is important to note, also, that our formalism can be easily extended to the case of more than one surface nanodefect or to a periodic distribution of such surface nanodefects. Thus, by extending our theoretical work to these more complex nanostructures would allow one not only to reach a deeper understanding of linear and nonlinear light interaction with nanopatterned metallic structure, but also provide us with a powerful tool to design and investigate new plasmonic nanodevices, such as light concentrators in deep-sub-wavelength spatial domains or optical nanoantennae.

4.5 APPENDIX:

4.5.1 DIFFERENTIAL AND TOTAL SCATTERING CROSS SECTIONS AT THE FUNDAMENTAL FREQUENCY

The field distribution described by the Eq. (4.1) contains two components that are of particular interest for an experimental investigation of scattering of SPPs by metallic

nanostructures, namely the far field component radiated as an outward propagating spherical wave, in the region $x_3 \geq \zeta(x_\parallel)$, and a cylindrical SPP wave, which represents the far field component of the scattered SPP. The far field distribution of the scattered light can be derived from Eq. (4.1), by using the stationary phase approximation, [45], and is given by the expression

$$E_{rad}^{\uparrow}(x;\omega) = -\frac{i\omega}{2\pi c}\cos(\theta_x)\frac{e^{\frac{i\omega}{c}x}}{x}[\hat{e}_p A_p\left(\frac{\hat{x}_\parallel \omega}{c}\sin(\theta_x)\right) + \hat{e}_s A_s\left(\frac{\hat{x}_\parallel \omega}{c}\sin(\theta_x)\right)] \quad 4.20$$

whereas the far field scattered SPP can be written as [43]:

$$E_{rad}^{\uparrow}(x;\omega) = -\frac{c\alpha(\omega)}{\omega}\frac{e^{ik_\parallel(\omega)x_\parallel - \alpha_0(\omega)x_3 + \frac{i\pi}{4}}}{\sqrt{2\pi k_\parallel(\omega)x_\parallel}} \frac{\left(i\hat{x}_\parallel \alpha_0(\omega) - \hat{x}_3 k_\parallel(\omega)\right)}{\epsilon(\omega)+1} a_p(x_\parallel k_\parallel(\omega)) \quad 4.21$$

The unit vectors $\hat{e}_s = (-\sin(\phi_x), \cos(\phi_x), 0)$ and $\hat{e}_p = (\cos\theta_x \cos\phi_x, \cos\theta_x \sin\phi_x, -\sin\theta_x)$ in define the polarization direction of s- and p-polarized waves, respectively, whereas $\vec{x} = x(\sin\theta_x \cos\phi_x, \sin\theta_x \sin\phi_x, \cos\theta_x)$ is a vector that defines the direction of observation. Note that the expression (A.2) is equal to 2π times the residue of the integrand in Eq. (1) at the pole $q_\parallel = k_\parallel(\omega)$. The Eqs. (A.1) and (A.2) can be used to calculate the amount of energy scattered into radiative modes (light) and surface plasmon waves. Thus, the power density radiated in the solid angle defined by the angles θ_x and ϕ_x is $\frac{dP_{rad}(\theta_x,\phi_x)}{d\Omega} = x^2 Re\{S_{r,rad}(\mathbf{x};\omega)\}$, whereas the power density

emitted by the surface plasmon wave, in a direction defined by the angle ϕ_x, is $\frac{dP_{SPP}(,\phi_x)}{d\phi_x} = x_{\|} Re\{S_{r,SPP}(\mathbf{x};\omega)\}$. Here, $S_{r,SPP}(\mathbf{x};\omega)$ is the radial component of the Poynting vector. Moreover, the power density associated to the incident surface plasmon wave, per unit length, can be written as $\frac{dP_{inc}}{dx_2} = Re\left\{S_{1,inc}(\mathbf{x};\omega)\right\}$, where the component $S_{1,inc}(\mathbf{x};\omega)$ corresponds to the first term in the r.h.s. of Eq. (4.1). Furthermore, these power densities can be used to define two deferential scattering cross-sections, $\sigma_{rad}(\theta_x,\phi_x)$ and $\sigma_{SPP}(\phi_x)$, which characterize the scattering of the incident surface plasmon wave into radiation and outgoing surface plasmons, respectively:

$$\Sigma_{rad}(\theta_x,\phi_x) \equiv \frac{d\sigma_{rad}}{d\Omega} = \frac{1}{P_{inc}}\frac{dP_{rad}(\theta_x,\phi_x)}{d\Omega} \tag{4.22a}$$

$$\Sigma_{SPP}(\phi_x) \equiv \frac{d\sigma_{SPP}}{d\phi_x} = \frac{1}{P_{inc}}\frac{dP_{SPP}(\phi_x)}{d\phi_x} \tag{4.22b}$$

Finally, from the differential scattering cross-sections we can determine the total scattering cross-sections, quantities that are given by the following expressions:

$$\sigma_{rad} = \frac{1}{P_{inc}}\int_0^{\frac{\pi}{2}} d\theta_x \sin\theta_x \int_{-\pi}^{\pi} d\phi_x x^2 Re\{S_{r,rad}(\mathbf{x};\omega)\} \tag{4.23a}$$

$$\sigma_{SPP} = \frac{1}{P_{inc}}\int_0^{\infty} dx_3 \int_{-\pi}^{\pi} d\phi_x x_{\|} Re\{S_{r,SPP}(\mathbf{x};\omega)\} \tag{4.23b}$$

Here, the incident power P_{inc} can be written as

$$P_{inc} = \int_{-\frac{L}{2}}^{\frac{L}{2}} dx_2 \int_0^{\infty} dx_3 Re\{S_{1,inc}(\mathbf{x},\omega)\} \tag{4.24}$$

4.5.2 BORN APPROXIMATION

A big challenge for simulations is to verify the correctness of numerical codes. In order to do this, we use Born Approximation for the lower frequency range to get a better understanding of our results as well as to verify our code.

Born Approximation is an analytical approach for analyzing scattering properties in which the higher orders of interactions are neglected.

Bibliography:

[1] W. L. Barnes, A. Dereux, and T. W. Ebbesen, Nature (London) 424, 824 (2003).

[2] T. W. Ebbesen, H. J.Lezec, H. F. Ghaemi, T. Thio, P. A. Wolff, Nature (London) 391,667(1998).

[3] S. I. Bozhevolnyi, J. Erland, K. Leosson, P. M. W. Skovgaard, and J. M. Hvam, Phys. Rev Lett. 86, 3008 (2001).

[4] S. K. Gray and T. Kupka, Phys. Rev. B 68, 045415 (2003).

[5] W. Nomura, M. Ohtsu, and T. Yatsui, Appl. Phys. Lett. 86, 181108 (2005).

[6] S. I. Bozhevolnyi, V. S. Volkov, E. Devaux, J. Y. Laluet, and T. W. Ebbesen, Nature (London) 440, 508 (2006).

[7] X. P. Zhang, B. Q. Sun, R. H. Friend, H. C. Guo, D. Nau, and H. Giessen, Nano Lett. 6, 651 (2006).

[8] J. Cesario, M. U. Gonzalez, S. Cheylan, W. L. Barnes, S. Enoch, and R. Quidant, Opt. Express 15, 10533 (2007).

[9] R. M. Roth, N. C. Panoiu, M. M. Adams, J. I. Dadap, and R. M. Osgood, Opt. Lett. 32, 3414 (2007).

[10] S. M. Nie and S. R. Emery, Science 275, 1102 (1997).

[11] K. Kneipp, Y. Wang, H. Kneipp, L. T. Perelman, I. Itzkan, R. R. Dasari, and M. S. Feld, Phys. Rev. Lett. 78, 1667 (1997).

[12] C. L. Haynes and R. P. Van Duyne, J. Phys. Chem. B 107, 7426 (2003).

[13] R. M. Roth, N. C. Panoiu, M. M. Adams, R. M. Osgood, C. C. Neacsu, and M. B. Raschke, Opt. Express 14, 2921 (2006).

[14] D. M. Schaadt, B. Feng, and E. T. Yu, Appl. Phys. Lett. 86, 063106 (2005).

[15] J. Cole and N. J. Halas, Appl. Phys. Lett. 89, 153120 (2006).

[16] N. C. Panoiu and R. M. Osgood, Opt. Lett. 32, 2827 (2007).

[17] R. D. R. Bhat, N. C. Panoiu, S. R. J. Brueck, and R. M. Osgood, Opt. Express 16, 4588 (2008).

[18] R. M. Osgood and D. J. Ehrlich, Opt. Lett. 7, 385 (1982).

[19] C. J. Chen and R. M. Osgood, Phys. Rev. Lett. 50, 1705 (1983).

[20] H. J. Simon, D. E. Mitchell, and J. G. Watson, Phys. Rev. Lett. 33, 1531 (1974).

[21] A. V. Baranov, Y. S. Bobovich, and V. I. Petrov, Opt Spektrosk+ 58, 578 (1985).

[22] C. K. Johnson and S. A. Soper, J. Phys. Chem. 93, 7281 (1989).

[23] R. Antoine, P. F. Brevet, H. H. Girault, D. Bethell, and D. J. Schiffrin, Chem. Commun., 1901 (1997).

[24] E. C. Hao, G. C. Schatz, R. C. Johnson, and J. T. Hupp, J. Chem. Phys. 117, 5963 (2002).

[25] A. Bouhelier, M. Beversluis, A. Hartschuh, and L. Novotny, Phys. Rev. Lett. 90, 013903 (2003).

[26] W. Fan, S. Zhang, N. C. Panoiu, A. Abdenour, S. Krishna, R. M. Osgood, K. J. Malloy, and S. R. J. Brueck, Nano Lett. 6, 1027 (2006).

[27] L. Cao, N. C. Panoiu, and R. M. Osgood, Phys. Rev. B 75, 205401 (2007).

[28] C. Hubert, L. Billot, P. M. Adam, R. Bachelot, P. Royer, J. Grand, D. Gindre, K. D. Dorkenoo, and A. Fort, Appl. Phys. Lett. 90, 181105 (2007).

[29] N. C. Panoiu and R. M. Osgood, Nano Lett. 4, 2427 (2004).

[30] H. Raether, Surface Polaritons on Smooth and Rough Surfaces and on Gratings (Springer-Verlag, Berlin, 1995).

[31] A. V. Zayats, I. I. Smolyaninov, and A. A. Maradudin, Phys. Rep. 408, 131 (2005).

[32] T. F. Heinz, In Nonlinear Surface Electromagnetic Phenomena H. E. Panath, and G. I. Stegeman, (Elsevier, Amsterdam, 1991); p 353.

[33] S. I. Bozhevolnyi and K. Pedersen, Surf. Sci. 377-379, 384 (1997).

[34] U. Kreibig and M. Vollmer, Optical Properties of Metal Clusters (Springer-Verlag, Berlin, 1995).

[35] J. I. Dadap, J. Shan, and T. F. Heinz, J. Opt. Soc. Am. B 21, 1328 (2004).

[36] K. B. Eisenthal, Chem. Rev. 106, 1462 (2006).

[37] K. Atsushi, Y. S. Jung, H. K. Kim, and H. Petek, J. Phys. B: At. Mol. Opt. Phys. 40, S259-S272 (2007)

[38] G. Boisde and A. Harmer, Chemical and Biochemical Sensing with Optical Fibers and Waveguides (Arthech House, Boston, 1996).

[39] J. L. West and N. J. Halas, Annu. Rev. Biomed. Eng. 5, 285 (2003).

[40] M. A. Ordal, L. L. Long, R. J. Bell, S. E. Bell, R. R. Bell, R. W. Alexander, and C. A. Ward, Appl. Opt. 22, 1099 (1983); M. A. Ordal, R. J. Bell, R. W. Alexander, L. L. Long, and M. R. Querry, ibid. 24, 4493 (1985).

[41] G. C. Brown, V. Celli, M. Haller, and A. Marvin, Surf. Sci. 136, 381 (1984).\

[42] A. A. Maradudin, In Topics in Condensed Matter Physics; Das, M. P., Ed. (Nova Science: New York, 1994); p 33.

[43] A. V. Shchegrov, I. V. Novikov, and A. A. Maradudin, Phys. Rev. Lett. 78, 4269 (1997).

[44] J. A. Sanchez-Gil and A. A. Maradudin, Phys. Rev. B 60, 8359 (1999).

[45] D. L. Mills, Phys. Rev. B 12 4036 (1975).

[46] N. Bloembergen, R. K. Chang, S. S. Jha, and C. H. Lee, Phys. Rev. 174, 813 (1968).

[47] J. E. Sipe, V. C. Y. So, M. Fukui, and G. I. Stegeman, Phys. Rev. B 21, 4389 (1980).

[48] J. E. Sipe, V. Mizrahi, and G. I. Stegeman, Phys. Rev. B 35, 9091 (1987).

[49] G. S. Agarwal and S. S. Jha, Solid State Commun. 41, 499 (1982).

[50] D. Krause, C. W. Teplin, and C. T. Rogers, J. Appl. Phys. 96, 3626 (2004).

[51] J. D. Jackson, Classical Electrodynamics, 3rd ed. (Wiley & sons, Inc., Hoboken, 1999).

[52] J. I. Dadap, J. Shan, K. B. Eisenthal, and T. F. Heinz, Phys. Rev. Lett. 83, 4045 (1999).

[53] W. H. Press, S. A. Teukoisky, W. T. Vetterling, and B. P. Flannery, Numerical Recipes in C (Cambridge University Press, Cambridge, U. K., 1992).

[54] V. Kuzmiak and A. A. Maradudin, Phys. Rev. B 55, 7427 (1997).

[55] T. Ito and K. Sakoda, Phys. Rev. B 64, 045117 (2001).

Chapter 5

Future Studies

There are several clear central directions for interesting future work after this thesis. As we have discussed, this thesis yielded an analytical approach for understanding the scattering properties of SPP by metallic nanostructures. We were still able to do the simulations for 1D Gaussian structures as well as 2D circularly symmetric nanostructures. Finally, this approach is a general approach and is easy applicable to different systems. These more complex systems are as follows:

1. Scattering of SPP by grating metallic structures

A grating structure is a simple extension of the 1D Gaussian structure we have discussed in Chapter 3. The approach to solve this problem should start from Eq. (3.3) and change the function $f(q)$. All the other equations should hold. In this way, we can simulated the interaction of SPP's with gratings, which are typical coupling devices for optical SPP excitation.

2. Scattering of SPP by multiple circularly symmetric nanodefects

An important goal of this project is to simulate random distributions of defects, adsorbates, or adsorbates on planar surfaces. A first-order approximation for such multiple nanodefects can come from the simple superposition of the electric field of

single defects. However, for more accuracy, a better approach should start from Eq. (4.8) and use the exact form for the surface function. The chief difficulty in these calculations is the loss of a simple single spatial origin for the nanostudies.

3. Design of optical devices

Once we could solve the multiply defects problem, an application should be the prediction of surface scattering phenomena thus to design new optical devices for the control of optical-like surface energy flow.

4. Scattering of SPP by chiral metallic nanostructures.

If the surface defect has chirality, it is expected that we could generate nanoflashlights with angular momentum. This is a very interesting direction, which can be used for chiral molecule probing.

Appendix A:

PUBLICATIONS

A.1 Publications in refereed journals

1. **L. Cao**, N. C. Panoiu, R. M. Osgood Jr., "Surface second-harmonic generation from surface plasmon waves scattered by metallic nanostructures", Phys. Rev. B.75.205401 (2007)

2. **L. Cao**, N. C. Panoiu, R. Bhat, R. M. Osgood Jr., "Surface Second-Harmonic Generation from Scattering of Surface Plasmon Polaritons from Radially Symmetric Nanostructures" (under review for Phy. Rev.B)

A.2 Conference presentations:

1. **L. Cao**, N. C. Panoiu, S. Zhang, W. Fan, K. J. Malloy, S. R. J. Brueck and R. M. Osgood, "Second Harmonic Generation by Scattering of Surface Plasmon Polaritons by Metallic Nanodefects", Materials Research Society Fall 2005 meeting, GG3.5.
2. **L. Cao**, N. C. Panoiu, R. M. Osgood, "Second Harmonic Generation of Surface Plasmon Polaritons Scattered by Metallic Nanostructures", Integrated Photonics Research and Applications (IPRA) 2006 paper: IMC2

3. X. Chen, **L. Cao**, N.C. Panoiu, R.M. Osgood, R. Scarmozzino, "Numerical Studies of Dispersion Properties of SOI Photonic Nanowires",. 3rd IEEE International Conference on Group IV Photonics, 2006, page 155-157, 9274207

4. **L. Cao**, N. C. Panoiu, R. M. Osgood , "Surface Second-Harmonic Generation from Scattering of Surface Plasmon Polaritons from Circularly Symmetric Metallic Nanostructures", Frontiers in Optics (FiO) 2008 paper: FThC2